FRACTURE CHARACTERIZATION AND PREDICTION IN THE "MISSISSIPPIAN LIMESTONE" IN NORTH-CENTRAL OKLAHOMA

By

TAYLOR THOMPSON

Bachelor of Arts in Geology

University of Colorado

Boulder, CO

2013

Submitted to the Faculty of the
Graduate College of the
Oklahoma State University
in partial fulfillment of
the requirements for
the Degree of
MASTER OF SCIENCE
May, 2016

FRACTURE CHARACTERIZATION AND PREDICTION IN THE

"MISSISSIPPIAN LIMESTONE" IN NORTH-CENTRAL

OKLAHOMA

Thesis Approved:

Dr. G. Michael Grammer

Thesis Advisor

Dr. James Puckette

Dr. Daniel Laó Dávila

ACKNOWLEDGEMENTS

First, I would like to thank Dr. Michael Grammer for his assistance throughout my research. His invaluable guidance and insight during my time at Oklahoma State University greatly assisted my academic, professional, and personal growth. I would also like to thank my committee members, Dr. Jim Puckette and Dr. Daniel Laó Dávila, for their insight and assistance regarding my research.

I would like to thank my "carbonate clan" colleagues Stephanie LeBlanc, Beth Vanden Berg, Buddy Price, Miranda Childress, Yulun Wang, Ashley Dupont, Scott Shelley, Lara Jaeckel, C. J. Appleseth, Ibukun Bode, Ahmed Elbelasy, and Elizabeth Elium. Their assistance with my research was greatly appreciated and I am thankful I had the opportunity to work with such intelligent and enjoyable people. I would also like to thank Garrett Hickman, Skyler St. John, and Sahar Mohammadi for their assistance with my research.

Lastly, I would like to say a big thank you to my family for their constant support and encouragement throughout my time spent at Oklahoma State University.

Name: TAYLOR THOMPSON

Date of Degree: MAY, 2016

Title of Study: FRACTURE CHARACTERIZATION AND PREDICTION IN THE "MISSISSIPPIAN LIMESTONE" IN NORTH-CENTRAL OKLAHOMA

Major Field: GEOLOGY

Abstract:

Unconventional Mississippian oil and gas reservoirs in central and northern Oklahoma and southern Kansas are characterized by porosities of 1-2 percent or less, and permeability values measured in fractions of millidarcies. As such, natural fractures are an important part of reservoir performance in the "Mississippi Lime." Understanding the types and distribution of fractures in these carbonate rocks and how they may be related to facies and sequence stratigraphic architecture, may increase the predictability of fracture-enhanced permeability in the subsurface. The overall goal of the study is to understand the distribution and types of fractures within the "Mississippian Limestone" as they may relate to specific facies and sequence stratigraphic architecture to increase the subsurface predictability of fracture permeability.

Three cores from Payne and Osage counties, Oklahoma were utilized in this study (Elinore #1-18, Winney #1-8, and Orion Blackbird #3-44). Fracture types in the cores were first identified and various fracture properties were measured. This data was integrated with the established high-resolution sequence stratigraphic framework to analyze the distribution of fractures within petrophysically-significant facies.

Fracture types and fracture density are facies dependent (i.e. fracture predictability is enhanced by tying the data to the 4 defined facies types). The crinoidal packstone-grainstone facies had the highest number of ptygmatic and vertical extensional fractures and the highest fracture density in the Elinore and Winney cores (1.95 fractures per foot and 1.46 fractures per foot). The glauconitic sandstone facies had the lowest fracture density (0 fractures total). In the Orion core, the bioturbated wackestone-packstone facies had the highest number of ptygmatic and vertical extensional fractures as well as the highest fracture density (2.56 fractures per foot).

Fracture types and densities were compared to the sequence stratigraphic framework and XRD data. Fracture type and fracture density correlate to the regressive phases of probable 3rd order high frequency sequences in the Elinore and Winney, suggesting that fracture trends can be predicted by tying the data to the sequence framework. Fracture density did not correlate to the XRD data at high resolutions, but did correlate when the data was averaged by facies type. A more comprehensive dataset would likely yield a more reliable correlation.

Micro-CT scanning of fractured samples proved to be a useful tool in evaluating the fracture distribution beyond what can be seen at the surface of the core and highlights the need for analyzing microfractures.

TABLE OF CONTENTS

Chapter Page

LIST OF TABLES

Table Page

LIST OF FIGURES

Figure Page

Figure Page

CHAPTER I

INTRODUCTION

The "Mississippian Limestone" of the Mid-Continent contains hydrocarbon-rich reservoirs in Oklahoma and Kansas (Figure 1). The "Mississippian Limestone" play has historically been developed using vertical drilling techniques and was considered to be exhausted of its hydrocarbon resources (Montgomery et al., 1998). However, in recent years, horizontal drilling has allowed for new development of unconventional reservoirs like those of Mississippian carbonates. The Mississippian carbonate system of the Mid-Continent is highly heterogeneous, including a mix of siliciclastic and carbonate rocks. The unpredictable and laterally discontinuous reservoir units in the system include: spiculite, tripolite, dolomite, chat, grainstone, and mound facies. Recent work on the Mississippian carbonates of the Mid-Continent has resulted in the development of a sequence stratigraphic hierarchy in the region that has begun to solve the unpredictability of various reservoir units (e.g. LeBlanc, 2014; Price, 2014; Childress, 2015; Childress and Grammer, 2015). This work includes both outcrop and subsurface

studies in which a high-resolution sequence stratigraphic framework was constructed to better understand the vertical and lateral continuity of facies distribution.

Unconventional “Mississippian Limestone” reservoirs of the Mid-Continent are characterized by low porosities, generally 1-2 percent or less, and low permeability values typically in the fractions of millidarcies (Grieser and Pinkerton, 2013). Because of these low porosity and permeability values, natural fractures could be an important part of reservoir performance. A comprehensive fracture study that ties to the recently determined high-resolution sequence stratigraphic framework in the “Mississippian Limestone” of the Mid-Continent allows for further examination of the controls on the natural fracturing in the system.

The primary goals of this research are to: 1) identify the types of fractures in the “Mississippian Limestone” using three cores located in Payne and Osage counties, Oklahoma; 2) determine if the fractures can be correlated to petrophysically-significant facies types; and 3) determine if the subsurface predictability of fractures can be enhanced by tying to either facies, lithology, or the sequence stratigraphic framework. By attempting to tie fracture type and fracture density to petrophysically-significant facies types and the overall sequence stratigraphic architecture, the controls of the natural fracture system in the “Mississippian Limestone” can be analyzed from a higher resolution standpoint. This will allow for increased subsurface predictability of fracture networks in these unconventional carbonate reservoirs.

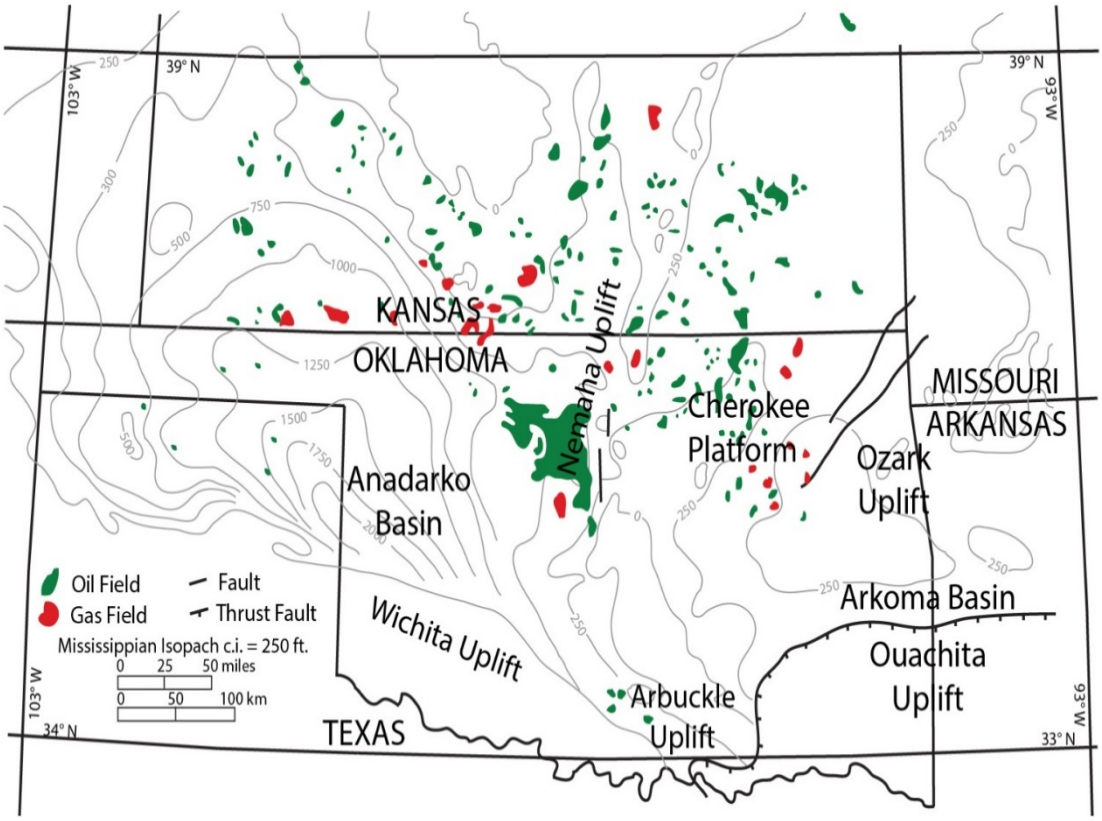

Figure 1. Map of the "Mississippian Limestone" oil (green) and gas (red) fields defined primarily with vertical drilling. The largest oil field is located in north - central Oklahoma (Sooner Trend). Thickness of the Mississippian system is mapped in gray, with the thickest Mississippian section in western Oklahoma. Modified from Harris (1975).

Geologic Setting

Mississippian carbonates were deposited across the ancient Burlington Shelf, which extended across parts of Nebraska, Colorado, Kansas, Oklahoma, Arkansas, Missouri, Iowa, and Illinois (Figure 2) (Lane and DeKyser, 1980; Gutschick and Sandberg, 1983). During the Mississippian, the depositional system was located approximately 20-30 degrees south of the paleoequator in relatively shallow marine conditions and subtropical climates (Gutschick and Sandberg, 1983; Witzke et al., 1990, Blakey, 2011).

Recent interpretations conclude that deposition took place in a carbonate ramp to distally steepened ramp environment (Wilhite et al., 2011; LeBlanc, 2014; Price, 2014; Childress, 2015; Childress and Grammer, 2015). Figure 3 illustrates the location of the three subsurface cores used for this study, which include the Winney #1-8, Elinore #1-18, and the Orion Blackbird #3-44 located in north-central Oklahoma in Payne and Osage counties.

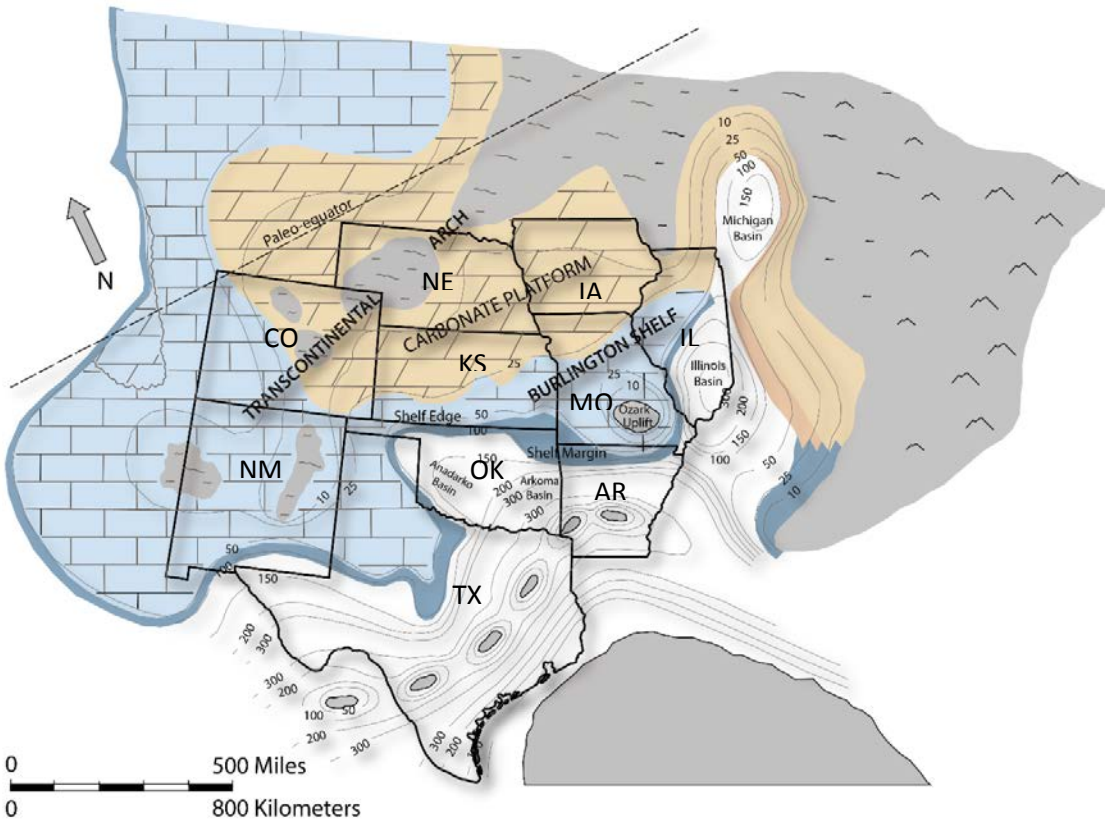

Figure 2. Paleo-depositional model representative of the Early Mississippian time. The model depicts the west-east trending Mississippian carbonate system of the Mid-Continent as being deposited across the ancient Burlington Shelf, with shallower water regions present in the north and deeper water to the south. It is important to note that this model is a generalized static model that only represents a single and simplified time slice of a dynamic system. Modified from Gutschick and Sandberg (1983).

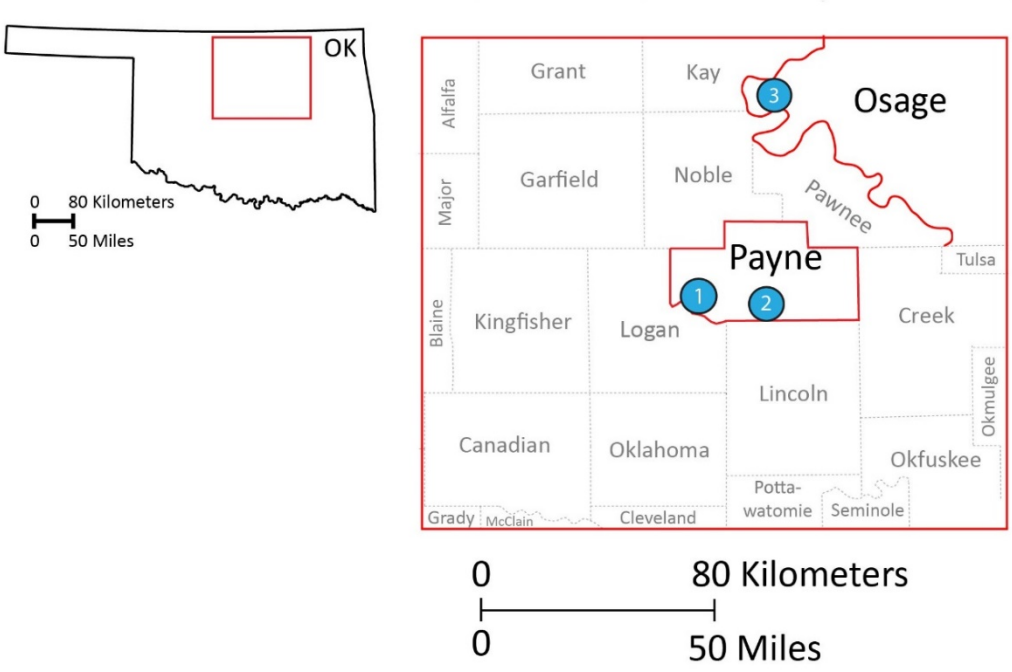

Figure 3. Map of the study area in Oklahoma. Core locations are shown in blue. The Winney #1-8 core (1 on figure) and the Elinore #1-18 core (2 on figure) are located in Payne County. The Orion Blackbird #3-44 core (3 on figure) is located in Osage County.

Major tectonism in the Mid-Continent began in the Late Mississippian (~330 Ma) and climaxed in the Early Pennsylvanian (~318 Ma) with the Ouachita Orogeny and uplift and faulting of the Nemaha Ridge (Gay, 2003; Gay, 1999). The Nemaha Uplift (also referred to as the Nemaha ridge) is a north-south trending structural feature in north-central Oklahoma and southern Kansas consisting of a belt of high angle to reverse faulting (Gay, 2003). The study areas are located east of the Nemaha uplift on the Cherokee Platform. Structural features bordering the study areas include the Ozark Uplift to the east, the Arbuckle Uplift to the south, and the Anadarko Basin to the southwest (Figure 4).

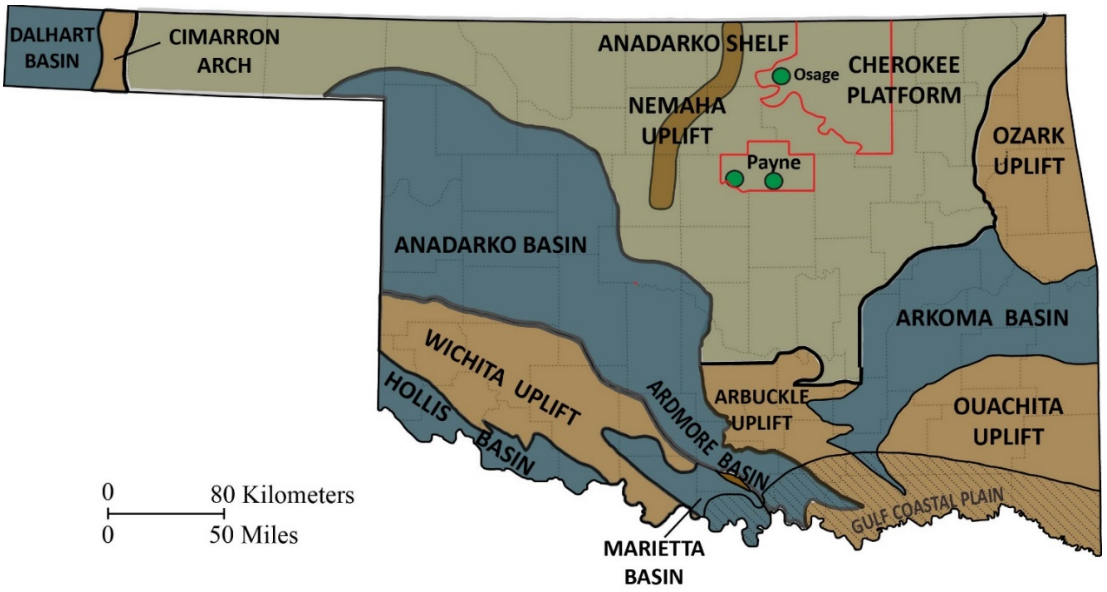

Figure 4. Map depicting the size and orientation of structural features in Oklahoma relative to the study areas (core locations are shown in green, counties are outlined in red). Brown regions represent uplifted regions relative to depression features (blue). The cores are located on the Cherokee Platform, east of the Nemaha Uplift. Structural features bordering the study areas include the Anadarko Basin to the southwest, the Arbuckle Uplift to the south, the Arkoma Basin to the southeast, and the Ozark Uplift to the east. Modified from Northcutt and Campbell (1996).

Stratigraphy

Mississippian-aged strata in the Mid-Continent is informally referred to as the "Mississippian Limestone", however, these Mississippian aged rocks are composed of a mixture of carbonates and siliciclastics (Montgomery et al., 1998). In the Mid Continent, the Mississippian stratigraphic section typically overlies the Devonian Woodford shale and occurs beneath the unconformable contact of the overlying Pennsylvanian strata. The cores used for this study do not have exact stratigraphic ranges assigned to them due to lack of biostratigraphy, but the unconformities at each contact between the overlying (Pennsylvanian) and underlying (Devonian) deposits have been observed in all three cores indicating they are of Mississippian age.

Sea Level and Cyclicity

Shallow water marine carbonate systems are highly dependent on sea level fluctuations. Eustatic sea level history during the Mississippian is related to a transitional period from greenhouse conditions that existed in the Devonian, to icehouse conditions that existed during the Pennsylvanian (Read, 1995). Depositional cycles are controlled by climate, sedimentation rates, tectonics, and Milankovitch cycles (Read, 1995). Milankovitch cycles refer to high frequency sequences and cycles (4^{th} and 5^{th} order). These are climatically driven sea level cycles that control the facies stacking patterns (lithologies) in carbonate systems (Read, 1995). The Milankovitch cycles are controlled by changes in earth's eccentricity (shape of orbit), which is associated with 4^{th} order sequences (100-400 kyr duration), and changes in obliquity (earth's axial tilt, ~40 kyr) and precession (wobble of earth's axial orientation, ~20 kyr), which are associated with 5^{th} order cycles (Read, 1995).

CHAPTER II

METHODS AND DATA

Measured and Calculated Fracture Parameters

Data collection included fracture aperture and height measurements for each fracture visible in core as well as tabulation of fracture density. These parameters were chosen based on methods used for fracture studies by Lockman et al. (1997), Cooper and Lorenz (2012), and Nelson (2001).

Measuring Fracture Apertures

In order to assess porosity and permeability of a natural fracture system, data that defines the aperture of fractures is needed. The fracture aperture refers to the width of the fracture opening. Measurements of fracture apertures in this study include both widths of fully mineralized fractures as well as open sections of fractures to evaluate the total amount of fracturing (i.e. the original width of the fracture). The measurements were obtained by measuring the apertures directly on the core face with

a millimeter scale ruler. The apertures for most fractures varied, thus an average fracture aperture was calculated using the minimum aperture measurement and the maximum aperture measurement.

One limitation that exists in measuring fracture apertures optically is the ability to see fracture apertures smaller than a few tenths of a millimeter. There is likely some error associated with the aperture measurements of smaller fracture apertures. Another limitation associated with measuring fracture apertures is the difficulty in measuring the apertures in natural rubble zones or pieces of the core that are split apart due to primary and/or induced fracturing. Because the apertures cannot be measured in these circumstances, there is uncertainty with the aperture results found from rubble zones and pieces of core that are broken apart.

Measuring Fracture Heights

The fracture heights were obtained by measuring each fracture vertically with a millimeter scale ruler. It is important to note that fracture height in this study is not necessarily the same as fracture length. Capturing the true fracture length depends on both the orientation of the fracture parallel to the vertical direction of the core as well as the fracture type. There is a small population of horizontal fractures in the cores and these fracture heights were recorded as zero due to these fractures lacking a vertical dimension.

Calculating Fracture Density

Cooper and Lorenz (2012) and Nelson (2001) define fracture density as the number of fractures per foot of core. This is the definition of fracture density used in this study and differs from Lockman et al. (1997) who define it as the surface area of a fracture in a unit volume of rock. The available dataset, i.e. 3 subsurface cores, precludes accurately measuring the volume of rock through which a fracture may be found. The fracture density for each petrophysically-significant facies was calculated using the total footage of each facies divided by the total number of fractures identified in each facies.

X-Ray Diffraction

X-ray diffraction (XRD) provides quantitative estimation of rock mineralogy and was used in this study to analyze potential correlation of fractures to mineralogical variability. The XRD data was obtained from 1 inch diameter core plug samples taken from whole core that were analyzed by Weatherford Laboratories using bulk XRD methods. The Winney and Elinore XRD datasets were the same datasets used for XRD analysis in LeBlanc (2014), which included clay content, carbonate content, and various other minerals. The clay content was subdivided into percentages of chlorite, kaolinite, illite/mica, and illite/smectite. The carbonate content was separated into percentages of calcite, dolomite, and siderite. Percentages of quartz, potassium feldspar, plagioclase, pyrite, apatite, marcasite, halite, and barite were also reported. The XRD dataset for the Orion core included only percentages of quartz and calcite.

Potential limitations of the given XRD datasets for each core include: 1) the spacing of the core plug samples, which are not consistent in any of the datasets; 2) some of the sampling locations may have been purposefully chosen in unfractured zones, creating a sampling bias; 3) a first-order approximation of clay minerals was determined using bulk x-ray diffraction, however, oriented mounts to properly identify specific clay minerals were not used.

Micro-CT Scanning

Micro computed tomography (micro-CT) uses x-rays to image an object in three dimensions which is not possible from a 2-D core surface. Micro-CT scanning was used in this study for two 1.5 inch diameter core plug samples from the Winney core to visualize fractures and fracture distribution in three dimensions, which may lead to a better understanding of how the fractures are interconnected.

Previous Work and Petrophysically-Significant Facies

The Winney, Elinore, and Orion Blackbird cores were previously analyzed by LeBlanc (2014) and Vanden Berg (2016) for identification of facies types, vertical stacking patterns, pore types, and to constrain the high frequency sequence stratigraphic framework. Facies textures and pore types were examined using core and thin section analysis and were determined using the Dunham (1962) and Choquette and Pray (1970) classifications. Facies colors were determined using the GSA rock color designation chart (Goddard et al., 1951). According to LeBlanc (2014), five facies exist in the Winney and Elinore cores. Stratigraphically, from relatively deep to shallow water,

these facies include a glauconitic sandstone, burrowed calcareous mudstone-wackestone, bioturbated wackestone to packstone, peloidal packstone-grainstone, and a skeletal packstone-grainstone. Vanden Berg (2016) identified seven facies in the Orion Blackbird core, consisting of variations of mudstones, wackestones, and mud-lean packstones.

For this study, the facies identified by LeBlanc (2014) and Vanden Berg (2016) were grouped into four petrophysically-significant facies. Petrophysically-significant facies were defined based on probable susceptibility to brittle or ductile failure (i.e. how the rock would likely behave from a rock mechanics standpoint) and are defined here as discrete rock packages of similar mineralogy and texture. The following petrophysically-significant facies descriptions and interpretations are based on LeBlanc's (2014) previous facies descriptions and the reader is directed to that work for a more detailed analysis of facies interpretations.

Facies 1: Glauconitic Sandstone

The glauconitic sandstone facies (Figure 5) is composed primarily of sand-sized glauconite grains (average 45%) and silt-sized quartz (average 48%). Sparse phosphatic bone fragments (1-5%), and brachiopod fragments (5%) are also present. Mineralogically, the facies is characterized by an average of 23% total clay minerals (16% illite/mica, 7% illite/smectite), an average of 12% calcite, 0-10% dolomite by volume, and pyrite grains (average 4%). This facies is dark greenish gray in color and is characterized as having intraparticle and interparticle porosity (average porosity of

9.45%, minimum 9.34%, maximum 9.56%). The average permeability in Facies 1 is approximately 0.36 millidarcies (mD) (minimum 0.006 mD, maximum 0.71 mD). The glauconitic sandstone facies is present in the Winney and Elinore near the base of the cores, but is absent in the Orion Blackbird core. Facies 1 was interpreted to have been deposited in a restricted, low-energy environment, likely in a more distal portion along the carbonate ramp depositional model.

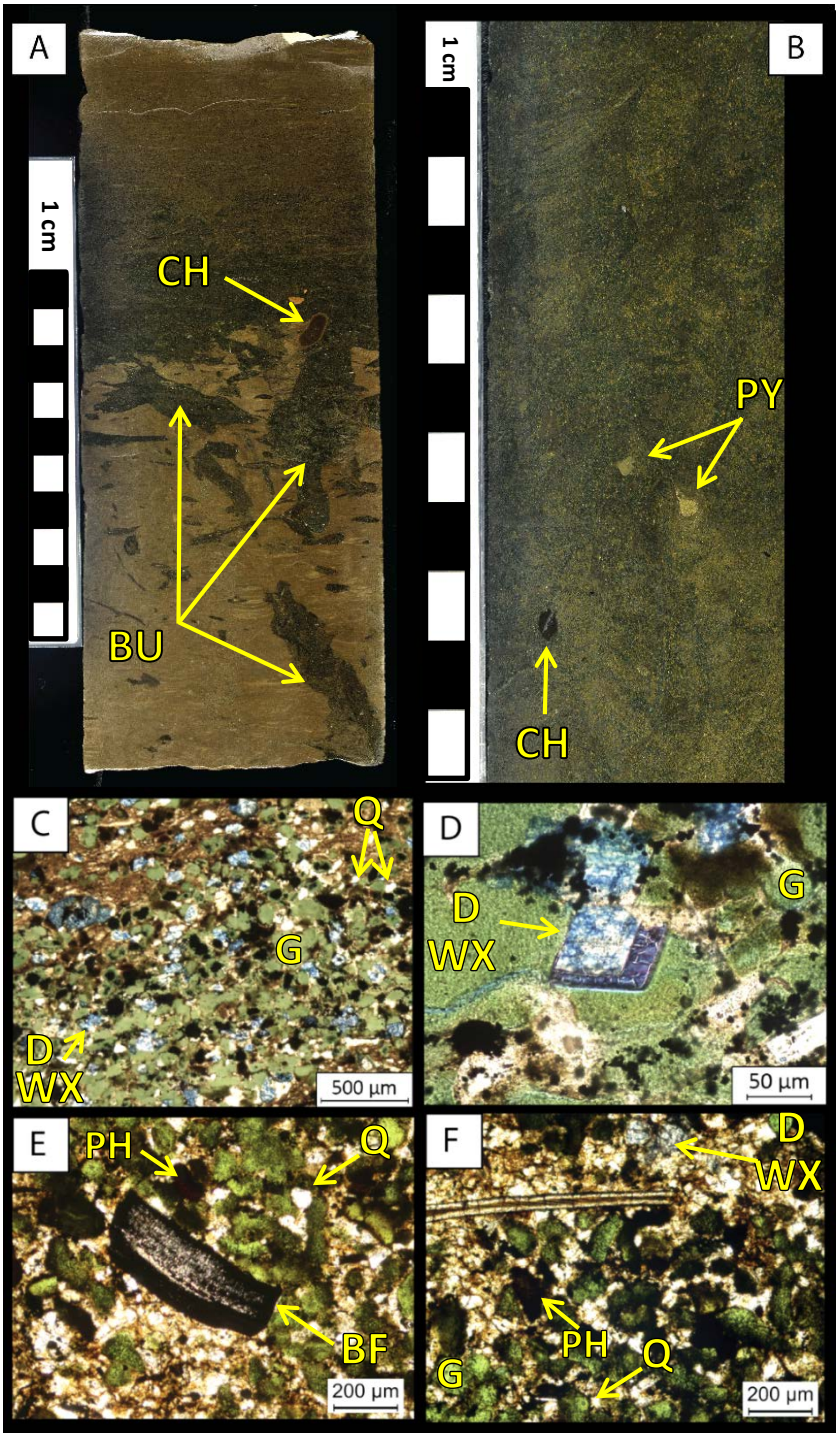

Figure 5. Glauconitic Sandstone (Facies 1). **A-B)** Facies 1 core photograph under white light from the Elinore core. Scale is in centimeters. Glauconite-rich sand in hand sample concentrated in centimeter-scale burrows (BU) and chert (CH) nodules. Photo B contains very coarse sand-sized scattered pyrite grains (PY) and chert (CH) nodules. **C-D)** Thin section photomicrograph of Facies 1 under white light with blue epoxy

impregnation. The sample contains silt- to very fine sand-sized quartz (Q) and glauconite (G) grains. Intracrystalline porosity (WX) within dolomite grains (D), possibly indicating dedolomitization (?) and interparticle porosity (blue) are evident. **E-F)** Thin section photomicrograph of Facies 1 under white light with blue epoxy impregnation. This thin section contains scattered phosphatic bone fragments (BF) and phosphate debris (PH). Quartz (Q) and glauconite (G) grains are present with minor interparticle porosity and intracrystalline (WX) porosity (blue) present within dolomite crystals (D). From LeBlanc (2014).

Facies 2: Burrowed Mudstone-Wackestone

The burrowed mudstone-wackestone facies (Figure 6) is characterized by a brownish black to grayish color, millimeter scale burrows, and presence of laminated mudstone. This facies contains silt-sized quartz (average 60%) with the presence of sponge spicules (5-10%), brachiopod fragments (5%), and thin crinoid beds (average 1 cm thick). Mineralogically, this facies is characterized by an average of 28% calcite, an average of 19% total clays (0.2% kaolinite, 15% illite/mica, 4% illite/smectite), and pyrite (average 2.8%). Facies 1 is observed in all three cores and contains moldic pores, an average porosity of 2.5% (minimum 1.1%, maximum 7.16%), and an average permeability of 0.05 mD (minimum 0.0001 mD, maximum 0.2 mD). Facies 2 was interpreted to have been deposited in an outer to distal outer ramp environment or in a low-energy, restricted environment.

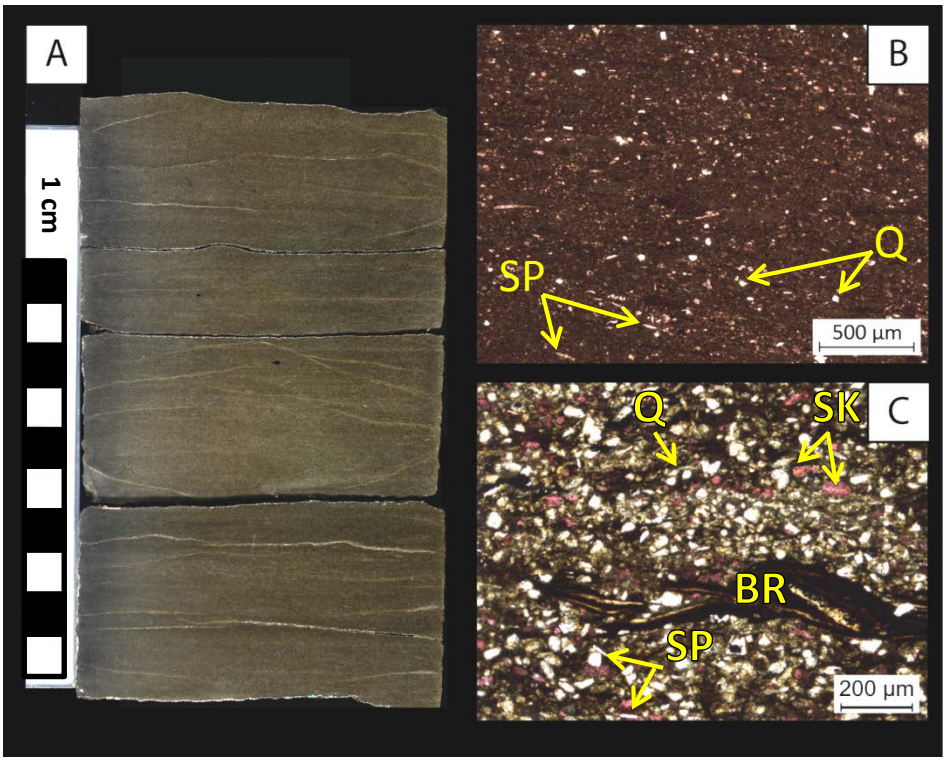

Figure 6. Burrowed Mudstone-Wackestone (Facies 2). **A)** Facies 2 core photograph from the Elinore core under white light. Scale is in centimeters. In hand sample, it is thinly bedded with some visible brachiopod and crinoid fragments. **B)** Thin section photomicrograph of Facies 2 under white light with alizarin red staining. The sample contains scattered calcareous grains (pink) throughout the muddy matrix as well as siliceous sponge spicules (SP) and silt-sized quartz grains (Q). **C)** Thin section photomicrograph of Facies 2 under white light. The sample contains abundant brachiopod fragments (BR), silt-sized quartz grains (Q), and calcareous skeletal fragments (SK) with scattered sponge spicule fragments (SP). From LeBlanc (2014).

Facies 3: Bioturbated Wackestone-Packstone

The bioturbated wackestone-packstone facies (Figure 7) contains silt-sized quartz grains (average 50%) and fine sand-sized peloids (average 40%). Sponge spicules (5%), crinoid fragments (10%), and brachiopods (5%) are also present. Mineralogically, the facies is characterized by an average of 42% calcite, an average of 9.3% total clays (6.5% illite/mica, 2.8% illite/smectite), and sparse pyrite grains (average 1.6%). This facies is a dusky yellowish brown color and is characterized by a bioturbation index of 1 (sparse) to 6 (heavy) (bioturbation index from Bann et al., 2008), with localized centimeter-scale burrows, moldic pores with an average porosity of 3.2% (minimum 0.43%, maximum 6.37), and an average permeability of 0.006 mD (minimum 0.0001 mD, maximum 0.07mD). Facies 3 is present in all three cores and was interpreted as being deposited in a mid- to outer-ramp environment.

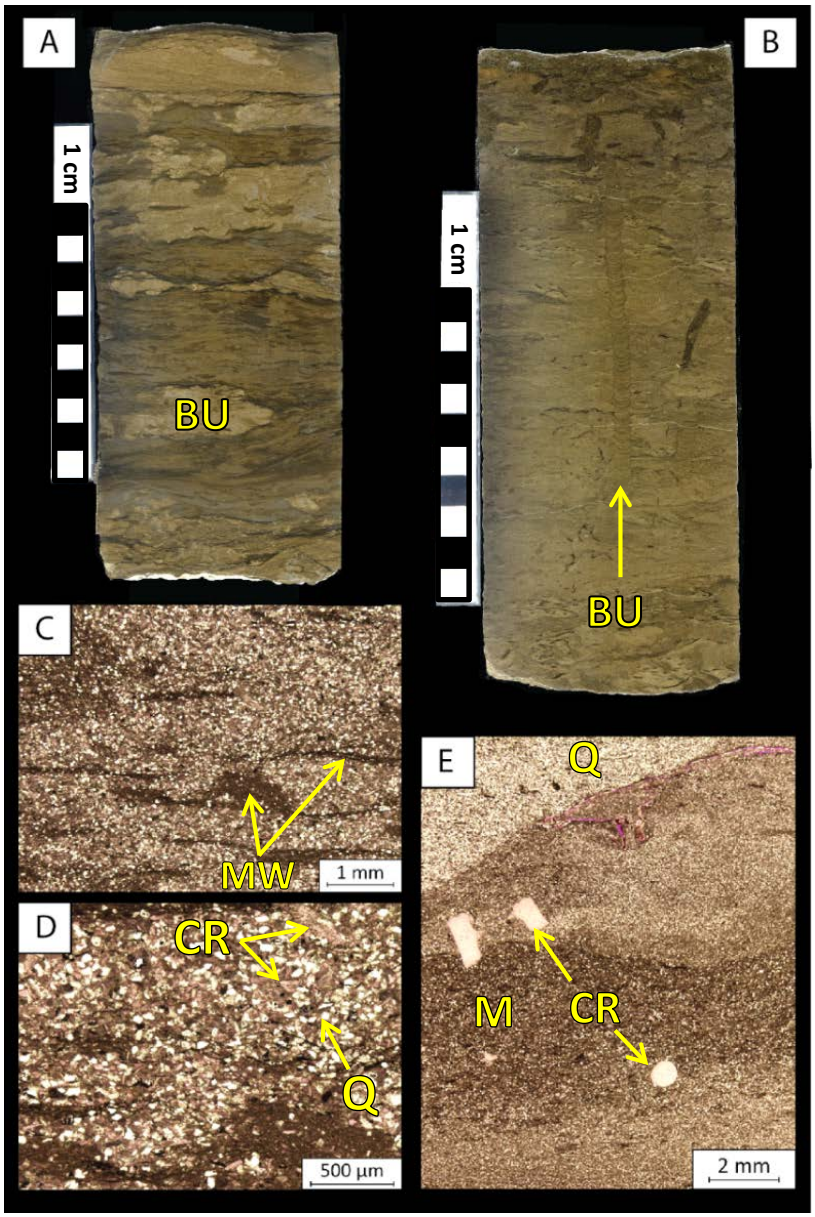

Figure 7. Bioturbated Wackestone-Packstone (Facies 3). **A-B)** Facies 3 core photograph under white light from the Winney core. Scale is in centimeters. Heavy bioturbation (bioturbation index of 6) and centimeter-scale burrows (BU) are visible in hand sample. **C-D)** Thin section photomicrograph of Facies 3 under white light at 2X (C) and 5X (D) with alizarin red staining. The sample is composed of silt-sized quartz grains (Q) and crinoid fragments (CR) and contains mud wisps (MW) throughout. **E)** Thin section photomicrograph of Facies 3 under white light with alizarin red staining. The sample is mud-supported (M) near the middle and bottom and grain-supported at the top and is

heavily bioturbated. Scattered crinoid fragments (CR) are present throughout the sample. From LeBlanc (2014).

Facies 4: Crinoidal Packstone-Grainstone

The crinoidal packstone-grainstone facies (Figures 8a and 8b) is a grain dominated facies (silt to fine sand-sized grains) characterized by silt to fine sand-sized quartz (average 40%) and sand-sized peloids (~50%). Abundant skeletal grains (~15%) consisting of crinoids, brachiopods and some bryozoan fragments are also present. Mineralogically, the facies consists of an average of 2% total clays (1.8% illite/mica, 0.2% illite/smectite), an average of 50% calcite, and sparse pyrite grains (average 0.3%). Facies 4 is variable in color, ranging from medium to dark grays and browns, contains moldic pores, vugs, and intraparticle porosity, has an average porosity of 3.2% (minimum 0.12%, maximum 11.4%), and has an average permeability of 0.009 mD (minimum 0.0001 mD, maximum 0.24 mD) . It is massive-bedded with intermittent cross-bedding, inclined bedding planes, and hummocky and swaley cross stratification and was interpreted to have been deposited in a mid-ramp environment or in a more distal portion of the ramp crest, within the influence of storm waves. Facies 4 is present in the Winney and Elinore cores, but is absent in the Orion Blackbird core.

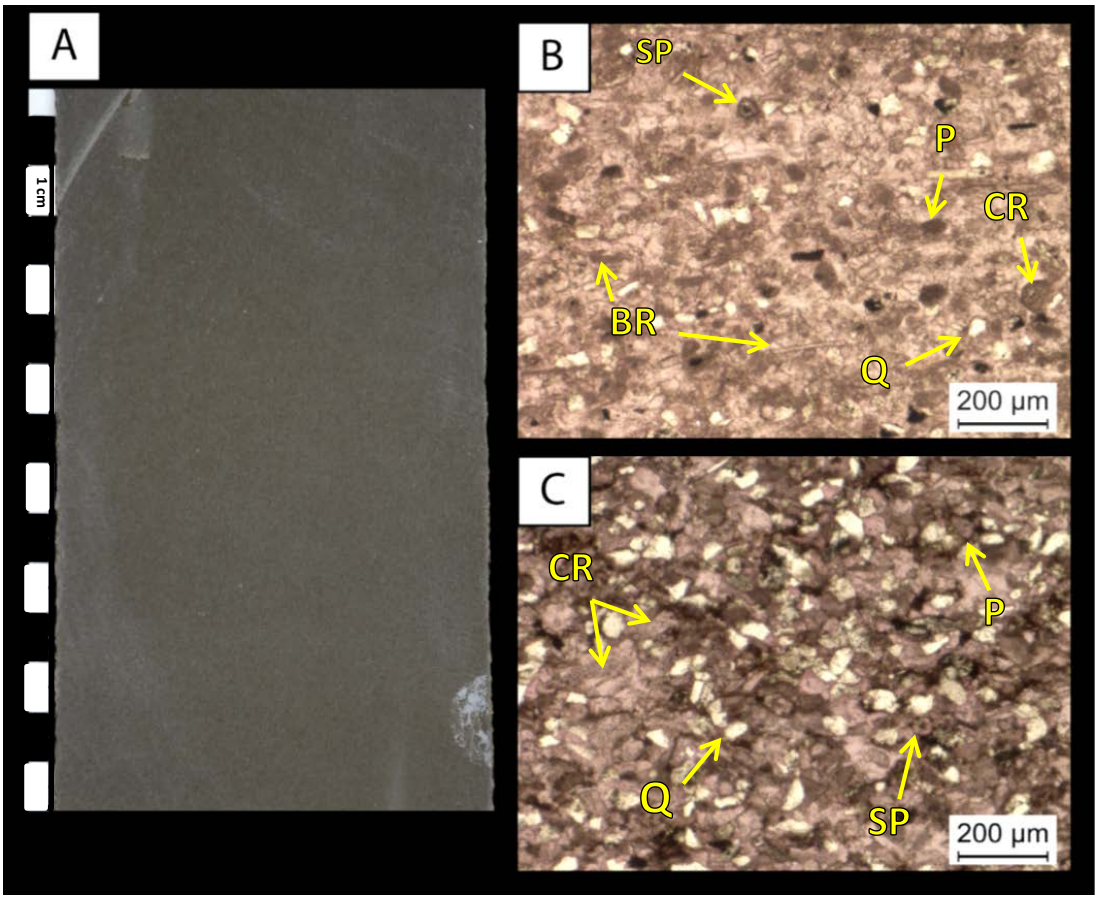

Figure 8a. Crinoidal Packstone-Grainstone (Facies 4). **A)** Facies 4 core photograph under white light from the Winney core. Scale is in centimeters. Facies 4 can be massively bedded in hand sample. **B-C)** Thin section photomicrographs of Facies 4 under white light with alizarin red staining. This sample is composed of brachiopod (BR) and crinoid (CR) fragments, sponge spicules (SP), fine sand-sized peloids (P) and silt-sized quartz grains (Q). From LeBlanc (2014).

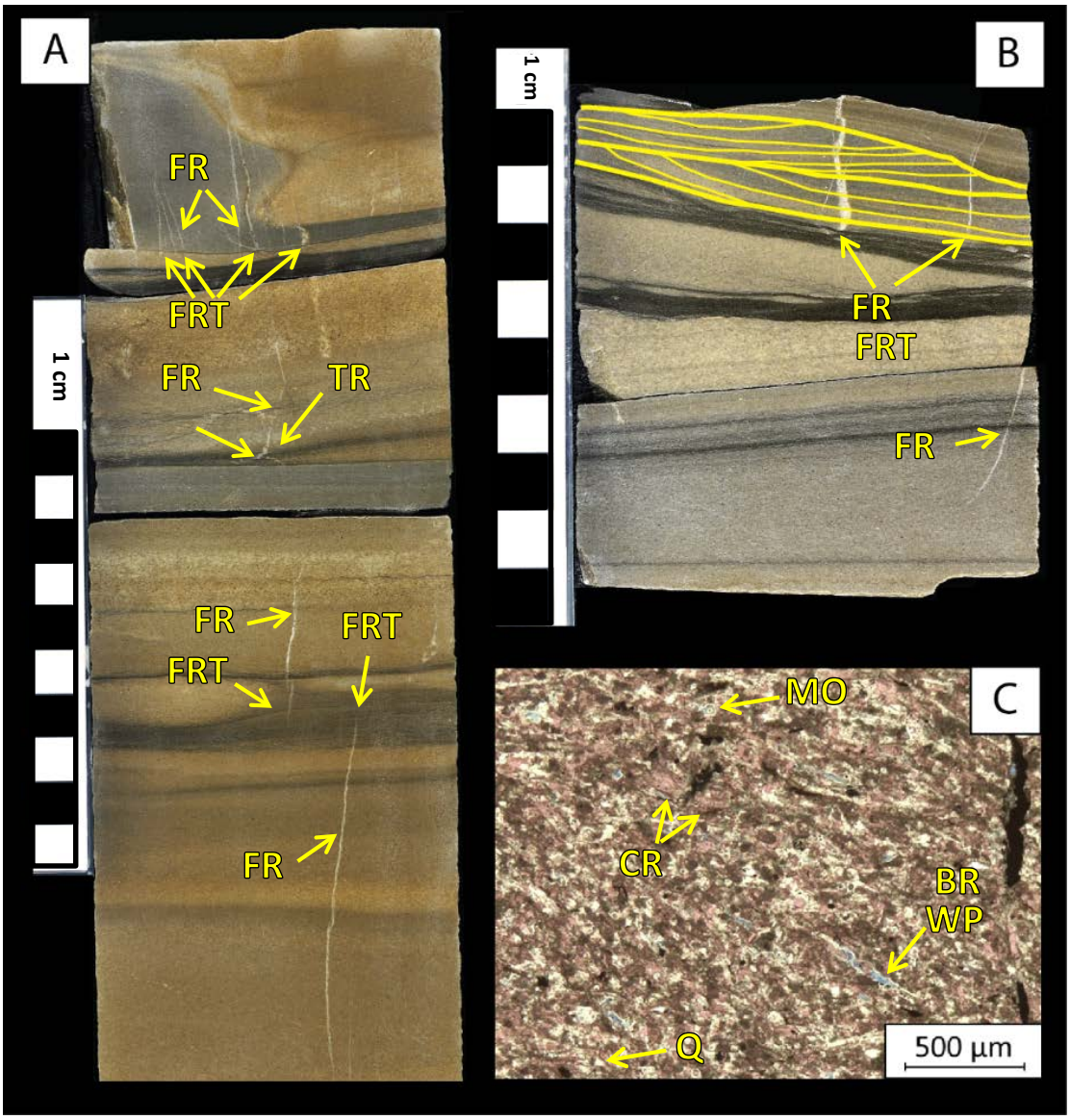

Figure 8b. Crinoidal Packstone-Grainstone (Facies 4). **A)** Facies 4 core photograph under white light from the Winney core. Scale is in centimeters. Traction current features with truncated surfaces (TR) are commonly observed in hand sample. Visible fractures (FR) as well as fracture terminations (FRT) are present in this sample. **B)** Facies 4 core photograph under white light. Scale is in centimeters. In hand sample, hummocky cross-stratification (outlined in yellow) is sporadically observed as well as visible fractures (FR) and fracture terminations (FRT). **C)** Thin section photomicrograph of Facies 4 in white light. This sample is composed of quartz grains (Q), brachiopod (BR) and crinoid (CR) fragments and contains intraparticle porosity (WP) as well as moldic porosity (MO). From LeBlanc (2014).

Fracture Types

Using fracture type characterization from Nelson (2001) and Cooper and Lorenz (2012), three fracture types were identified in core, which include: vertical extensional, and ptygmatic fractures. A fourth fracture type, "mixed" fractures, are characterized by the presence of both of the previously stated fracture types. Fracture type characterization is based on the morphological characteristics observed, which can be attributed to their associated stress regimes. Figure 9 illustrates the stress regimes associated with extensional (A) and shear (B and C) fracturing.

Vertical Extensional Fractures

Extension fractures have a sense of displacement perpendicular to and away from the fracture plane (Nelson, 2001). These fractures form parallel to σ_1 (maximum principal stress) and σ_2 (intermediate principal stress) and perpendicular to σ_3 (minimum principal stress) (shown as A on Figure 9). Characteristic indicators of extensional fractures include the absence of shear offsets and the presence of plume structures on the open fracture faces (Cooper and Lorenz, 2012). The vertical extensional fractures observed in this study commonly have partial mineralization by calcite or were completely separated with calcite mineralization present along the fracture walls. Figure 10 includes representative core photographs of vertical extensional fractures identified. A total of 270 vertical extensional fractures were identified in the entire subsurface dataset.

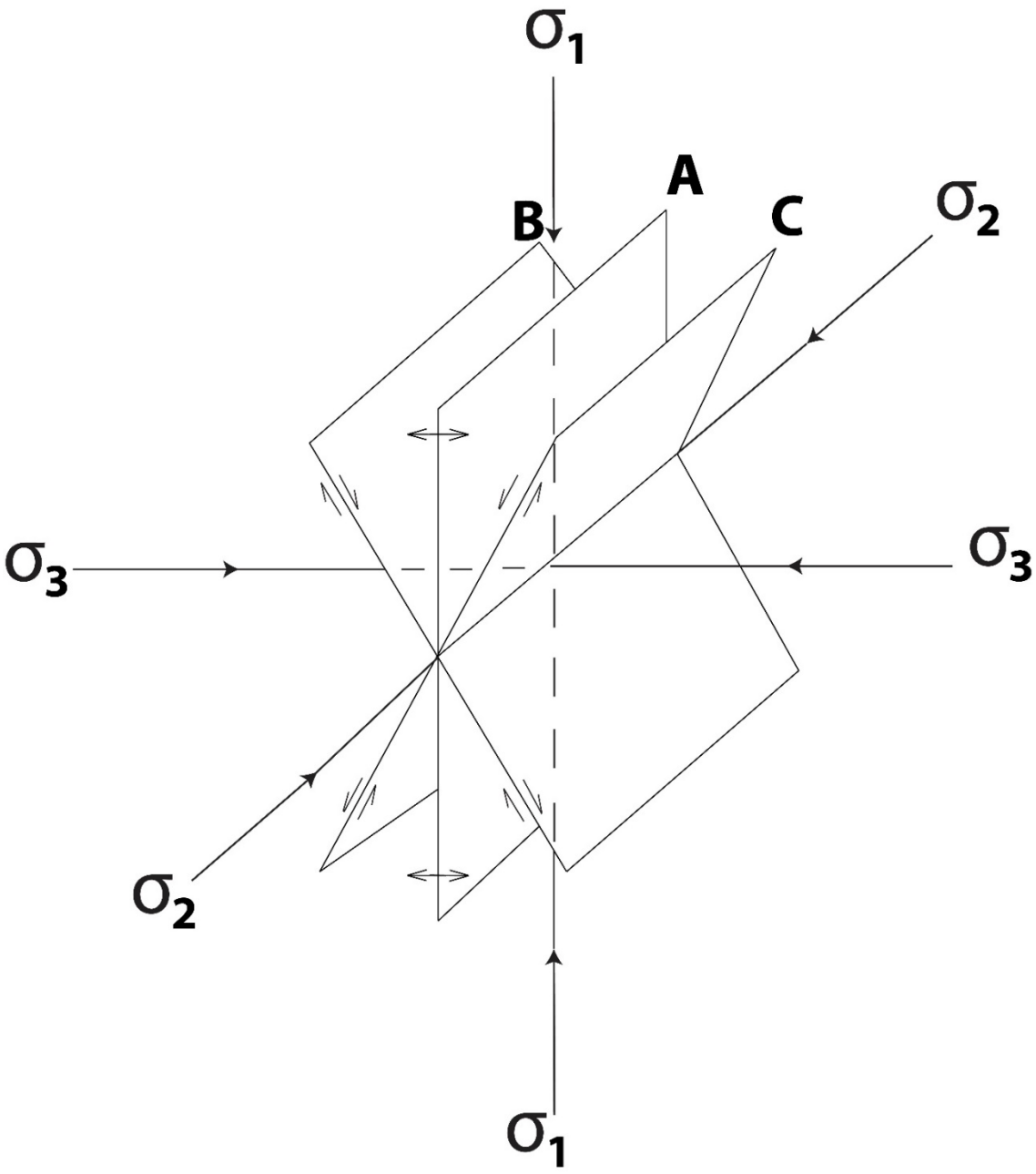

Figure 9. Diagram depicting extensional fractures (A), shear fractures (B and C), and their associated stress regimes ($\sigma_1, \sigma_2, \sigma_3$). σ_1 represents the maximum principal stress, σ_2 represents the intermediate principal stress, and σ_3 represents the minimum principal stress. Extensional fractures form parallel to σ_1 and σ_2 and perpendicular to σ_3. Shear fractures form at acute angles to σ_1 and obtuse angles to σ_3. Re-Drafted from Nelson (2001).

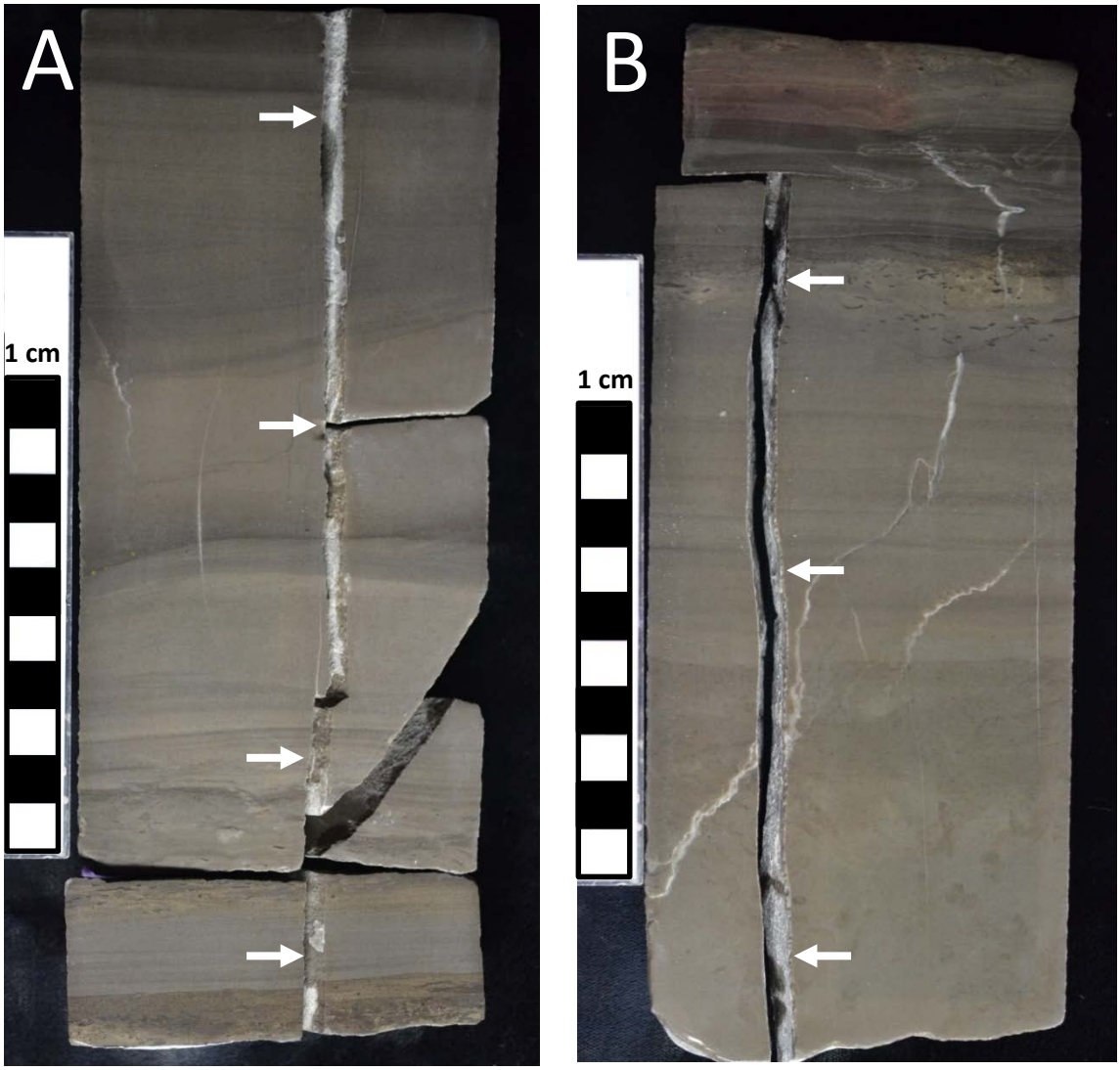

Figure 10. Extensional fractures (arrows) identified in the Winney core. **A)** Core photograph of an extensional fracture at a depth of 5227' in the crinoidal packstone-grainstone (Facies 4). Scale is in centimeters. The fracture is completely separated with the presence of calcite mineralization. **B)** Core photograph of an extensional fracture at a depth of 5225.4' in the crinoidal packstone-grainstone (Facies 4). This fracture is also completely separated and contains calcite mineralization along the fracture walls.

Ptygmatic Fractures

Ptygmatic refers to fractures that are intensely distorted or folded. There is uncertainty in how this type of fracture forms. Cooper and Lorenz (2012) suggest that ptygmatic fractures form as extensional fractures first and are compacted and subsequently folded. The fractures are interpreted to have occurred when the sediment was brittle enough to fracture, but soft enough for significant ductile deformation to occur. The ptygmatic fractures seem to have the most distortion (folding) in the muddier facies, similar to what has been reported by Gross (1995) and Cooper and Lorenz (2002). A total of 700 ptygmatic fractures were present in all three cores combined, making ptygmatic fractures the most abundant fracture type. These fractures are completely mineralized with calcite, commonly terminate at one or both ends at more ductile muddier layers, and may display multiple broken vertical fracture segments from intense folding (Figures 11 and 12).

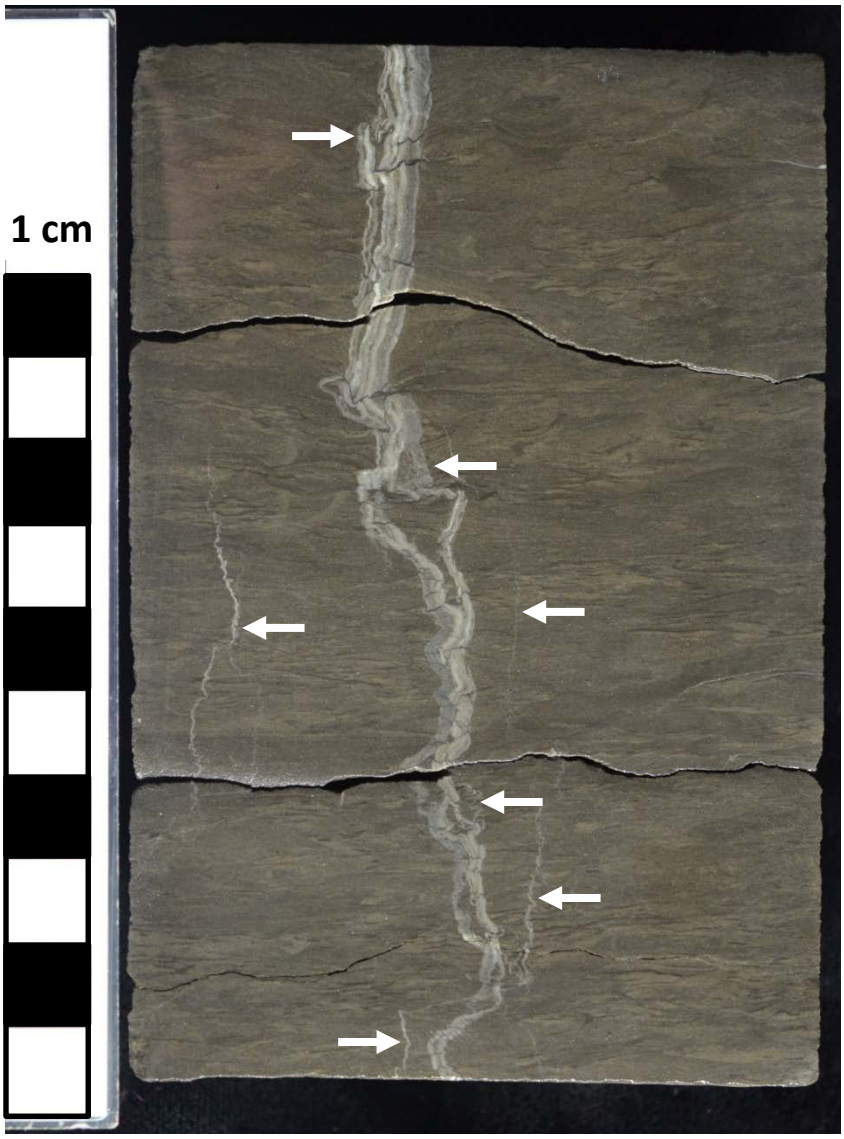

Figure 11. Ptygmatic fractures (arrows) identified in the Elinore core at a depth of 4477' in the burrowed mudstone-wackestone (Facies 2). Scale is in centimeters. Each ptygmatic fracture in this sample is mineralized and was identified by the presence of the characteristic folding along the fracture plane. There are likely multiple zones of cement present in the larger fracture and this fracture may also be made up of multiple fractures. The smaller fractures terminate at specific layers within the mottled fabric.

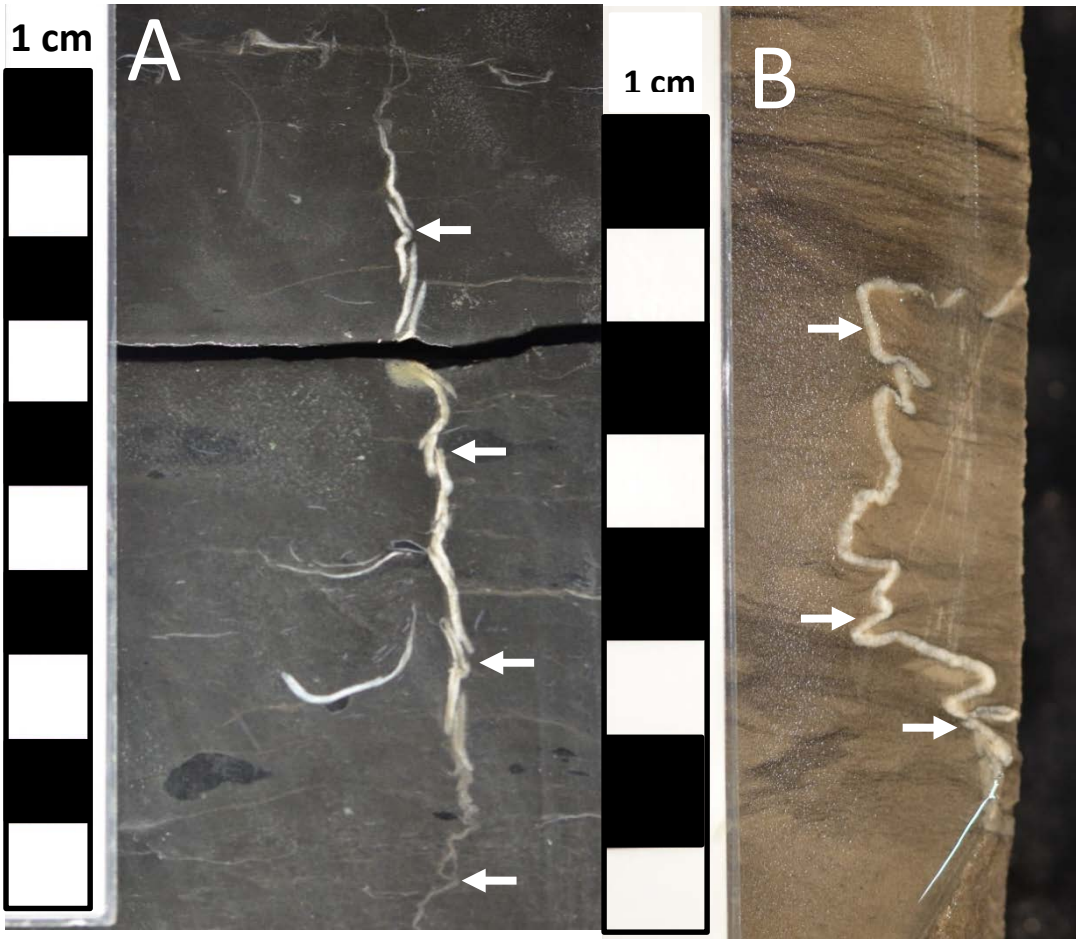

Figure 12. Ptygmatic fractures (arrows) identified in the Winney and Orion Blackbird cores. **A)** Core photograph in the Winney core at a depth of 5161.5' in the burrowed mudstone-wackestone (Facies 2). Scale is in centimeters. The fracture is heavily folded throughout the length of the fracture and the top half of the fracture was folded to the point of breaking into smaller vertical segments. **B)** Core photograph of a ptygmatic fracture identified in the Orion Blackbird core at a depth of 3215.8' in the bioturbated wackestone-packstone (Facies 3). The arrows indicate the ptygmatic fracture with calcite mineralization and visible folding along the fracture plane.

Mixed Fractures

In some cases, fracture characterization and identification could not be determined when the presence of two fracture types occurred within a single fracture. These fractures were identified as a mixed fracture type: extensional and ptygmatic. Figures 13 and 14 illustrate examples of mixed fracture types in core that display characteristics of extensional and ptygmatic fracturing.

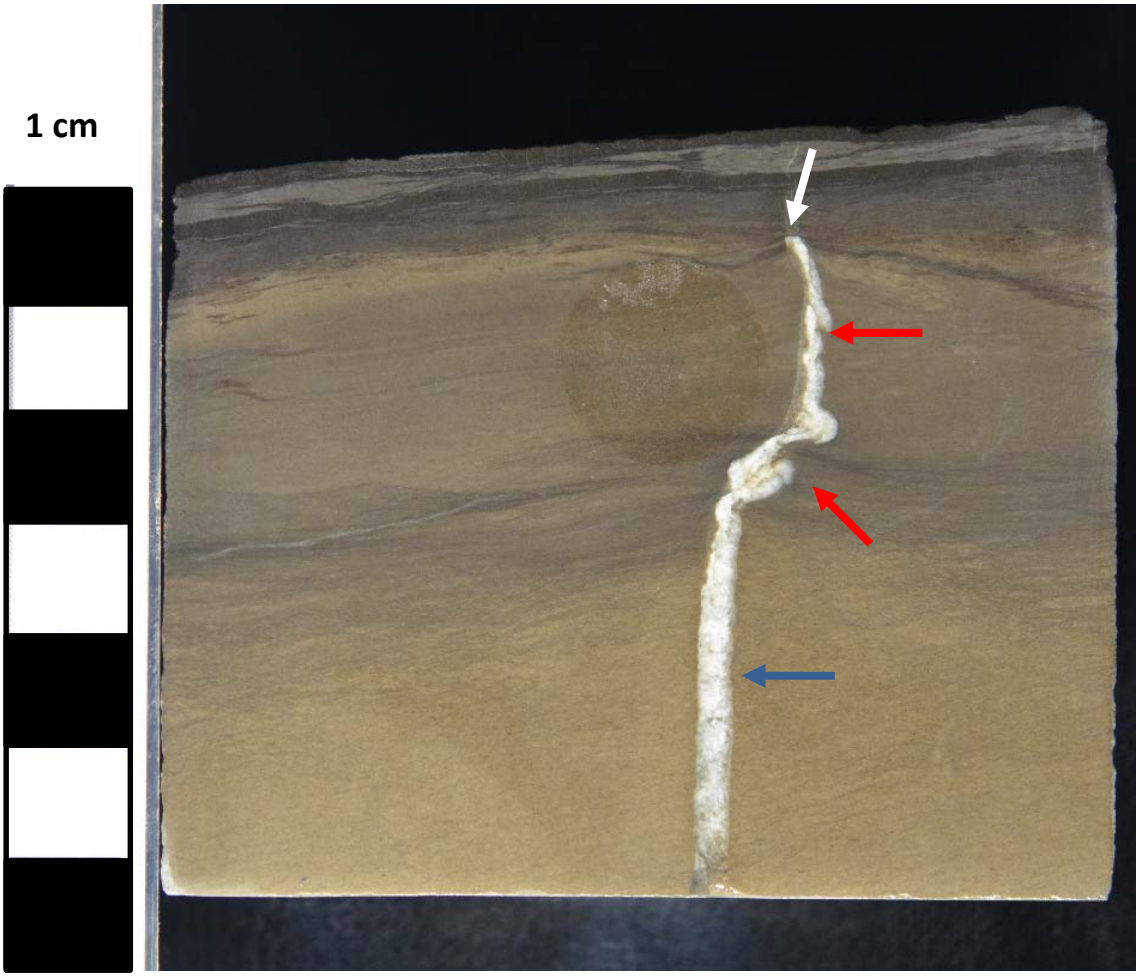

Figure 13. Core photo of a mixed fracture in the Winney core at a depth of 5263.8'. The extensional portion of the fracture is indicated by the blue arrow and the ptygmatic portions are indicated by the red arrows. The fracture is mineralized with calcite,

terminates at a darker layer (indicated by the white arrow), and is more heavily folded in the darker material that intervenes towards the middle of the photo.

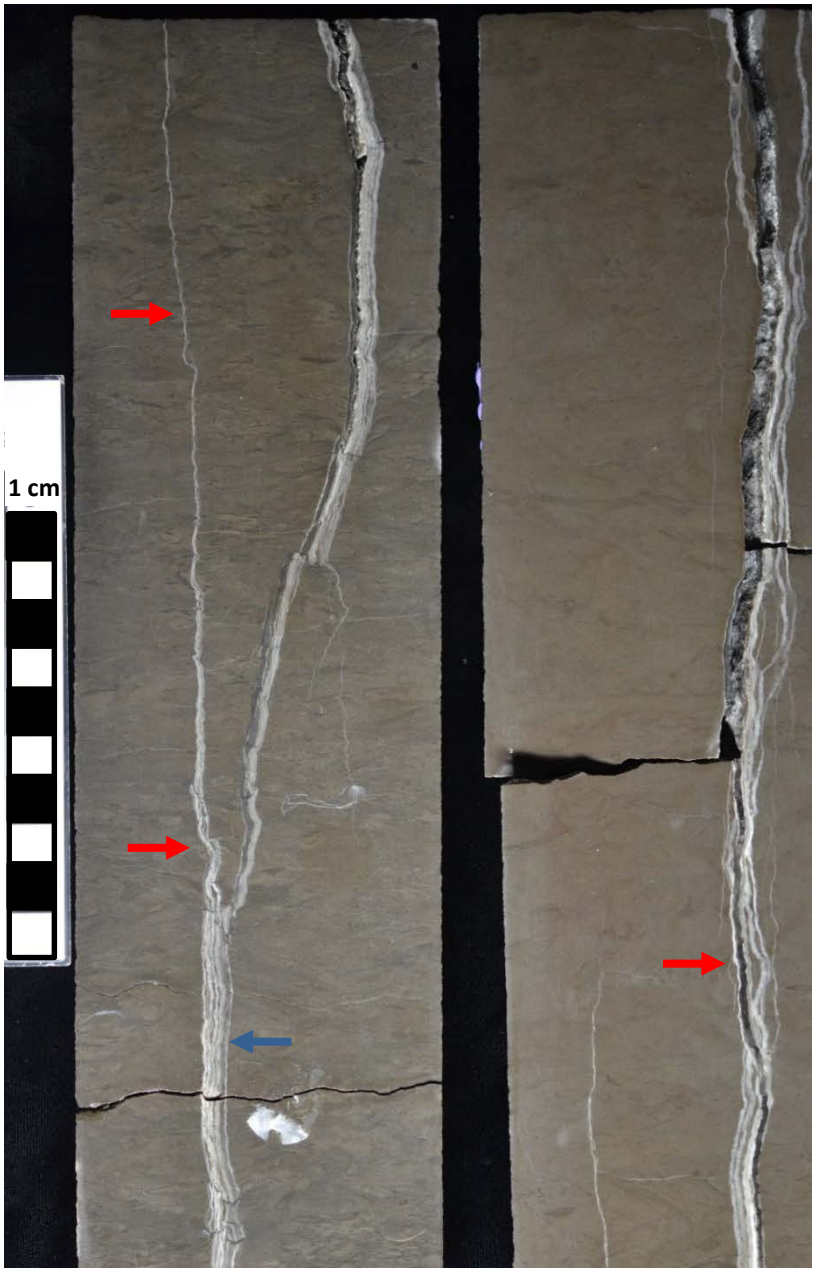

Figure 14. Mixed fracture (extensional and ptygmatic) identified in the Elinore core at a depth of 4475' in the bioturbated wackestone-packstone (Facies 3). Scale is in centimeters. The arrows indicate the fracture plane. The top of the fracture is located at the top of the left core interval in the photo and the bottom of the fracture is located at the bottom of the right core interval. This calcite filled fracture displays characteristics of extensional and ptygmatic fracturing. The blue arrow indicates an

extensional section of the fracture. The red arrows indicate ptygmatic portions of the fracture where the fracture plane has been folded.

Natural vs. Induced Fractures

Natural fractures are the fractures that exist in the rock before any coring or drilling occurs. Induced fractures are those that are created during drilling, coring, and subsequent core handling. It can be difficult at times to distinguish between natural and induced fractures. Kulander et al. (1990), Lorenz et al. (1990), and Nelson (2001) discuss distinguishing characteristics of natural and induced fractures in core analysis.

The primary indicator of natural fractures used for this study was the presence of mineralization. If mineralization was present on a fracture plane, the fracture was identified as natural. Induced fractures were identified based on common morphological characteristics outlined in Kulander et al. (1990), Lorenz et al. (1990), and Nelson (2001). Induced fractures commonly seen in the cores include petal-centerline, scribe-knife, and disc fractures.

Fracture Types Related to Facies

Ptygmatic fractures are the most abundant fracture type in the cores overall, with vertical extensional fractures being the second most abundant. The Elinore and Winney cores (Figures 15a and 15b) have the most abundant ptygmatic and vertical extensional fractures (113 total ptygmatic and 50 total vertical extensional in the Elinore; 89 total ptygmatic and 48 total vertical extensional in the Winney) in the crinoidal packstone – grainstone facies (Facies 4). The Orion Blackbird core (Figure 15c)

does not have the crinoidal packstone – grainstone facies or the glauconitic sandstone facies present, however, the same general trend exists with the ptygmatic and vertical extensional fracture populations being most abundant in the grainier facies. The bioturbated wackestone-packstone (Facies 3) has more ptygmatic and vertical extensional fractures (321 total ptygmatic and 137 total vertical extensional) compared to the burrowed mudstone-wackestone (Facies 2).

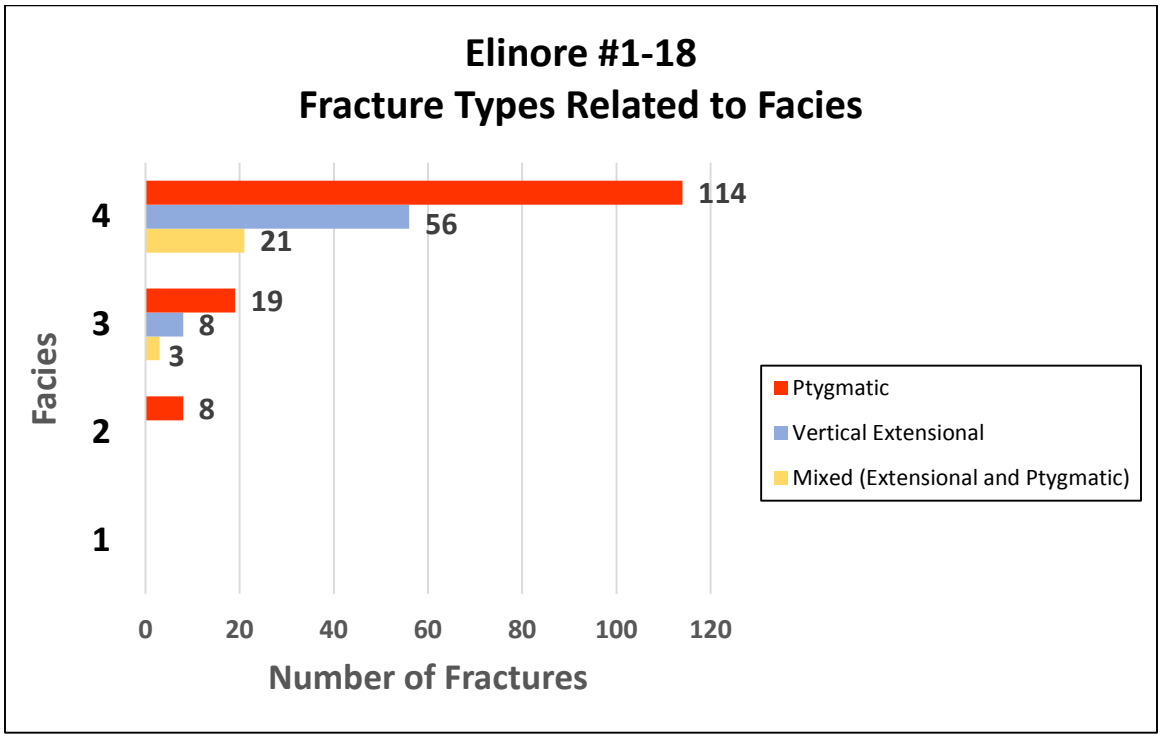

Figure 15a. Graph of fracture types and frequency plotted by petrophysically-significant facies type in the Elinore core. Number of fractures is plotted on the x-axis and facies types are plotted on the y-axis. Fracture populations for each facies are color coded by fracture type. Facies 4 (crinoidal packstone-grainstone) contains the largest number of ptygmatic and extensional fractures. The number of ptygmatic fractures decreases from Facies 4 to Facies 1.

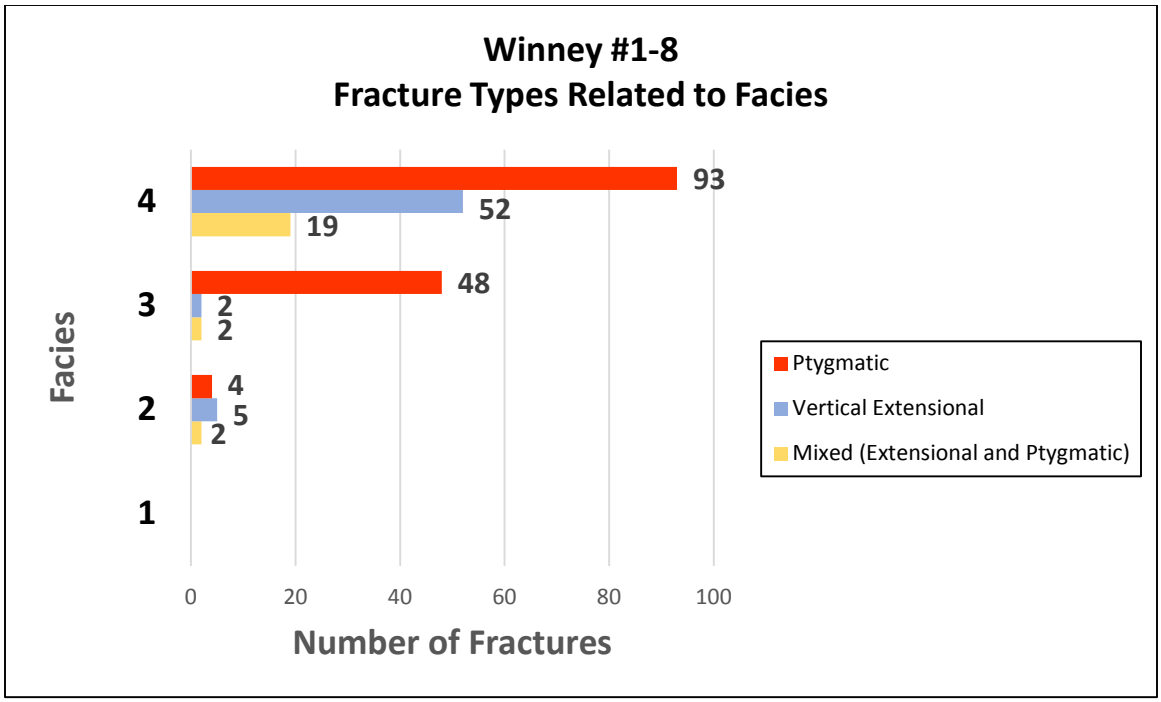

Figure 15b. Graph of fracture types and frequency plotted by petrophysically-significant facies type in the Winney core. Number of fractures is plotted on the x-axis and facies types are plotted on the y-axis. Fracture populations for each facies are color coded by fracture type. Facies 4 (crinoidal packstone-grainstone) contains the largest number of ptygmatic and extensional fractures. The number of ptygmatic fractures decreases from Facies 4 to Facies 1.

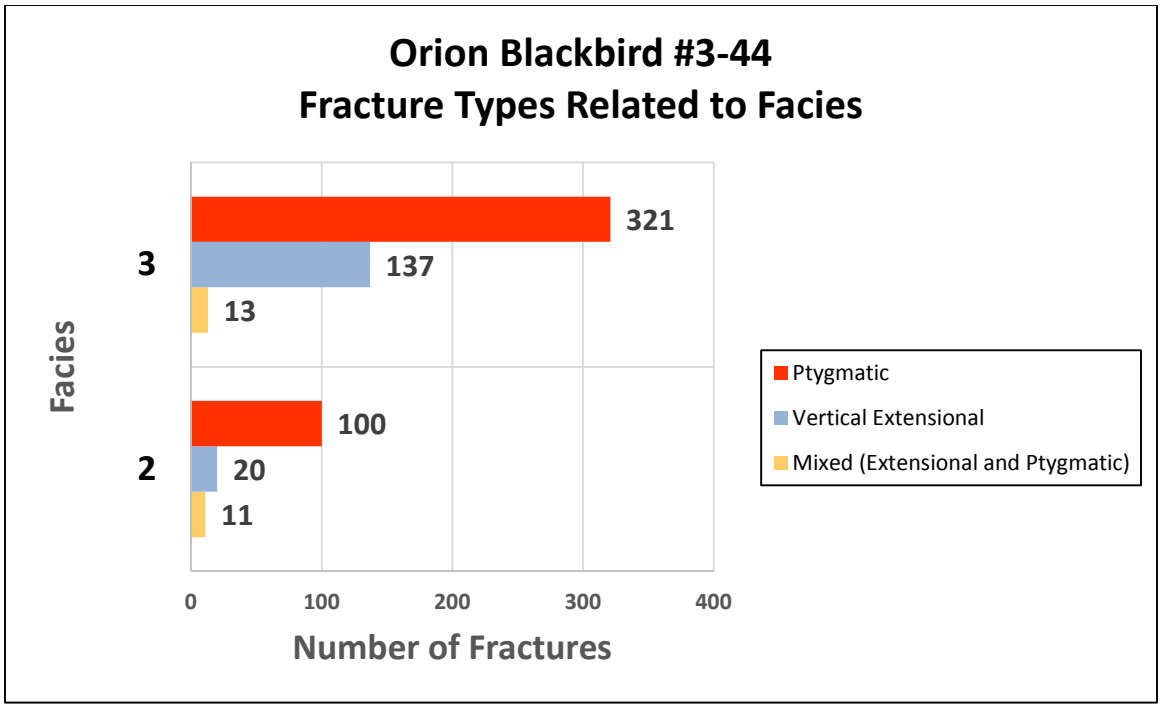

Figure 15c. Graph of fracture types and frequency plotted by petrophysically-significant facies type in the Orion Blackbird core. Number of fractures is plotted on the x-axis and facies types are plotted on the y-axis. Fracture populations for each facies are color coded by fracture type. Unlike the Elinore and Winney, Facies 4 (crinoidal packstone-grainstone) and Facies 1 (glauconitic sandstone) are absent. Facies 3 (bioturbated wackestone-packstone) has the largest number of ptygmatic and extensional fractures. The number of ptygmatic fractures decreases from Facies 3 to Facies 2.

Overall, the Winney and Elinore cores exhibit similar numbers of ptygmatic and vertical extensional fractures in each petrophysically-significant facies. Comparing these values to the Orion Blackbird values, Facies 2 and Facies 3 in the Orion core have much higher numbers of ptygmatic and vertical extensional fractures than those same facies types in the Winney and Elinore cores. To be certain that these numbers are not higher because the core is longer and therefore had more total footage of Facies 2 and Facies 3 present, Figure 16 displays the average fracture densities (normalized) for ptygmatic and vertical extensional fractures in the studied cores. The Orion Blackbird still exhibits higher vertical extensional and ptygmatic average fracture densities than Facies 2 and Facies 3 in the Elinore and Winney.

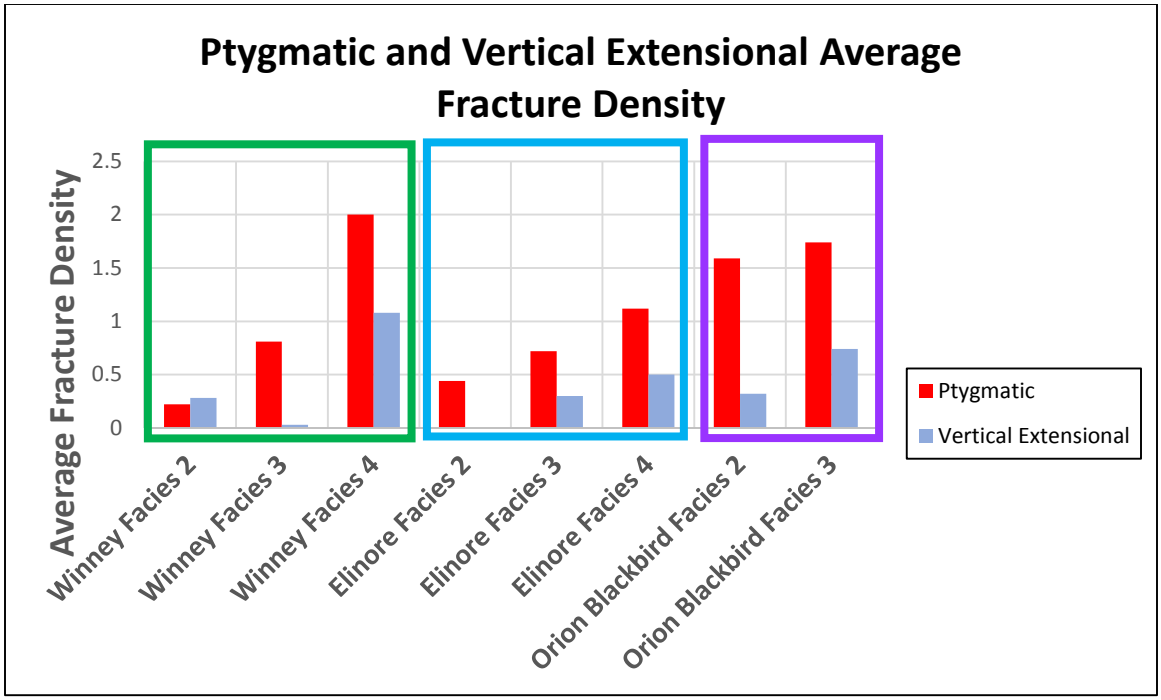

Figure 16. Average fracture densities of ptygmatic and vertical extensional fractures graphed by facies types in the studied cores. The green box represents the Winney core, the blue box represents the Elinore core, and the purple box represents the Orion Blackbird core. In general, the average fracture density of ptygmatic and vertical

extensional fractures increases from Facies 2 (burrowed mudstone-wackestone) to Facies 4 (crinoidal packstone-grainstone). The Orion Blackbird core exhibits higher ptygmatic and vertical extensional fracture densities when compared to Facies 2 (burrowed mudstone-wackestone) and Facies 3 (bioturbated wackestone-packstone) in the Winney and Elinore cores.

Fracture Density Related to Facies

Average fracture density calculations for each facies used the total footage of each facies in core divided by the total number of fractures in each facies and were utilized to infer predictive trends of fracturing. In the Elinore and Winney cores (Figures 17a and 17b), average fracture density increases as the facies become grainier from the glauconitic sandstone (Facies 1) to the crinoidal packstone-grainstone (Facies 4). Facies 4 has the highest average fracture density (1.95 fractures per foot in the Elinore; 1.46 fractures per foot in the Winney). As mentioned previously, the Orion Blackbird core (Figure 17c) does not have the crinoidal packstone – grainstone (Facies 4) or the glauconitic sandstone (Facies 1) present. However, the Orion core has the same general trend of increasing average fracture density as the facies become grainier, with the bioturbated wackestone-packstone (Facies 3) having a higher average fracture density (2.92 fractures per foot) than the burrowed mudstone-wackestone (Facies 2).

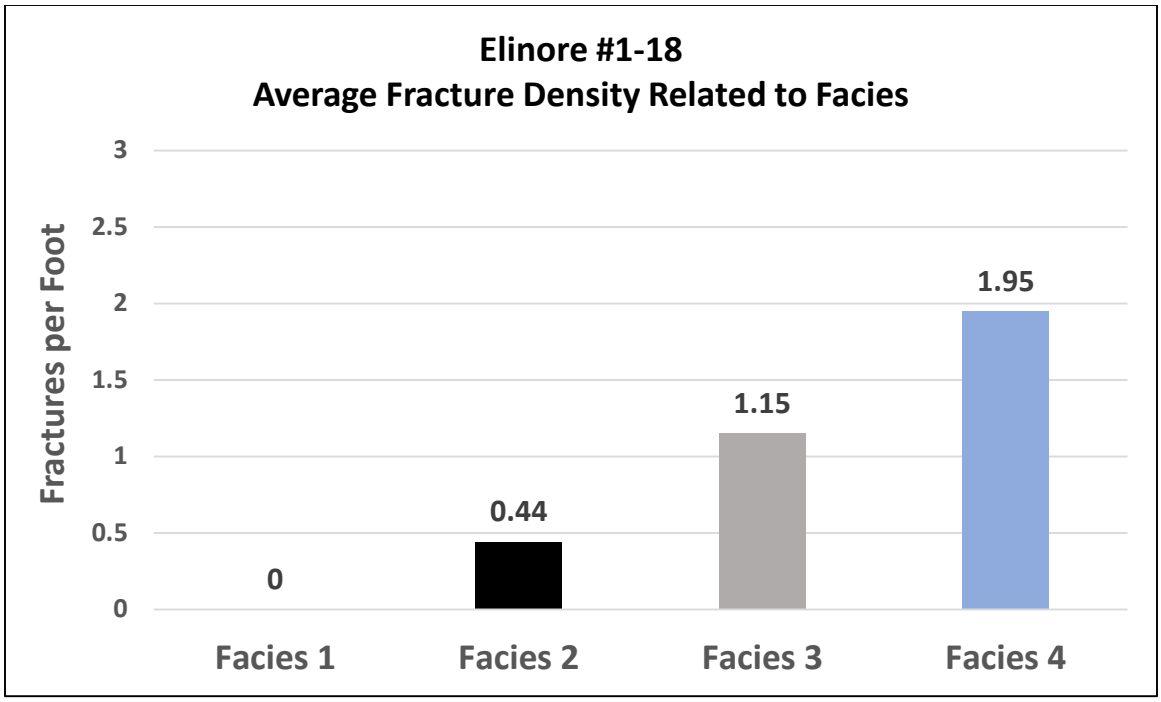

Figure 17a. Graph of average fracture density in each petrophysically-significant facies in the Elinore core. Facies are plotted on the x-axis and fractures per foot (fracture density) is plotted on the y-axis. Fracture density values increase as the facies become grainier from Facies 1 (glauconitic sandstone) to Facies 4 (crinoidal packstone-grainstone). Facies 4 has the highest average fracture density.

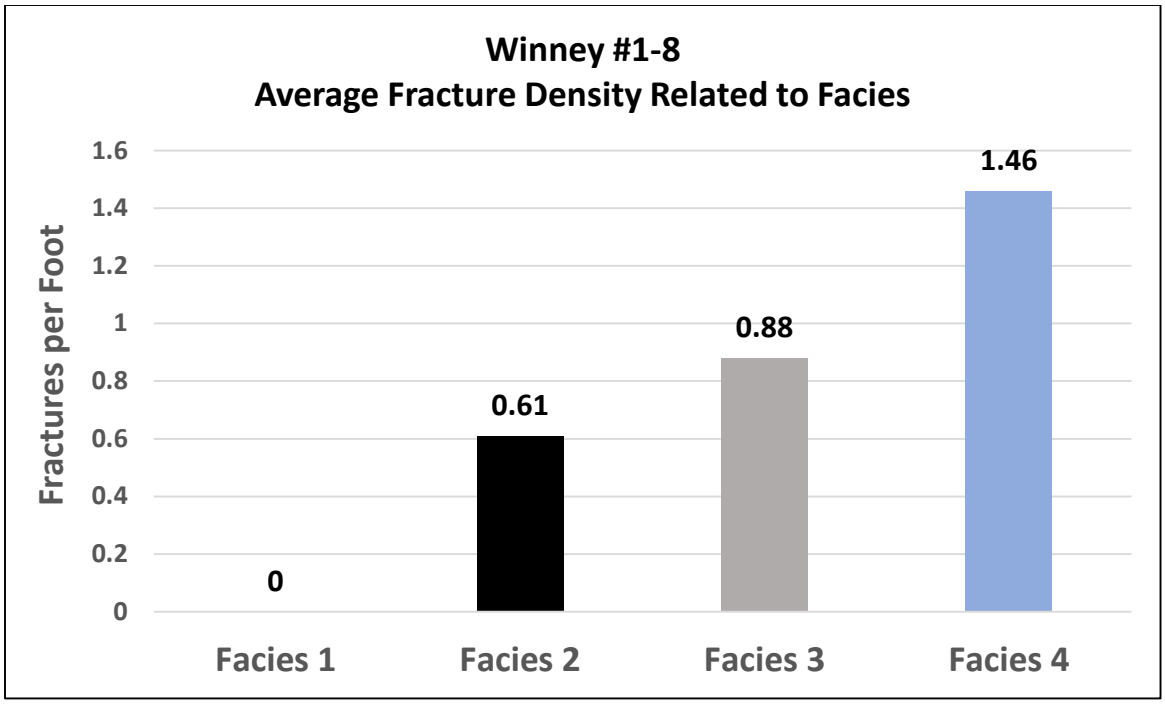

Figure 17b. Graph of average fracture density in each petrophysically-significant facies in the Winney core. Facies are plotted on the x-axis and fractures per foot (fracture density) is plotted on the y-axis. Fracture density values increase as the facies become grainier from Facies 1 (glauconitic sandstone) to Facies 4 (crinoidal packstone-grainstone). Facies 4 has the highest average fracture density.

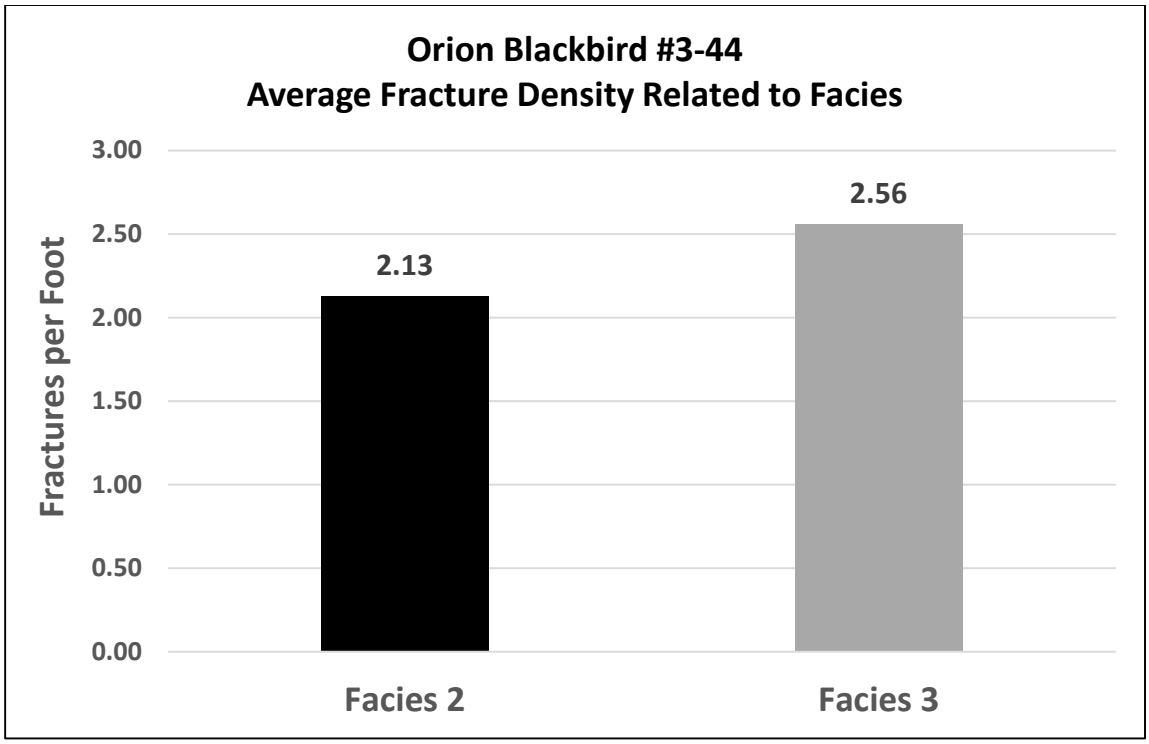

Figure 17c. Graph of average fracture density in each petrophysically-significant facies in the Orion Blackbird core. Facies are plotted on the x-axis and fractures per foot (fracture density) is plotted on the y-axis. The glauconitic sandstone (Facies 1) and the crinoidal packstone-grainstone (Facies 4) are absent in the Orion Blackbird. However, the same general trend observed in the Elinore and Winney cores is evident. Fracture density is increasing as facies become grainier from Facies 2 (burrowed mudstone-wackestone) to Facies 3 (bioturbated wackestone-packstone).

Fractures Related to Sequence Stratigraphic Framework

Each of the cores exhibit probable 2nd, 3rd, and 4th order cyclicity defined by Leblanc (2014) and Vanden Berg (2016). In each of the cores, the entire cored interval has been interpreted to represent one 2nd order sequence. The Winney exhibits four 3rd order sequences, the Elinore exhibits three, and the Orion Blackbird core exhibits six. A number of high frequency 4th order sequences were also defined in each core. Trends were analyzed between fractures and the 3rd order sequences, but were not analyzed

between the fractures and the various 4th order cycles due to the uncertainty as to the controlling mechanism of these cycles, making these cycles highly problematic for correlation.

The Winney and Elinore (Figures 18 and 19) exhibit similar trends between the 3rd order sequences and average fracture density. The regressive phases of sequences 1, 2, and 3 in the Winney and sequences 1 and 2 in the Elinore have higher fracture density values than the transgressive phases of these sequences. The sequence at the top of each core (sequence 4 in the Winney and Sequence 3 in the Elinore) illustrate a higher fracture density value in the transgressive phase when compared to the regressive phase. Trends in the 3rd order sequences and fracture types are also similar in both the Winney and Elinore cores where higher numbers of ptygmatic and vertical extensional fractures are present in the regressive phases when compared to the associated transgressive phases.

The Orion Blackbird (Figure 20) has six 3rd order sequences that exhibit higher fracture density values in sequences 1, 2, 3, and 5 in the transgressive portions. Sequence 6 is the only sequence in which the regressive phase has a higher average fracture density than the transgressive phase. Unlike the Winney and Elinore cores, the transgressive phases in sequences 1, 2 and 3 have a higher number of ptygmatic fractures than in the regressive phases, likely due to the difference in facies distribution within the sequences in the Orion core compared to the Winney and Elinore cores.

Apart from sequences 1 and 5, the regressive portions of the sequences exhibit a higher number of vertical extensional fractures than the transgressive portions.

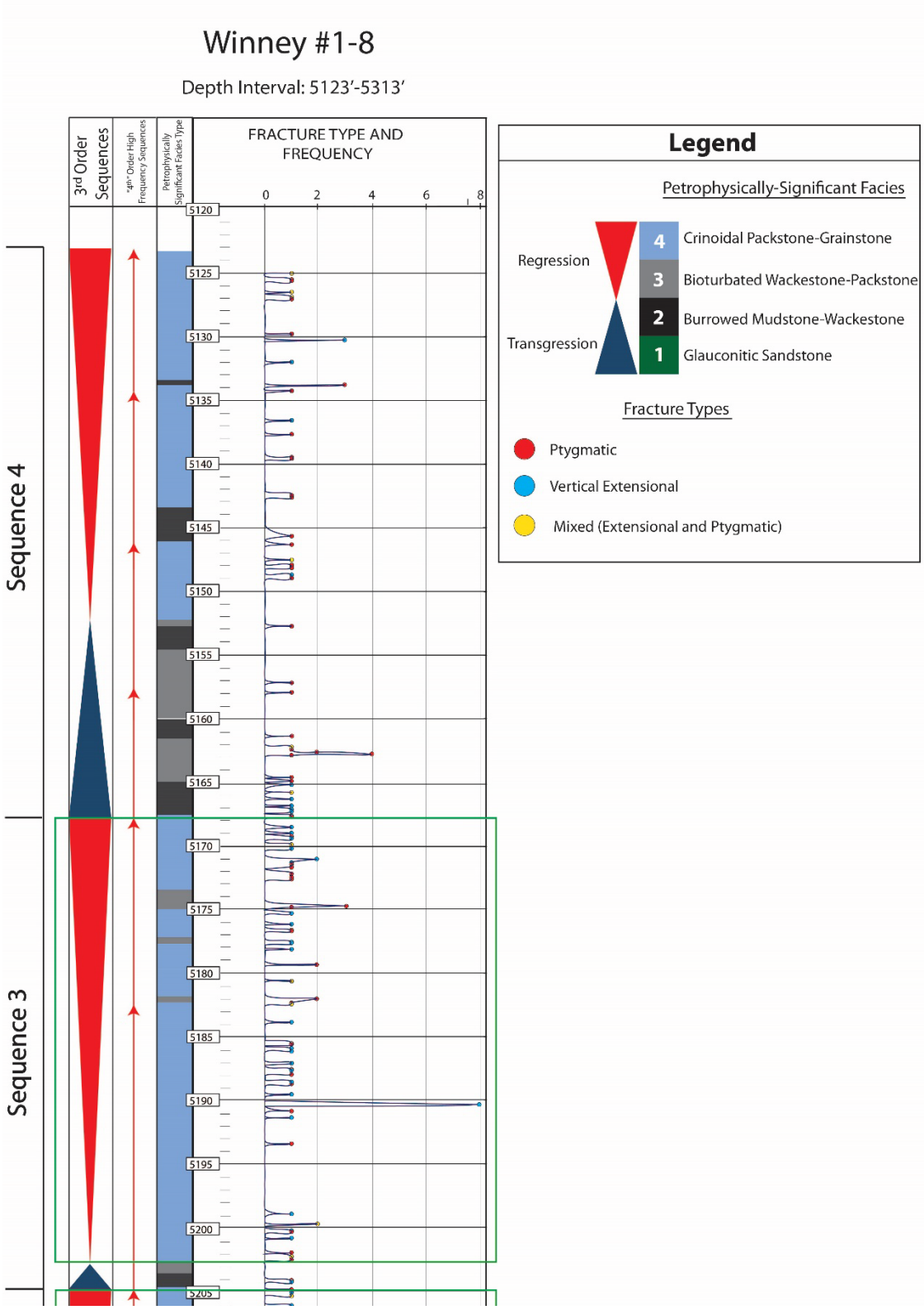
Winney #1-8
Depth Interval: 5123'-5313'
3rd Order Sequences
"4th" Order High Frequency Sequences
Petrophysically Significant Facies Type
FRACTURE TYPE AND FREQUENCY
0
2
4
6
8
5120
5125
5130
5135
5140
5145
5150
5155
5160
5165
5170
5175
5180
5185
5190
5195
5200
5205
Sequence 4
Sequence 3
Legend
Petrophysically-Significant Facies
Regression
Transgression
4 Crinoidal Packstone-Grainstone
3 Bioturbated Wackestone-Packstone
2 Burrowed Mudstone-Wackestone
1 Glauconitic Sandstone
Fracture Types
Ptygmatic
Vertical Extensional
Mixed (Extensional and Ptygmatic)

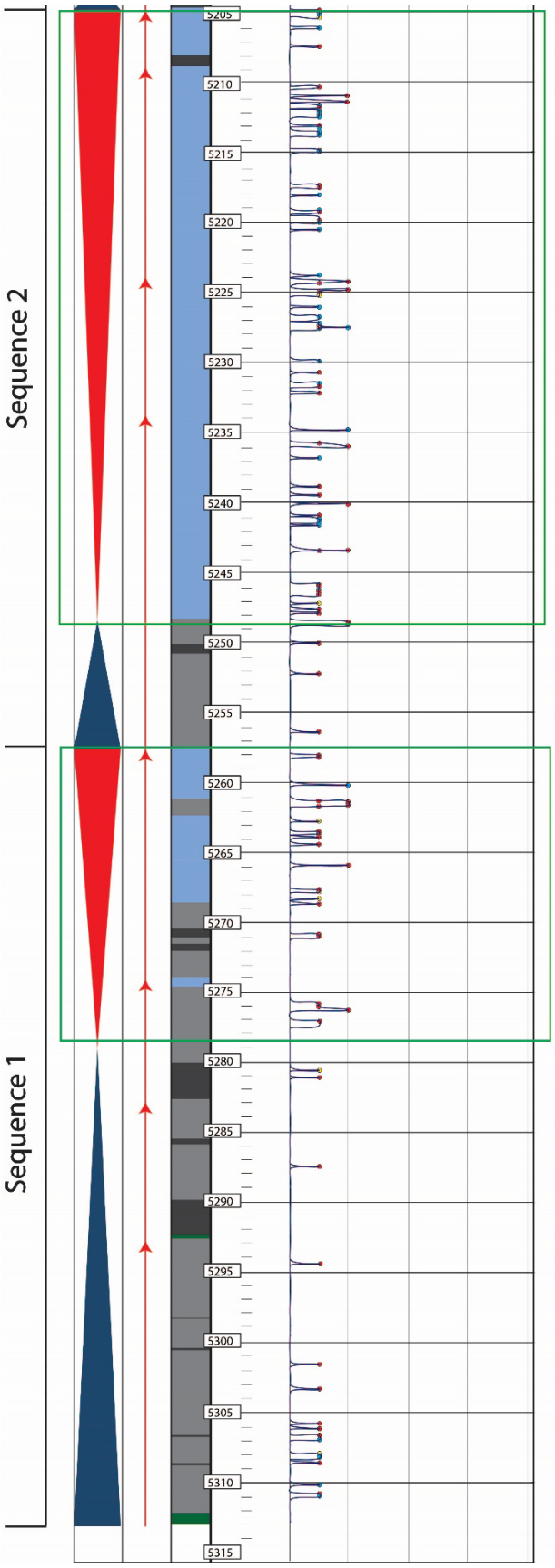
Sequence 2
Sequence 1
5205
5210
5215
5220
5225
5230
5235
5240
5245
5250
5255
5260
5265
5270
5275
5280
5285
5290
5295
5300
5305
5310
5315

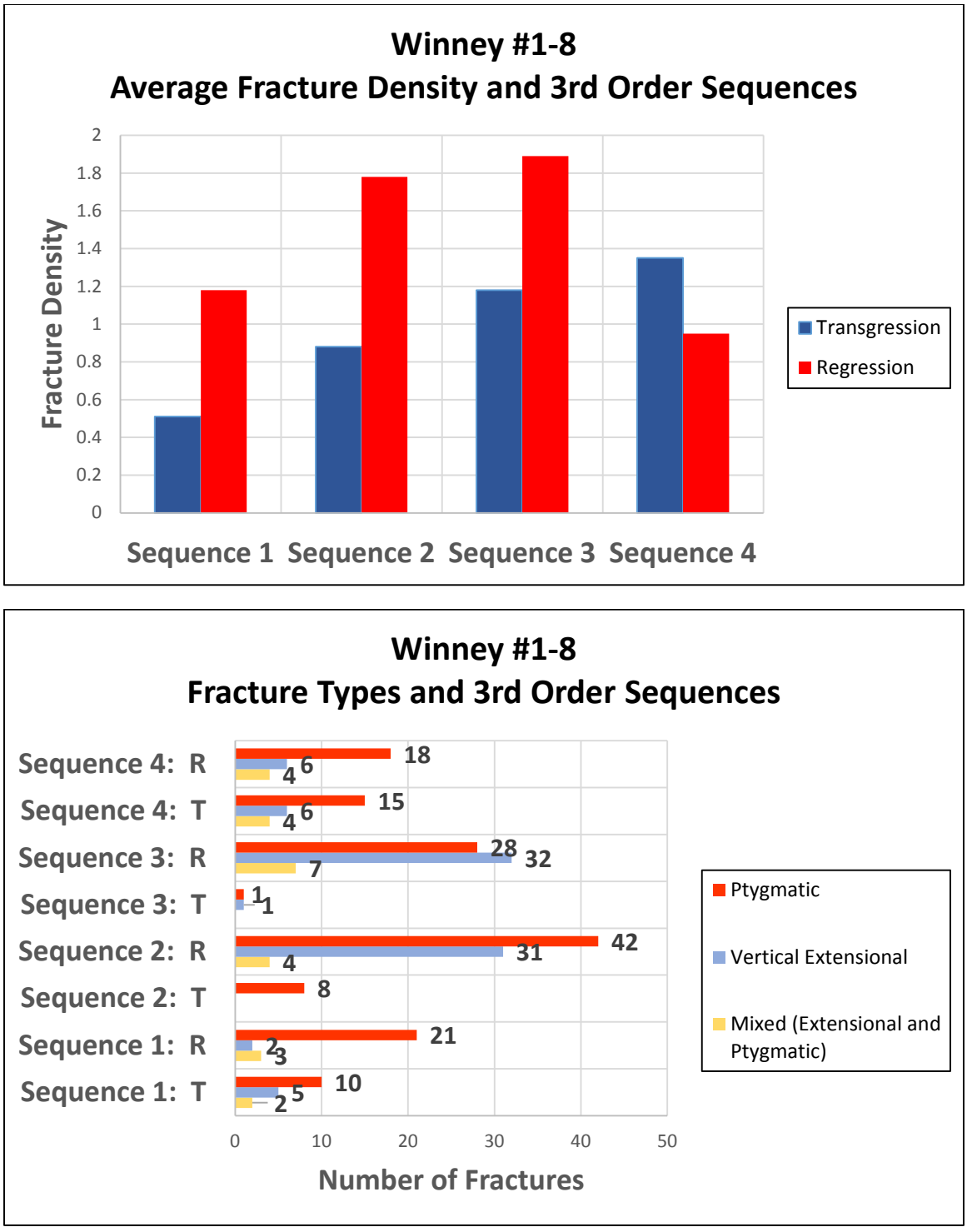

Figure 18. Fracture density and fracture types related to 3rd order sequences in the Winney core. The stratigraphic column displays the 3rd order sequences, petrophysically-significant facies types, and fractures plotted by depth. The top graph depicts the transgressive and regressive phases of each sequence and their associated fracture densities. Sequences 1, 2, and 3 have lower fracture densities in the transgressive phases and higher fracture densities in the regressive phases. The green

boxes on the stratigraphic column highlight these regressive phases with higher fracture densities. Sequence 4 displays an opposing trend of a higher fracture density value in the transgressive phase and a lower fracture density in the regressive phase. The bottom graph depicts the transgressive and regressive phases of each sequence with their associated fracture types. The regressive phases of each sequence have more ptygmatic and vertical extensional fractures than the associated transgressive phases and the regressive phases generally have more of a variety of fracture types present than the transgressive phases.

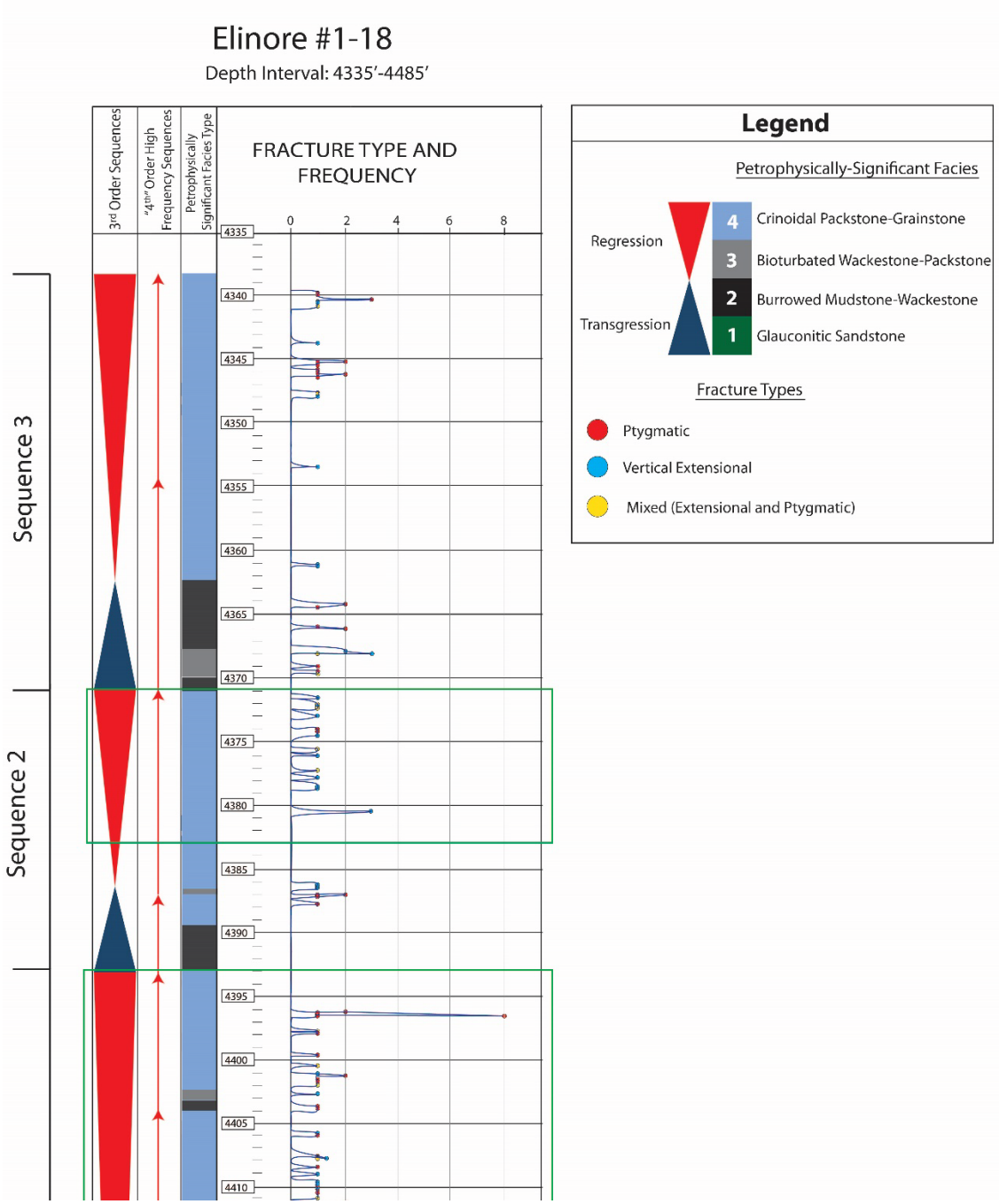
Elinore #1-18
Depth Interval: 4335'-4485'
3rd Order Sequences
"4th" Order High Frequency Sequences
Petrophysically Significant Facies Type
FRACTURE TYPE AND FREQUENCY
0
2
4
6
8
4335
4340
4345
4350
4355
4360
4365
4370
4375
4380
4385
4390
4395
4400
4405
4410
Sequence 3
Sequence 2
Legend
Petrophysically-Significant Facies
Regression
Transgression
4 Crinoidal Packstone-Grainstone
3 Bioturbated Wackestone-Packstone
2 Burrowed Mudstone-Wackestone
1 Glauconitic Sandstone
Fracture Types
Ptygmatic
Vertical Extensional
Mixed (Extensional and Ptygmatic)

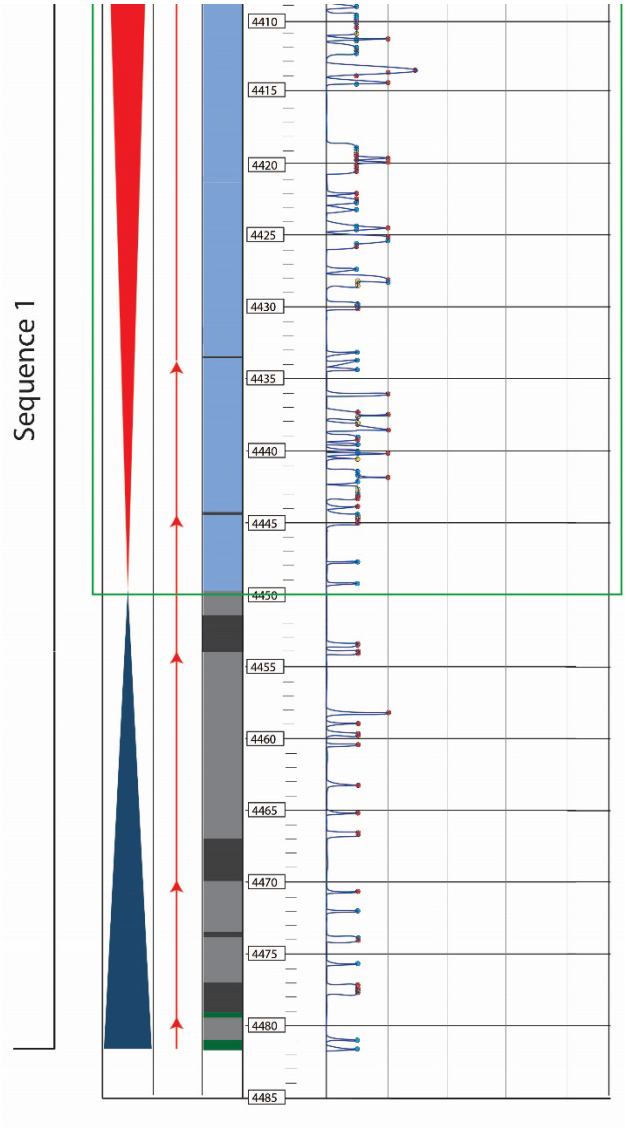
Sequence 1
4410
4415
4420
4425
4430
4435
4440
4445
4450
4455
4460
4465
4470
4475
4480
4485

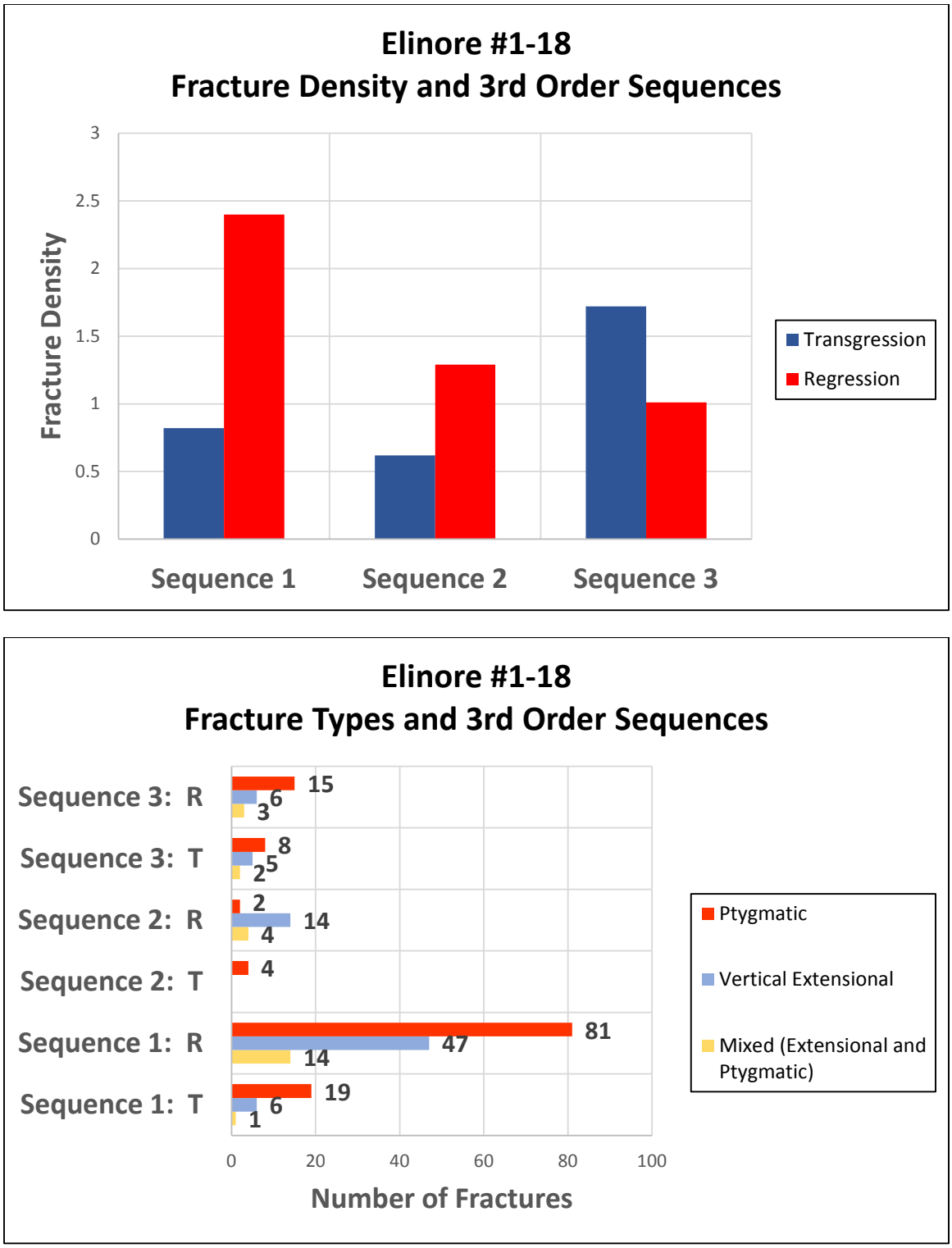

Figure 19. Fracture density and fracture types related to 3rd order sequences in the Elinore core. The stratigraphic column displays the 3rd order sequences, petrophysically-significant facies types, and fractures plotted by depth. The top graph depicts the transgressive and regressive phases of each sequence and their associated fracture

densities. Sequences 1 and 2 have lower fracture densities in the transgressive phases and higher fracture densities in the regressive phases. The green boxes on the stratigraphic column highlight these regressive phases with higher fracture densities. Sequence 3 displays an opposing trend of a higher fracture density value in the transgressive phase and a lower fracture density in the regressive phase. The bottom graph depicts the transgressive and regressive phases of each sequence with their associated fracture types. The regressive phases of each sequence generally have more ptygmatic and vertical extensional fractures than the associated transgressive phases and the regressive phases have more of a variety of fracture types present than the transgressive phases.

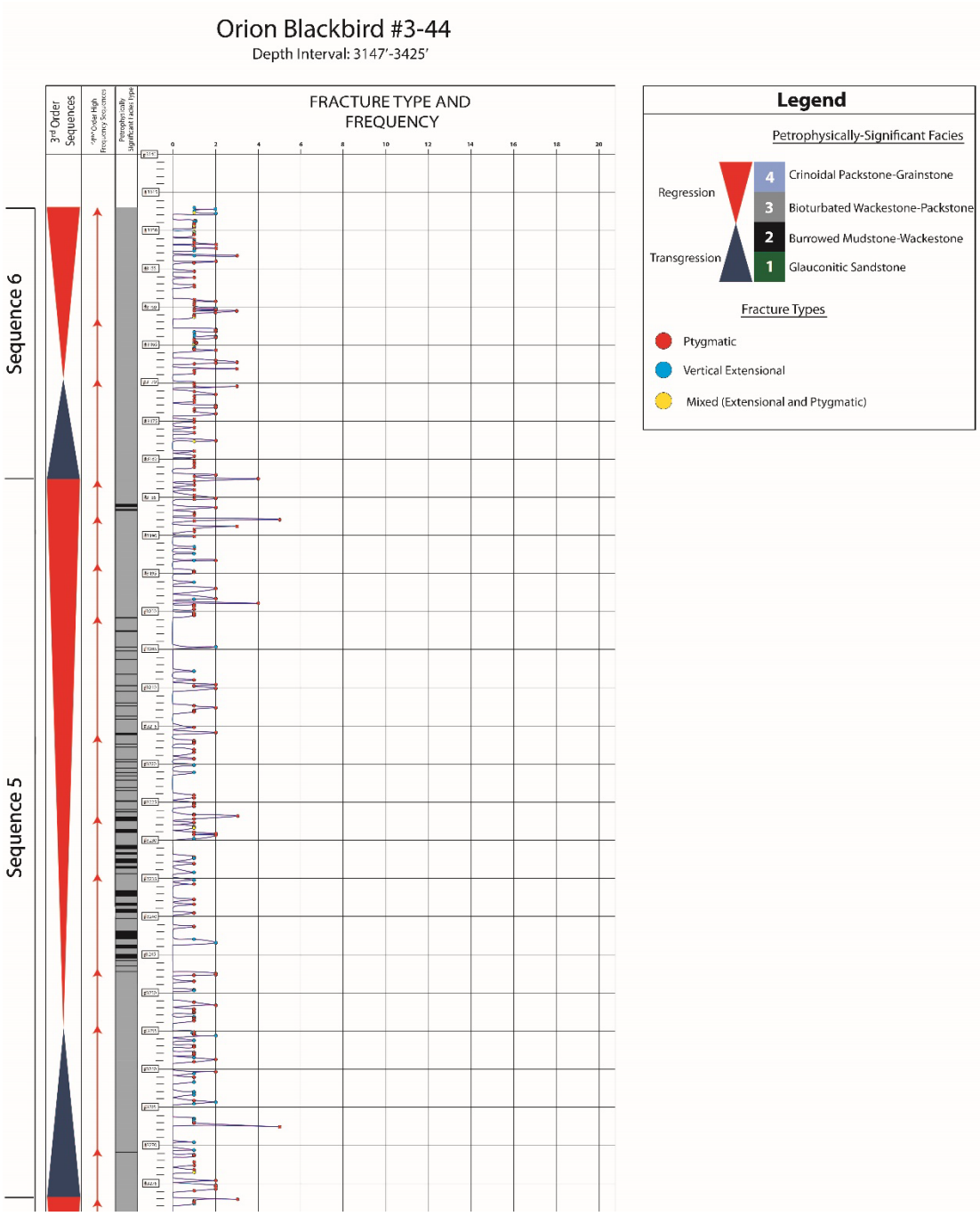
Orion Blackbird #3-44
Depth Interval: 3147'-3425'
3rd Order Sequences
FRACTURE TYPE AND FREQUENCY
Sequence 6
Sequence 5
Legend
Petrophysically-Significant Facies
Regression
Transgression
4 Crinoidal Packstone-Grainstone
3 Bioturbated Wackestone-Packstone
2 Burrowed Mudstone-Wackestone
1 Glauconitic Sandstone
Fracture Types
Ptygmatic
Vertical Extensional
Mixed (Extensional and Ptygmatic)

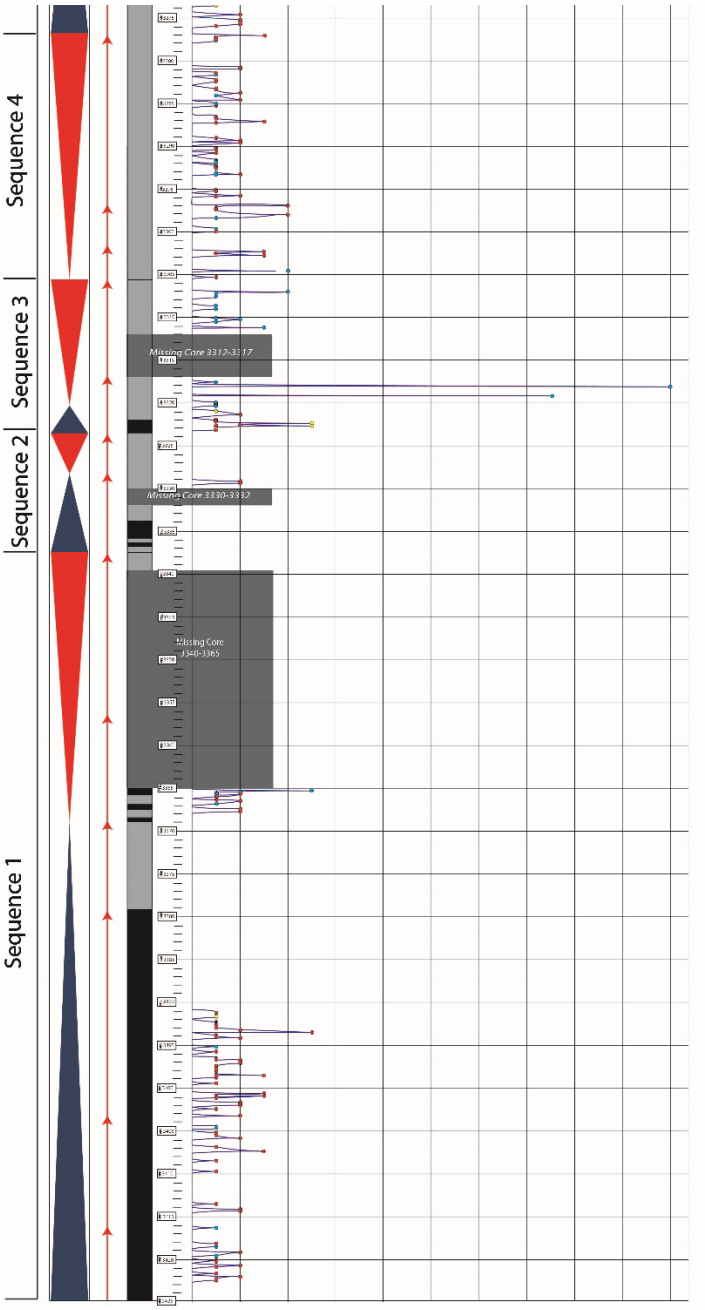
Sequence 4
Sequence 3
Sequence 2
Sequence 1
Missing Core 3312-3317
Missing Core 3330-3332
Missing Core
3340-3365

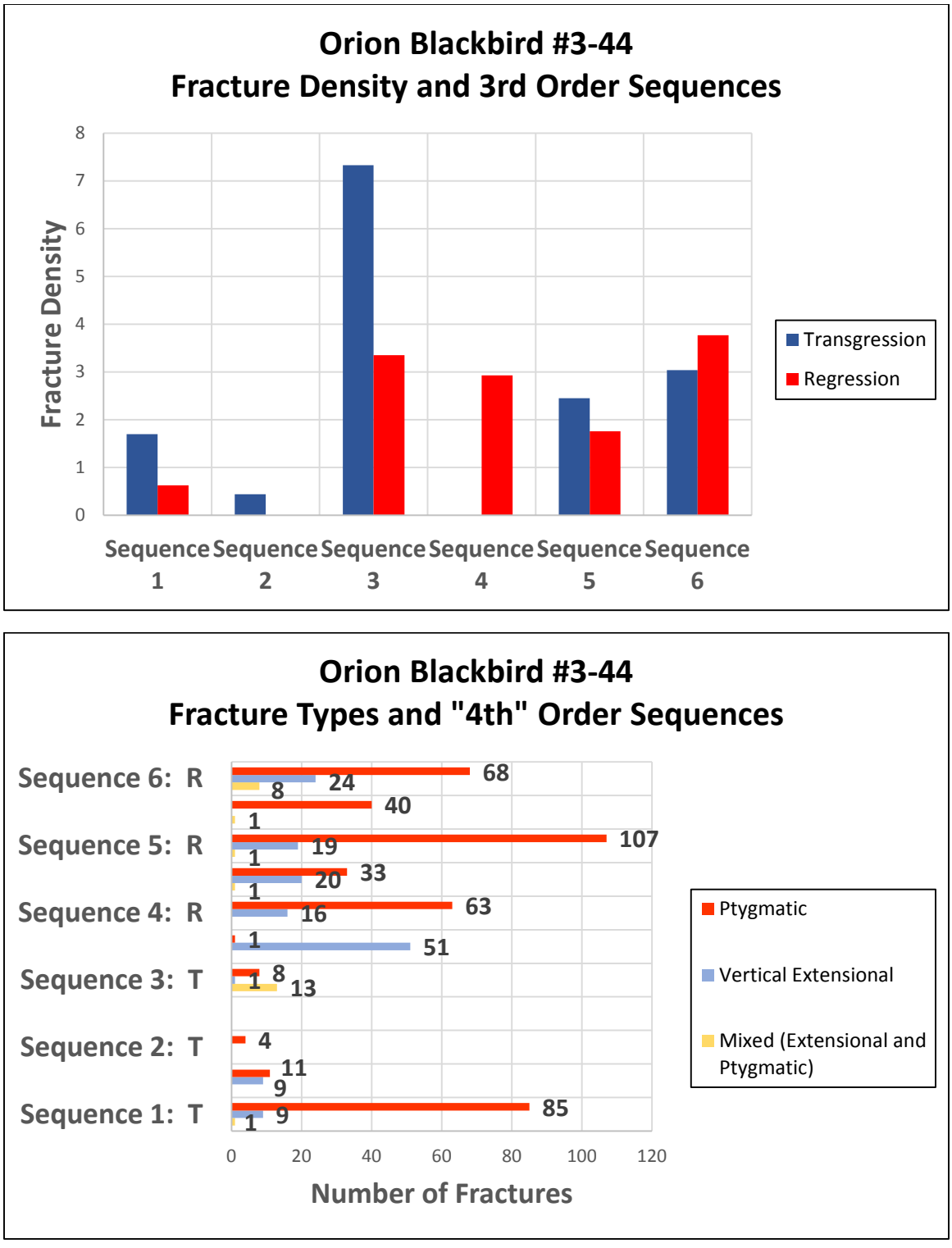

Figure 20. Fracture density and fracture types related to 3rd order sequences in the Orion Blackbird core. The stratigraphic column displays the 3rd order sequences, petrophysically-significant facies types, and fractures plotted by depth. The top graph depicts the transgressive and regressive phases of each sequence and their associated

fracture densities. Higher fracture densities are seen in the transgressive phases of sequences 1, 2, 3, and 5. The transgressive phase in sequence 4 is not present in the core. The only sequence with a higher fracture density in the regressive phase is sequence 6 at the top of the core. The bottom graph depicts the transgressive and regressive phases of each sequence with their associated fracture types. Sequences 1, 2, and 3 have higher numbers of ptygmatic fractures in the transgressive phases and sequences 5 and 6 have higher numbers of ptygmatic fractures in the regressive phases.

Fractures and X-Ray Diffraction Data

Evaluation of fractures tied to mineralogical constituents in the Winney and Elinore used three fracture density and XRD data comparisons. The first comparison included fracture density compared to total calcite and total clay percentages as individual points from each core plug sample (Figure 21) and did not result in any correlation. Figure 22 depicts the second comparison using averaged fracture densities and averaged total calcite and clay content values for each petrophysically-significant facies type. Results include: 1) increasing average fracture density values with increasing calcite percentages from Facies 1 to Facies 4, and 2) decreasing average fracture densities with increasing average clay percentages from Facies 4 to Facies 1. The third comparison (Figure 23) uses gross mineralogy curves, generated by Devon Energy, that interpolate between the measured core plug samples and depict the relative abundance of quartz, total carbonates, dolomite, and total clays for the entire Winney and Elinore cores. No obvious trends exist between whole core fracture densities and the relative mineral abundances.

A.

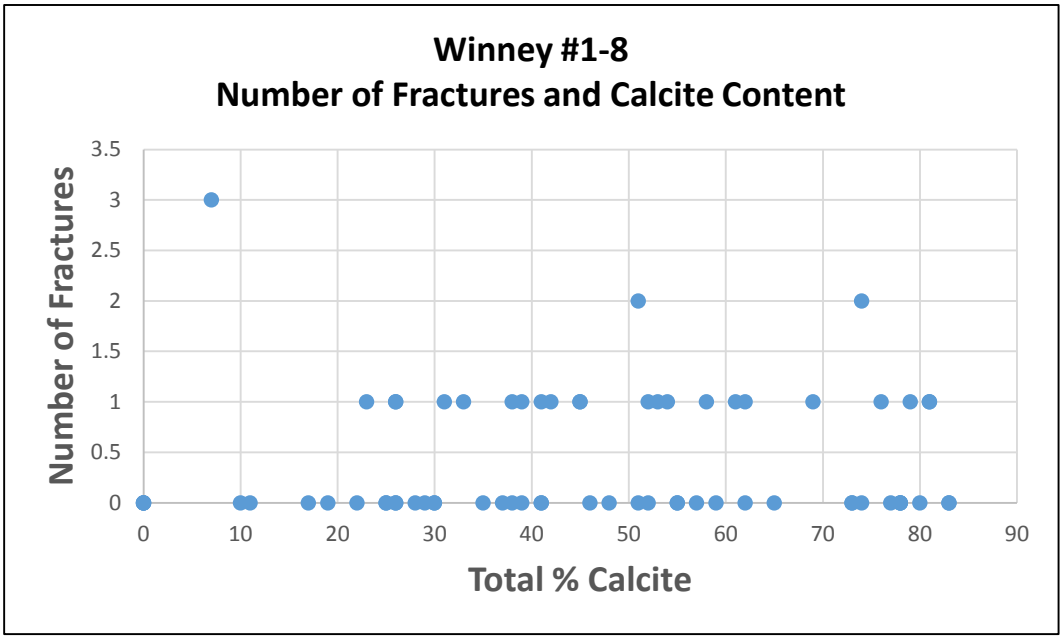

B.

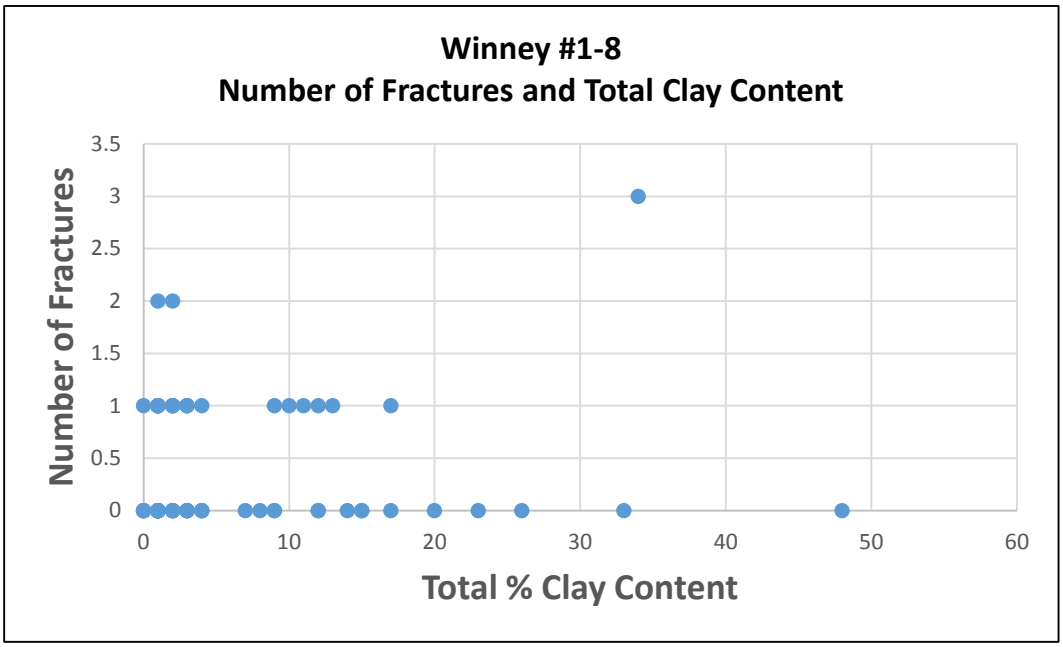

Figure 21. Fracture density related to XRD core plug data. **A)** Graph comparing fracture density and calcite percentage in the Winney core. Number of fractures is plotted on the y-axis, total calcite percentage is plotted on the x-axis. No correlation exists in the data. **B)** Graph comparing fracture density and clay content in the Winney core. Number of fractures is plotted on the y-axis, total clay content is plotted on the x-axis. No correlation exists in the data.

A.

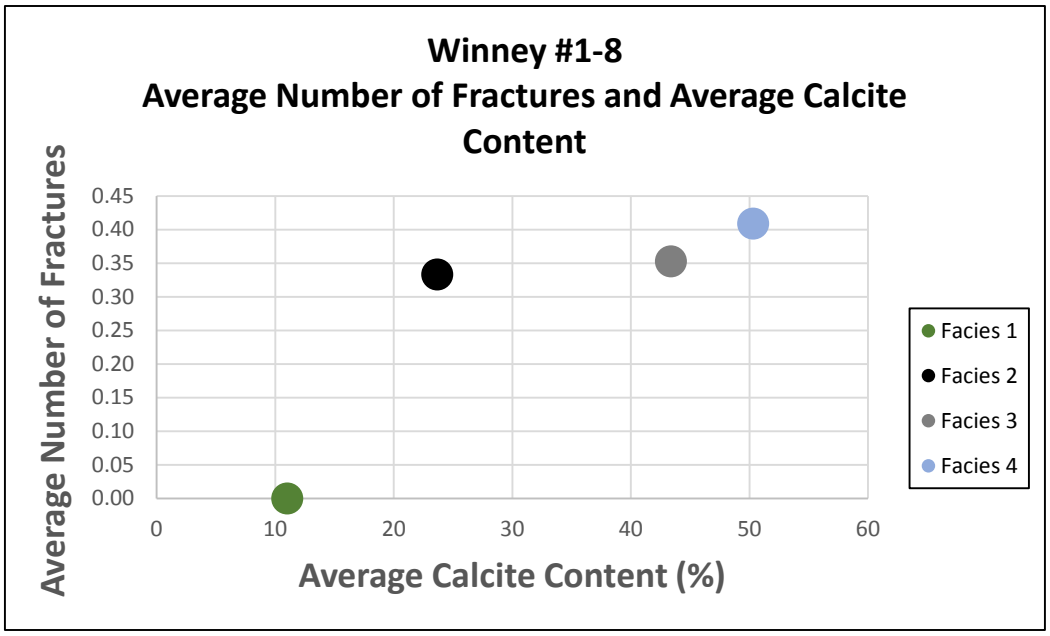

B.

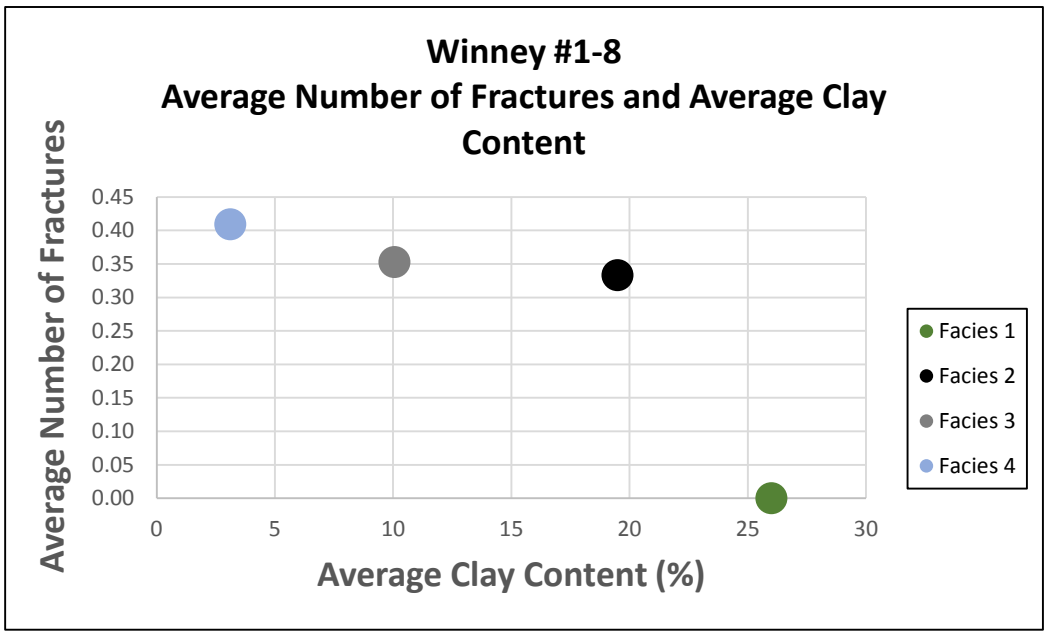

Figure 22. Average fracture density related to averaged XRD data. **A)** Graph A depicts the average fracture density (plotted on the y-axis) compared with the average calcite percentage (plotted on the x-axis) for each petrophysically-significant facies type in the Winney core. Average fracture density increases from Facies 1 to Facies 4 as the average calcite percentage increases. **B)** Graph B depicts the average fracture density (plotted on the y-axis) compared with the average clay content (plotted on the x-axis)

for each petrophysically-significant facies type in the Winney core. Average fracture density decreases from Facies 4 to Facies 1 as the average clay content increases.

Although the Orion Blackbird XRD dataset is limited, evaluation of fracture density related to total calcite content includes two comparisons. The first comparison relates fracture density and total calcite content as individual points from the core plug data, resulting in no correlation. The second comparison includes averaged fracture densities and averaged percentages of calcite in each petrophysically-significant facies type, resulting in increasing fracture densities with increasing calcite content from Facies 2 to Facies 3.

A

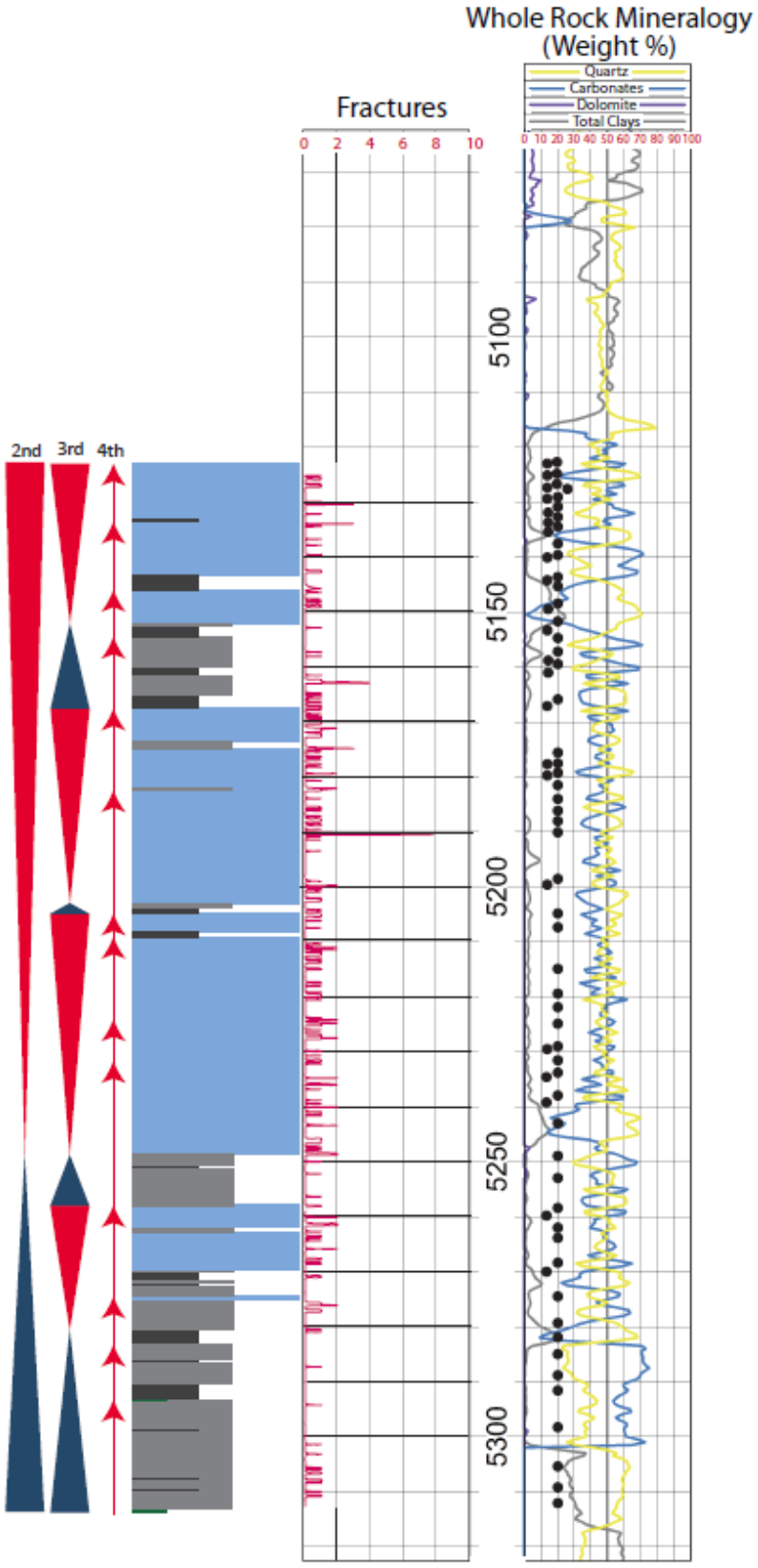
Whole Rock Mineralogy
(Weight %)
Quartz
Carbonates
Dolomite
Total Clays
0 10 20 30 40 50 60 70 80 90 100
Fractures
0 2 4 6 8 10
2nd
3rd
4th
5100
5150
5200
5250
5300

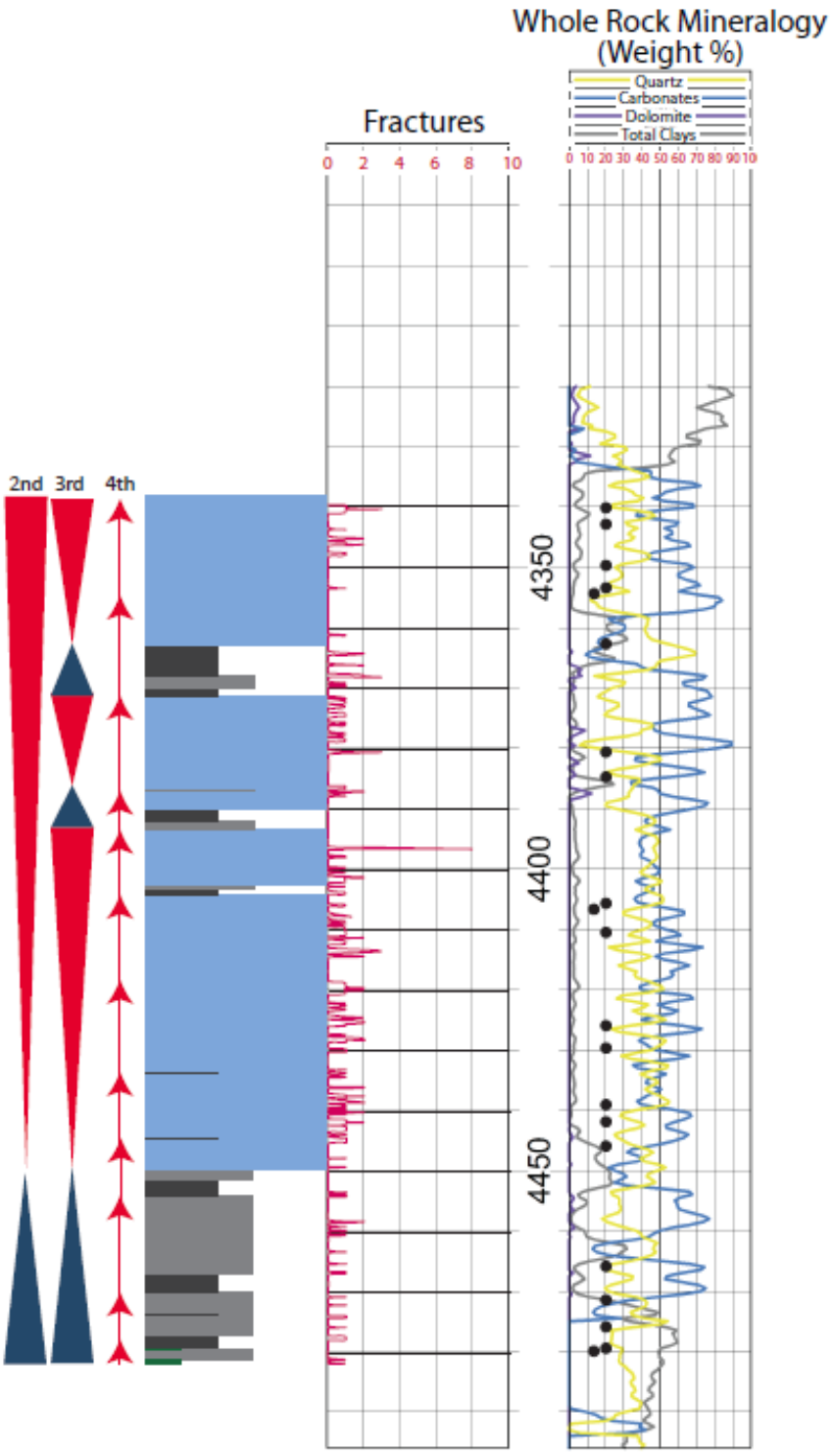

Figure 23. Comparison of whole core fracture density with the gross mineralogy curves. The black circles represent the XRD core plug sample locations. **A)** Figure A depicts the fractures plotted by depth in the Winney core next to the sequences, petrophysically-

significant facies, and the gross mineralogy curves consisting of quartz, carbonates, dolomite, and total clay content. No apparent trend exists between the fracture density and the gross mineralogy curves. **B)** Figure B depicts the fractures plotted by depth in the Elinore core next to the sequences, petrophysically-significant facies, and the gross mineralogy curves consisting of quartz, carbonates, dolomite, and total clay content. No trend exists between the fracture density and the gross mineralogy curves.

Fractures Related to Bed Thickness

Fracture Density Related to Bed Thickness

Tables 1-3 depict the average bed thickness of each facies type compared to the average fracture density within these facies, resulting in increasing fracture density values as bed thickness increases from Facies 1 (glauconitic sandstone) to Facies 4 (crinoidal packstone-grainstone).

Fracture Height and Aperture Related to Bed Thickness

All three of the studied cores reveal a correlation between average fracture height and average fracture aperture, with higher average apertures increasing as fracture height increases. Correlating the average aperture and height data with bed thickness resulted in no apparent trend in the Winney and Elinore cores (Tables 1 and 2), however, results in the Orion Blackbird core (Table 3) include increasing height and aperture values with increasing bed thickness values from Facies 2 (burrowed mudstone-wackestone) to Facies 3 (bioturbated wackestone-packstone).

Fracture Types Related to Height, Aperture, and Bed Thickness

The ratio of ptygmatic to vertical extensional fractures in Tables 1-3 was calculated using the number of ptygmatic fractures divided by the number of vertical extensional fractures in each facies and resulted in correlation between higher fracture length and apertures with lower ratios of ptygmatic to vertical extensional fractures. Referring back to Figures 13 and 14, the number of ptygmatic and vertical extensional fractures increases from Facies 1 to Facies 4, which correlates to increasing bed thickness values (i.e. higher numbers of ptygmatic and vertical extensional fractures are present in thicker beds) depicted in Tables 1-3.

Winney					
Facies	Average Bed Thickness (ft/m)	Average Fracture Density (fractures per foot/fractures per meter)	Average Fracture Height (mm)	Average Fracture Aperture (mm)	Ratio Ptygmatic/ Vertical Extensional
1	0.55/0.17	0/0	0	0	0
2	1.0/0.30	0.61/2.0	84	0.59	0.8
3	2.7/0.82	0.88/2.9	42	0.52	24
4	9.5/2.90	1.46/3.7	61	0.65	1.85

Table 1. Comparison of various parameters including average bed thickness, fracture density, height, aperture, and the ratio of ptygmatic to vertical extensional fractures in the Winney core. Patterns include: 1) as average bed thickness increases from Facies 1 to Facies 4, average fracture density increases; 2) average aperture increases as average height increases, however, no clear correlation exists between these parameters and average bed thickness; 3) higher ratios of ptygmatic to vertical extensional fractures result in lower average fracture heights and apertures.

Elinore					
Facies	Average Bed Thickness (ft/m)	Average Fracture Density (fractures per foot/fractures per meter)	Average Fracture Height (mm)	Average Fracture Aperture (mm)	Ratio Ptygmatic/ Vertical Extensional
1	0.6/0.18	0/0	0	0.00	0
2	1.8/0.55	0.44/1.45	35	0.21	8
3	3.2/0.98	1.15/3.8	124	0.64	2.38
4	12.8/3.90	1.95/6.24	53	0.53	2.36

Table 2. Comparison of various parameters including average bed thickness, fracture density, height, aperture, and the ratio of ptygmatic to vertical extensional fractures in the Elinore core. Results include: 1) as average bed thickness increases from Facies 1 to Facies 4, average fracture density increases; 2) average aperture increases as average height increases, however, no clear correlation exists between these parameters and average bed thickness; 3) generally, higher ratios of ptygmatic to vertical extensional fractures result in lower average fracture heights and apertures.

Orion Blackbird					
Facies	Average Bed Thickness (ft/m)	Average Fracture Density (fractures per foot/fractures per meter)	Average Fracture Height (mm)	Average Fracture Aperture (mm)	Ratio Ptygmatic/ Vertical Extensional
2	1.0/0.3	2.13/7.0	20	0.43	4.9
3	2.8/0.85	2.56/8.4	29	0.46	2.34

Table 3. Comparison of various parameters including average bed thickness, fracture density, height, aperture, and the ratio of ptygmatic to vertical extensional fractures in the Orion Blackbird core. Results include: 1) as average bed thickness increases from Facies 2 to Facies 3, average fracture density increases; 2) average aperture increases as average height increases and are correlated with increasing bed thickness values from Facies 2 to Facies 3; 3) higher ratios of ptygmatic to vertical extensional fractures result in lower average fracture heights and apertures.

Micro-CT Scanning of Fractured Samples

Two 1.5 inch diameter core plug samples from the Winney core were used for micro-CT scanning to evaluate fractures three dimensionally. Sample 1 (Figure 24 and 25 D) displays open or partially mineralized fractures that are discontinuous and not necessarily connected at millimeter scale. Sample 2 (Figure 22) depicts completely mineralized fractures that are connected.

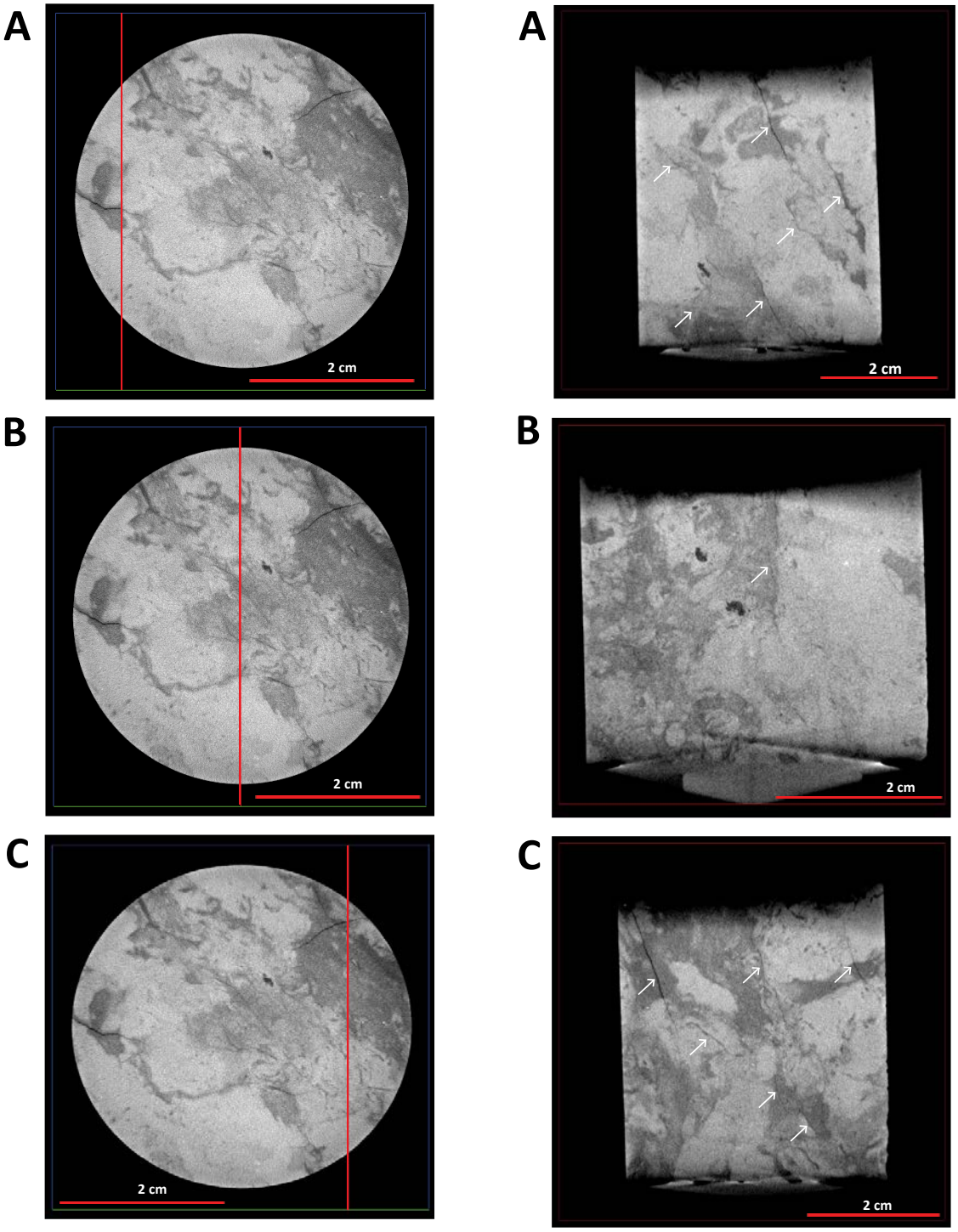

Figure 24. Two dimensional depiction of microfractures using micro-CT scanning. Images A, B, and C display a core plug sample from the Winney core at a depth of 5258.5 feet. This sample was taken from Facies 3 (bioturbated wackestone-packstone). The images are two dimensional slices of the sample. The images on the left depict the top of the core plug sample. The red lines indicate the plane in which the images to the right are displaying. The differing gray values are associated with varying minerals

present in the sample. Higher density minerals are associated with lighter gray values, whereas darker gray values are associated with minerals that have a lower density. The white arrows in the photos highlight the microfractures present. In this sample, the majority of the microfractures do not seem to be connected at the millimeter scale and do not propagate to the surface of the core plug.

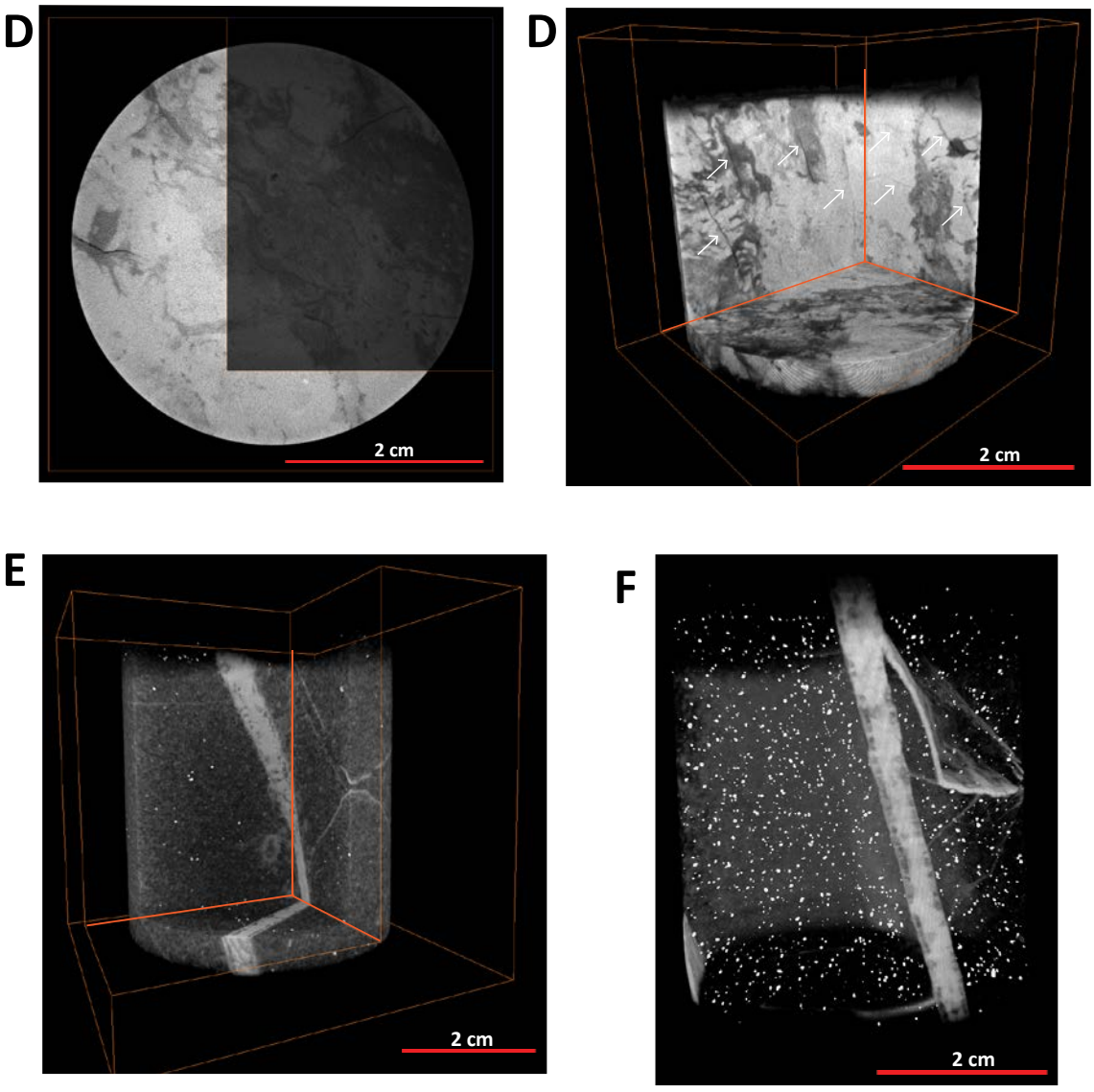

Figure 25. Three dimensional depiction of microfractures using micro-CT scanning. The images labeled "D" display a core plug sample from Facies 3 (bioturbated wackestone-packstone) in the Winney core at a depth of 5258.5 feet. Images E and F display a core plug sample from Facies 4 (crinoidal packstone-grainstone) in the Winney at a depth of 5179 feet. Images D, E, and F depict three dimensional views of the samples. The differing gray values are associated with varying minerals present in the sample. Higher

density minerals are associated with lighter gray values, whereas darker gray values are associated with minerals that have a lower density. The white arrows in the photos highlight microfractures. The right image in D depicts the discontinuous nature of the microfractures in three dimensions with no connectivity at the millimeter scale. Images E and F display mineralized fractures that are connected.

CHAPTER III

DISCUSSION

Fracture Types Related to Facies

One preliminary hypothesis of this study was that fracture types would correlate to the petrophysically-significant facies types. Previous studies determined a correlation between the mode of fracturing (fracture type) and general facies types (e.g. Gross, 1995; Lorenz et al., 1997). In this study, the general trend between fracture types and the petrophysically-significant facies exists in all three cores, where ptygmatic and vertical fractures are more abundant in Facies 4 (crinoidal packstone-grainstone) and Facies 3 (bioturbated wackestone-packstone). This correlation suggests that predictability of fracture types in the studied system can be enhanced by tying the fractures to the petrophysically-significant facies types.

The number of ptygmatic and vertical extensional fractures in the Orion Blackbird core is much higher than in the Winney and Elinore cores. The Orion is located approximately 40 miles (65 km) north of the Winney and Elinore cores where there may have been a different tectonic/stress regime that contributed to more

fractures occurring in this core. It may be that the facies types were more prone to fracturing due to some mineralogical constituent present in the Orion facies, however, the XRD dataset for the Orion is insufficient (discussed later), and therefore, it is difficult to know.

Fracture Density Related to Facies

Fracture density was also hypothesized to correlate to the petrophysically-significant facies types in the studied cores. Nelson and Serra (1993) proposed that lithology is the dominant control on the degree of fracturing in carbonate rocks that have not been deformed. Lorenz et al. (1997) states that although fracture initiation depends on the structure and tectonics to provide the stress regime, lithology is the primary control on the fracture susceptibility of a rock. Several studies have concluded that the degree of fracturing in carbonate rocks is controlled by the facies present (e.g. Stearns, 1967; Corbett et al., 1987; Gross, 1995; Gross et al. 1995; Nelson and Serra, 1993; Hanks et al., 1997; Lorenz et al., 1997; Di Naccio et al., 2005; Wennberg et al., 2006; Lézin et al., 2009; Frost and Kerans, 2010; Zahm et al., 2010). In this study, the same general trend is present in all three cores where average fracture density increases from Facies 1 (glauconitic sandstone) to Facies 4 (crinoidal packstone-grainstone), suggesting that the fracture density is tied to the petrophysically-significant facies types and that tying fractures to these petrophysically-significant facies types would enhance the subsurface predictability of fracturing in the system.

Although all of the cores exhibit trends between fracture density and facies types, the Orion Blackbird core displays much higher fracture density values in Facies 2 and Facies 3 (2.13 fractures/foot; 2.56 fractures/foot) than any of the facies in the Winney and Elinore cores. An explanation for these higher numbers could be related to the possibility that the Orion Blackbird core was deposited in a different tectonic/stress regime than the environment where the Winney and Elinore were deposited (as discussed previously). The nature of the complex internal bedding in the facies could be another possibility and this will be discussed further in this section.

Fractures Related to Sequence Stratigraphic Framework

Fractures in the studied subsurface cores were hypothesized to likely correlate to the sequence stratigraphic framework, at least at some level. Al Kharusi (2009) determined a correlation between higher fracture densities and regressive phases in the "Mississippian Limestone" in a Missouri outcrop and higher fracture densities in the transgressive phases of Mississippian rocks (likely the same age as the Winney, Elinore, and Orion Blackbird cores) of the Sheep Mountain Anticline in Wyoming. Zahm et al. (2010) determined a correlation between higher fracture densities in the transgressive phases in Aptian-Albian age carbonates in Texas.

Fractures in the Winney and Elinore resulted in the presence of higher overall fracture densities in the regressive phases of the 3rd order sequences (average thickness 47 feet/14 meters) in these cores (except for the top sequence in each) that are dominated by ptygmatic and vertical extensional fractures, suggesting that fracture

density as well as fracture types are tied to the sequence stratigraphic framework. These findings suggest that the sequence stratigraphic framework can be used to infer predictive trends of fracturing in the system. In contrast to the Winney and Elinore, the Orion Blackbird core exhibited higher fracture densities in most of the transgressive phases and the ptygmatic and vertical extensional fracture patterns in each sequence were variable, suggesting that the sequence stratigraphic framework for this core may not be a good tool to use to infer fracture density and fracture type trends.

A number of explanations might explain why some of the data did not correlate as expected to the sequence stratigraphic framework. In the Winney and Elinore cores, the top sequences may have higher fracture densities in the transgressive phases because of the unconformity present at the Mississippian/Pennsylvanian contact (i.e. it may be that the whole regressive phase of these sequences were not deposited or were removed by erosion in the cores, and/or that fracturing and jointing was enhanced due to subaerial exposure of the section). The Orion Blackbird core may have higher fracture densities in most of the transgressive phases related to undergoing a different tectonic/stress regime as discussed previously. In addition, the trends observed in sequences 1 and 3 in the Orion Blackbird core may be inconclusive due to missing core in these regressive phases. Also, sequence 1 in the Orion Blackbird core had an interval that was not analyzed for fractures due to the presence of hydrothermal breccia from approximately 3,370 to 3,390 feet.

Fractures and X-Ray Diffraction Data

It was hypothesized that fracture densities and fracture types would likely correlate to the mineralogy of the rocks. Mineralogical constituents have been known to assist or hinder the ability of a rock to fracture and affect what kind of fracturing occurs. Corbett et al. (1987) determined that mineralogy (especially smectite content) was among the three factors (two other factors include: porosity and percent axial strain) that have the greatest influence on rock strength. The relationship between fracture density and petrologic rock properties (strength and ductility) has been demonstrated in many studies (e.g. Corbett et al., 1987; Friedman et al., 1994; Rijken and Cooke 2001; Underwood et al., 2003; Lézin et al., 2009; Zahm et al., 2010). Gross (1995) and Lorenz et al. (2002) observed a correlation between the mineralogy present and fracture type.

The available XRD dataset for this study was limited by the sampling density (numbers of samples) and the location of the samples (i.e. not tied specifically to the petrophysically-significant facies or to the sequence stratigraphic framework). The Winney had the most complete XRD dataset as far as sampling density, whereas the Elinore and Orion sample points were more scattered. The core plugs for the XRD data were taken at sporadic intervals and an insufficient number of samples were taken from each of the facies types to adequately tie to facies. The nature of the sampling creates unreliability in the trends observed due to insufficient data and a potential sampling bias. In the studied cores, no trend between fracture density and mineralogy is

exhibited in the high resolution comparisons, however, trends are present in the averaged data comparisons, but these trends are questionable due to the given limitations of the dataset. Given a more constrained and comprehensive dataset, tying fracture density to XRD data would likely be a useful tool in subsurface fracture prediction in the system.

Fractures Related to Bed Thickness

Fracture Density Related to Bed Thickness

Fracture density was hypothesized to possibly correlate to bed thickness. Although fracture density is not always correlated to bed thickness (e.g. Hanks et al., 1997; Lorenz et al., 1997; Wennberg et al, 2006; Di Naccio, 2005), several studies have determined a correlation between increasing bed thickness and decreasing fracture densities (e.g. Ladeira and Price, 1981; Nelson and Serra, 1993; Harstad et al., 1996; Underwood et al., 2003). In this study, however, increasing fracture density is correlated to increased bed thickness (Tables 1-3), contrary to the trends suggested in the studies referenced above.

Although the expected trend (increasing fracture density with decreasing bed thickness) is not present in the current dataset as broken out by facies, it may be present on a smaller scale. Fractures (especially ptygmatic) tend to initiate in the brittle layers and terminate at the ductile layers e.g. (Figure 8b and Figure 26) as they do in other studies (e.g. Friedman et al., 1994; Gross et al., 1995; Lorenz et al., 1997; Rijken and Cooke, 2001; Underwood et al., 2003). Facies 4 (crinoidal packstone-grainstone)

and Facies 3 (bioturbated wackestone-packstone) tend to have a more mottled texture with frequent ductile layers (mud or clay) intervening with the overall brittle nature of these facies. It may be that the complex internal ductile structures of Facies 4 and Facies 3 are creating layers (i.e. below the bed scale) that are thinner and consequently more easily fractured. Al Kharusi (2009) noted this in the "Mississippian Limestone" outcrop in Missouri where fracture densities were higher in the regressive phases of the cycles due to the internal bedforms in the grainstones that were creating thinner layers that were more easily fractured. The fracture terminations in the cores of this study are likely mineralogically-related and a better understanding of the composition through a more complete XRD dataset would likely lead to higher fracture predictability in the system.

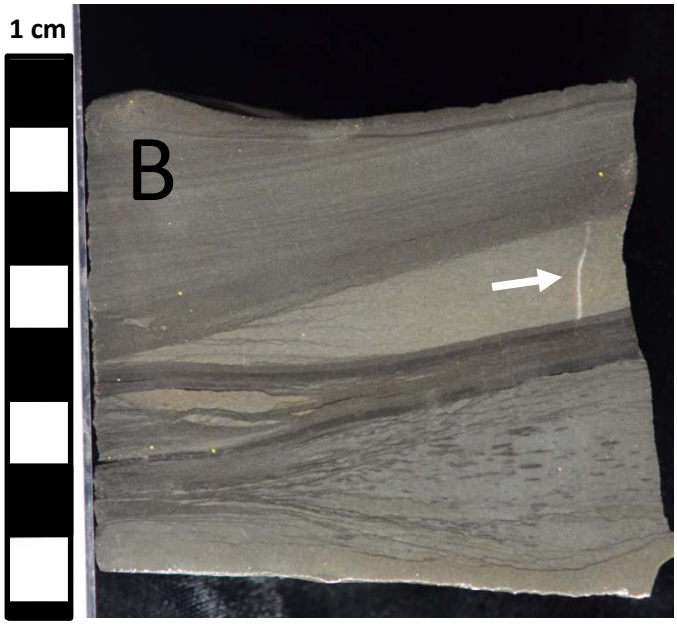

26. Core photographs of internal bedding and fractures (arrows) terminating at ductile layers. **A)** Core photograph of the Orion Blackbird core at a depth of 3274'. This photo is

an example of the complex internal bed geometries in the bioturbated wackestone-packstone facies (Facies 3) where fractures are terminating at ductile layers within an overall mottled texture. **B)** Core photograph of a fracture in the Winney core at a depth of 5224'. This photo is an example of a fracture bounded by ductile layers at the top and bottom.

Fracture Height and Aperture Related to Bed Thickness

Based on previous studies, it was hypothesized that longer/taller fractures would have wider apertures (e.g. Schultz and Fossen, 2002; Olson, 2003) and thicker beds would have taller fractures (e.g. Schultz and Fossen, 2002). In this study, generally, fracture aperture did increase with increasing fracture heights, however, no correlation exists between fracture height/aperture and bed thickness in the Winney and Elinore cores. Because Facies 4 has the highest average bed thickness (average 11.2 ft/3.4 m), it was expected to have the longest fractures as well as the widest, but as discussed previously the complex internal structures within Facies 4 are likely creating thinner beds that are more likely to fracture.

Fracture Types Related to Height, Aperture, and Bed Thickness

Comparing fracture types with overall bed thickness, average fracture heights, apertures, and bed thickness in each petrophysically-significant facies type resulted in a means to enhance the predictability of fractures in the system. The most abundant type of fracture within a zone controls the average height and width in each facies type (e.g. a higher ratio of ptygmatic to vertical extensional fractures yields lower average fracture heights and apertures) and the bed thickness and character of each facies (including

internal geometry) appears to control the abundance of fracture types (specifically ptygmatic and vertical extensional). This comparison highlights the overall goal of this study: understanding the relationship between various parameters (e.g. types of fractures and how they relate to facies/nature of the bedding, mineralogical components, bed thickness, and fracture parameters such as height and aperture) yields enhanced predictability of fractures in the subsurface.

Fracture Porosity and Permeability Implications

General assumptions can be made about fracture porosity in the subsurface cores. All of the ptygmatic fractures identified are heavily mineralized, however, Cooper and Lorenz (2012) estimate that the average remnant porosity in the ptygmatic fractures is about 1%, so the fractures could still contribute minimal porosity to the system. As Cooper and Lorenz (2012) also pointed out, the vertical extensional fractures likely add the most porosity to the system due to most of these fractures being partially mineralized.

According to Zahm et al. (2010), the tallest or longest fractures are the most important fractures from a permeability standpoint. This conclusion was made using three observations from other studies: 1) fracture height is dependent on bed thickness: thicker beds tend to have taller fractures than thinner beds (e.g. Schultz and Fossen, 2002); 2) longer/taller fractures tend to have wider apertures (e.g. Schultz and Fossen, 2002; Olson, 2003) and 3) longer/taller fractures tend to be more connected (e.g. Odling, 1997). Based on these observations, vertical extensional fractures would likely

be the main contributors to permeability because these are generally the tallest and widest fractures and may be more connected.

Micro-CT Scanning of Fractured Samples

Micro-CT scanning proved to be a useful tool for evaluating the three dimensional distribution of fractures in that: 1) it displays the discontinuous nature of some of the fractures (i.e. not all of the fractures seen three dimensionally are visible at the surface of the core plug); 2) it allows for enhanced fracture detection (40 micron resolution) over optical methods used to evaluate the cores (i.e. hand specimen and binocular microscope); and 3) it displays the lack of three dimensional interconnectedness of some of the fractures at the millimeter scale. It is likely that many fractures are unaccounted for in the data collected for this study due to the location within the core and/or the size of the fracture. Micro-CT scanning of the fractured samples highlights the need for the evaluation of microfractures that cannot be detected through evaluating hand samples in core.

Future Work

Structural Setting

The Winney, Elinore, and Orion Blackbird cores are located just east of the Nemaha Ridge (Figure 4), thus it is likely that the Nemaha Uplift played a role in the origin of fractures observed in the subsurface cores. According to Gay (1999 and 2003), the Nemaha system is structurally complex with three different phases of associated

tectonic movement: 1) high angle to reverse faulting occurring during the compressive phase; 2) strike-slip movement during later phases of compression and 3) normal faulting occurring after the compressive phase. Figure 27 indicates the three subsurface core locations and their proximity to reverse faults associated with the Nemaha Uplift. Image log reports from the subsurface cores reveal natural fracture orientations in various directions. Because of the various fracture orientations, it is difficult to determine exactly which structural phases of the Nemaha Uplift contributed to fracturing without more data. Future work on the structural setting with more detailed fracture orientation data as well as seismic data is needed to evaluate the origin of fracturing in the subsurface cores.

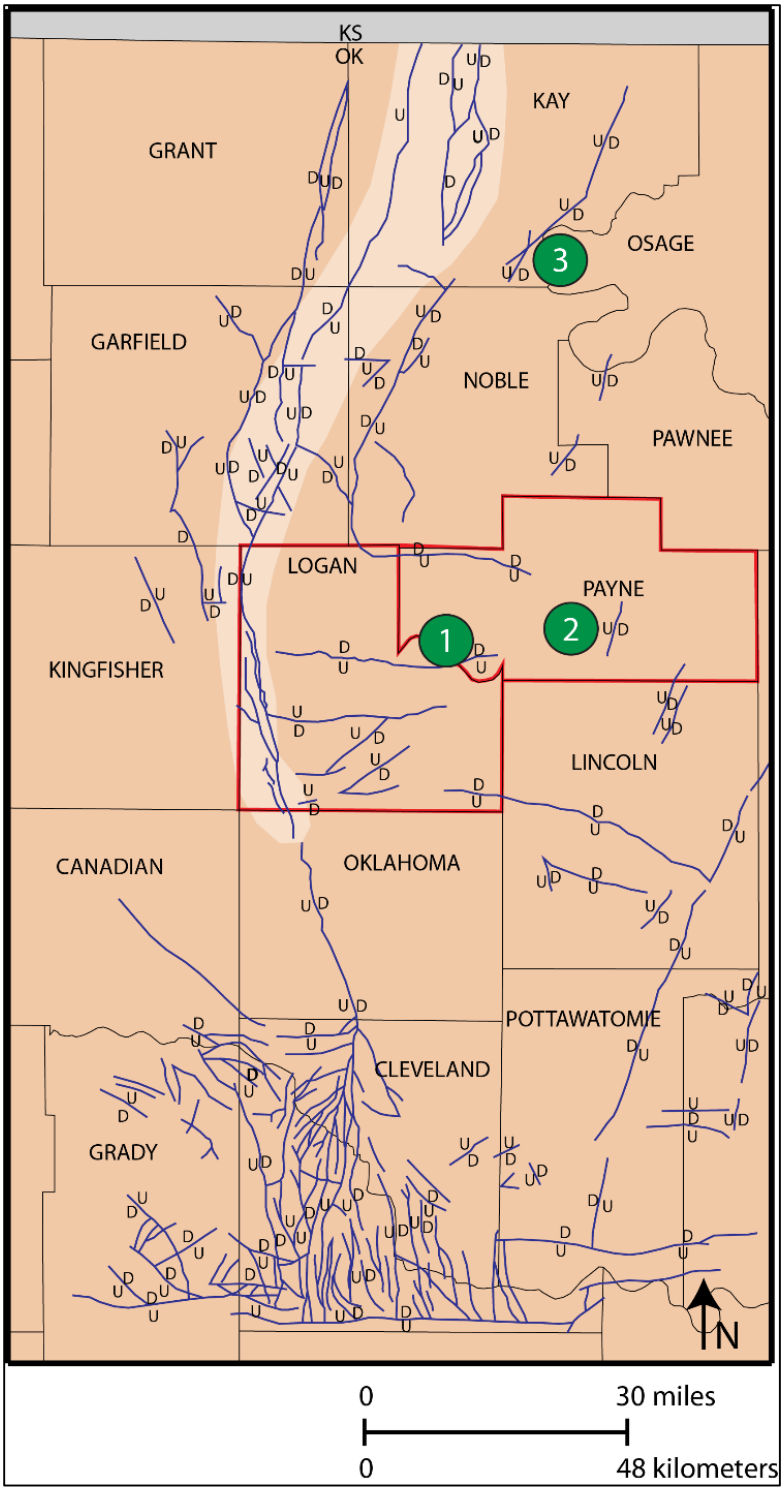

Figure 27. Map of subsurface core locations and their proximity to reverse faults associated with the Nemaha Uplift. The Winney core (1) is located on the downthrown side of an E-W trending reverse fault, the Elinore core (2) is located on the upthrown side of a NE-SW trending reverse fault, and the Orion Blackbird core (3) is located on the downthrown side of a NE-SW trending reverse fault. This map details the structural

complexity of the Nemaha Uplift system and highlights the need for understanding the structural components in the region to further evaluate the origin of fractures observed in the subsurface cores. Modified from Gay (2003).

Ptygmatic Fractures

Ptygmatic fractures are the most abundant fracture type observed in the subsurface cores, yet they are poorly understood. Cooper and Lorenz (2012) identify ptygmatic fractures as being early extensional fractures that formed and were subsequently folded and distorted with compaction. Ptygmatic fractures seem to have formed when the rock was brittle enough to fracture, but still soft enough to deform, however the timing of the mineralization observed in these fractures is debatable. Three different explanations on the timing of mineralization include: 1) extensional fracturing occurred, subsequent compaction folded the fracture, and the fracture was mineralized after compaction (Figure 28); 2) extensional fracturing occurred with subsequent mineralization, compaction occurred (folding the fracture) after mineralization, and the cement was dissolved and then the fracture was re-filled again (two different events); 3) extensional fracturing occurred with subsequent mineralization, compaction occurred after mineralization, and hydrothermal fluid dissolved the fracture fill and reprecipitated the mineralization during the same event.

To better understand the relative timing of ptygmatic fracture mineralization, it is useful to determine origin of the fracture filling cements. Timing of the ptygmatic fracture mineralization has been evaluated briefly through fluid inclusions, carbon and

oxygen isotope data, thin section analysis, and cathodoluminescence microscopy. Fluid inclusion data from Mohammadi (2016) reveal temperatures of crystallization (homogenization temperatures) ranging from 80 - 118°C, suggesting that some fluids may have been relatively hot. The isotope data from this study and Mohammadi (2016) depict carbon and oxygen isotope ranges falling between the shallow and deep burial fluid ranges. Thin section analysis of the ptygmatic fractures reveals twinning in the calcite cement filling (Figure 29) and this calcite twinning can be an indicator of the temperature of deformation (e.g. Burkhard, 1993; Ferrill et al., 2004). The temperature of deformation refers to the maximum temperature at which the material was exposed to during deformation (it is not the same as the crystallization temperature). The twins observed in the thin sections suggest type I or type II twinning (Figure 29), which corresponds to a deformation temperature of 200°C or less (type I) or 150 to 300°C (type II). Cathodoluminescence microscopy of the cement filling in the ptygmatic fractures (Figure 30) does not reveal any cement zonation, suggesting that the cement originated from a single fluid event. Further evaluation of these components in future work is vital for understanding the origin and timing of the ptygmatic fractures.

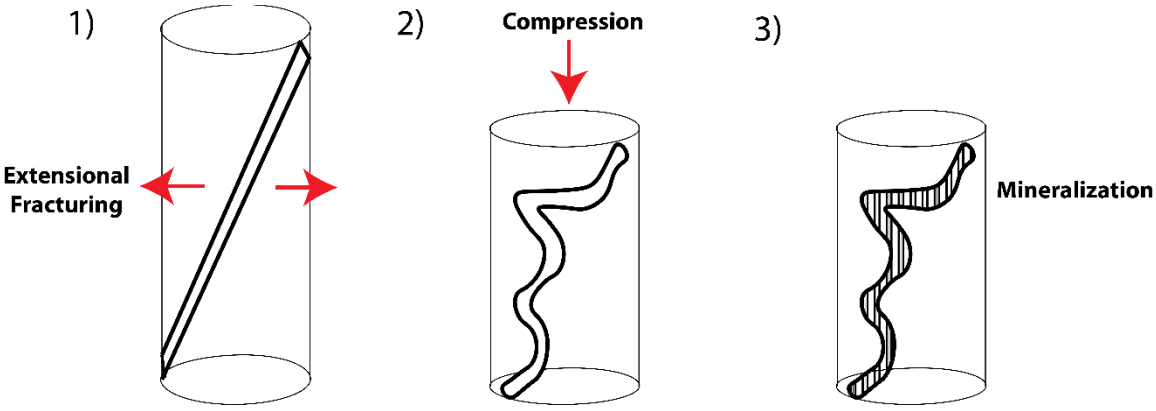

Figure 28. Diagram depicting one possible progression of events associated with the formation of ptygmatic fractures. Ptygmatic fractures are thought to have originated as early extensional fractures (1). Subsequent compaction/compression (2) led to folding and distortion of the fracture plane (indicating that ptygmatic fractures formed relatively early when the rock was brittle enough to fracture, but soft enough to deform). Mineralization of the fracture (3) occurred last.

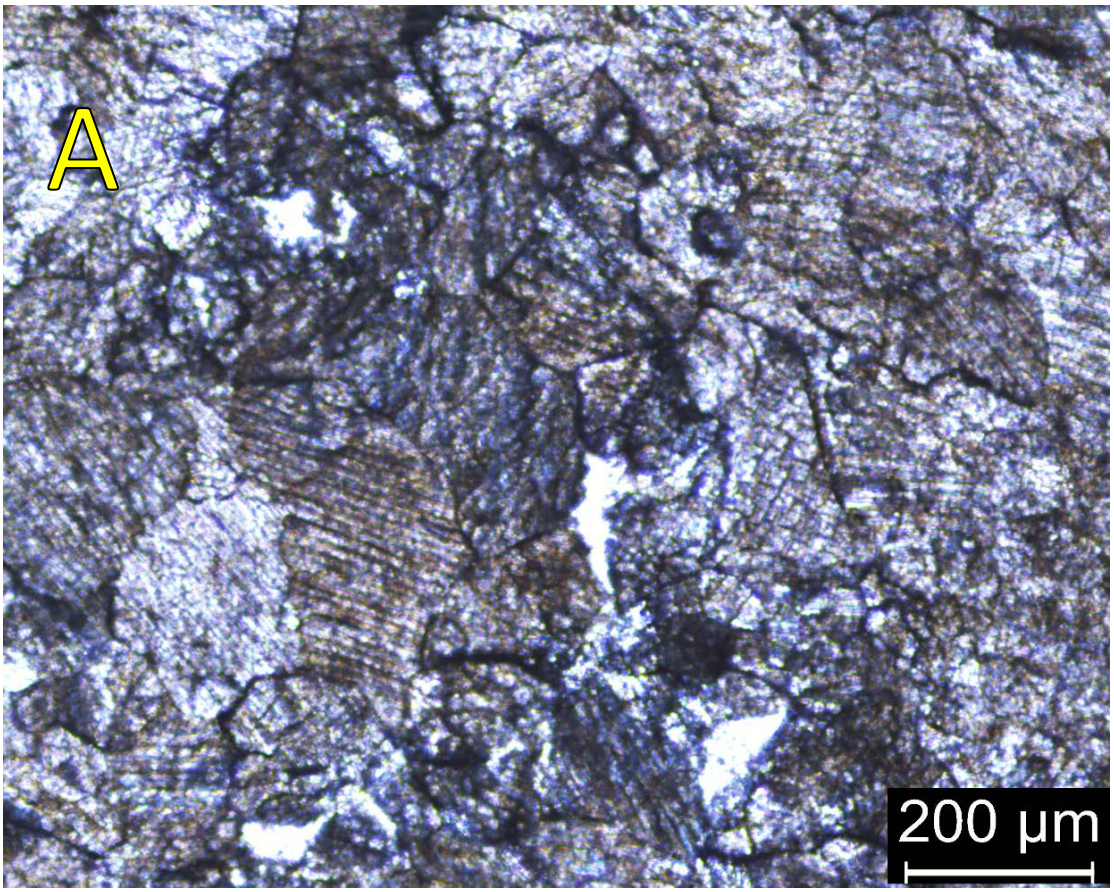

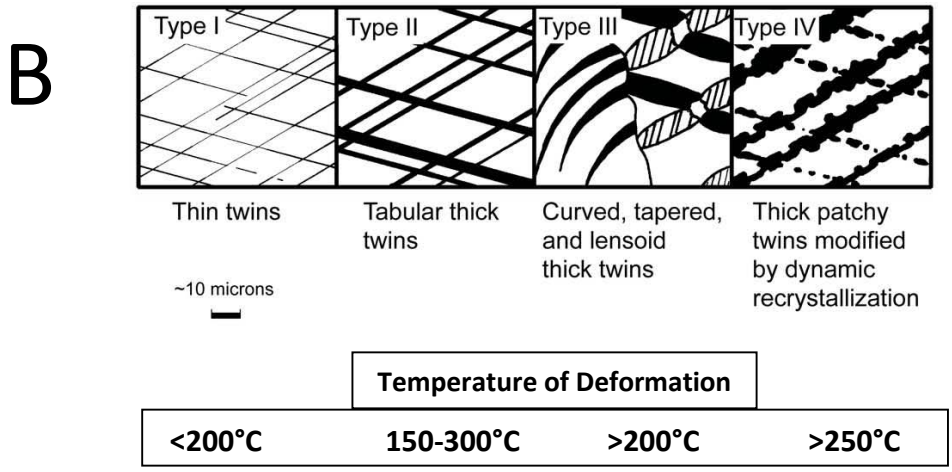

Figure 29. Calcite twinning and deformation temperature. **A)** Thin section photomicrograph of calcite cement in a ptygmatic fracture from the Orion Blackbird core at a depth of 3407.1'. The calcite grains display twinning that is characterized as type I or type II twinning (seen in B). **B)** Diagram representing the different types of twinning and the suggested temperature of deformation. The calcite twins in the ptygmatic fracture thin section photomicrograph represent type I or type II twinning,

which indicates a deformation temperature of <200°C or 150-300°C. The temperature of deformation suggests the maximum temperature the calcite was exposed to during deformation and is not necessarily the same as the crystallization temperature. Modified from Burkhard (1993) and Ferrill et al. (2004).

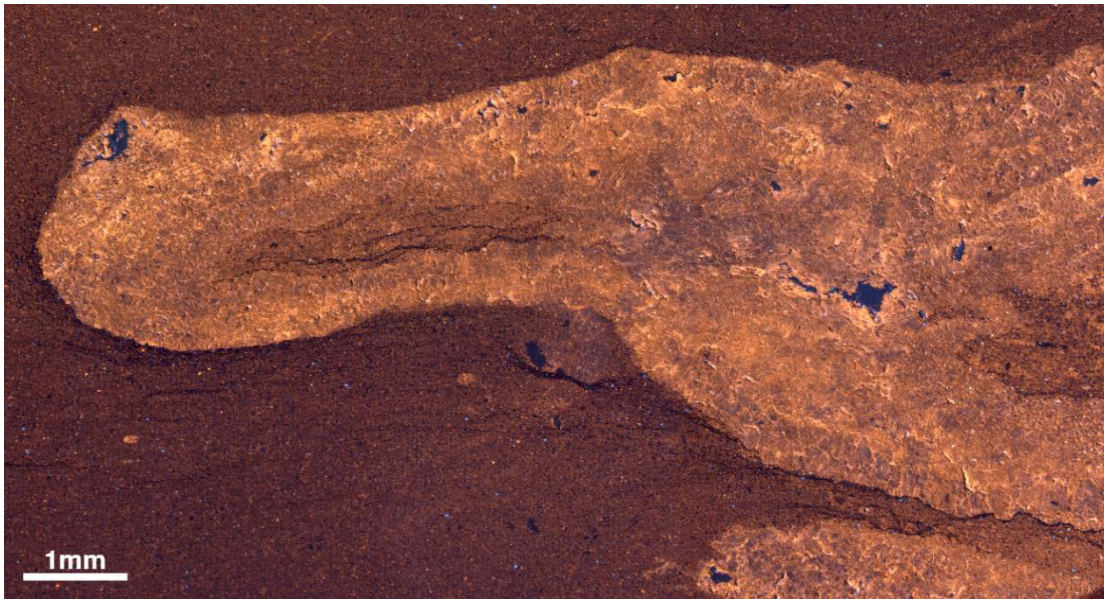

Figure 30. Cathodoluminescence thin section photomicrograph of ptygmatic fracture calcite cement. The image displays a ptygmatic fracture in the Orion Blackbird core at a depth of 3406.7'. No obvious zonation in the cement was revealed through cathodoluminescence microscopy, suggesting that the ptygmatic fracture mineralization originated from a single fluid event.

CHAPTER IV

SUMMARY AND CONCLUSIONS

This study analyzes the natural fracture network within three subsurface cores in the "Mississippian Limestone" of the Mid-Continent. The types of fractures in the system, how these fractures relate to the petrophysically-significant facies, and the relationship between fractures and the sequence stratigraphic framework are better understood and contribute to the subsurface predictability of the natural fracture system. Conclusions from this study include:

1. Four different fracture types were identified in core: vertical extensional, ptygmatic, and mixed. Ptygmatic fractures are the most abundant type present and vertical extensional fractures are the second most abundant type in all three subsurface cores.
2. Fracture types are related to the petrophysically-significant facies types. The crinoidal packstone-grainstone (Facies 4) in the Winney and Elinore cores and the bioturbated wackestone-packstone (Facies 3) in the Orion

Blackbird core have the most abundant ptygmatic and vertical extensional fractures.

3. Fracture density is related to the petrophysically-significant facies types. Facture density increases from the glauconitic sandstone (Facies 1) to the crinoidal packstone-grainstone (Facies 4) in the Winney and Elinore cores. Fracture density increases from the burrowed mudstone-wackestone (Facies 2) to the bioturbated wackestone-packstone (Facies 3) in the Orion Blackbird core.
4. Fracture type and fracture density correlate to the 3rd order sequences in the Winney and Elinore cores. Higher fracture densities as well as more abundant ptygmatic and vertical extensional fractures are present in the regressive phases. Fracture type and fracture density do not correlate well to the 3rd order sequences in the Orion Blackbird core.
5. The available XRD dataset for this study was limited by the sampling density (numbers of samples) and the location of the samples (i.e. not tied specifically to the petrophysically-significant facies or to the sequence stratigraphic framework). Selection of XRD samples tied to both could significantly aid in the prediction of fracture types and density in the subsurface.
6. Average fracture density correlates to the average bed thickness with increasing densities and thicknesses from the glauconitic sandstone (Facies 1) to the crinoidal packstone-grainstone (Facies 4). This trend

may be related to complex internal geometries that may be creating thinner layers in Facies 3 and Facies 4 that are more easily fractured.

7. Vertical extensional fractures likely contribute the most to porosity and permeability because these fractures are both longer and generally have wider apertures.
8. Micro-CT scanning of fractured samples displays the discontinuous nature of fractures, allows for enhanced fracture detection (40 micron resolution) over optical methods, and illustrates the lack of fracture interconnectedness at the millimeter scale.
9. The glauconitic sandstone facies is a key regional stratigraphic indicator that occurs in a few small intervals near the base of the Winney and Elinore cores. As previously stated, however, no fractures exist in the glauconitic sandstone facies. The glauconitic sandstone facies may act as a barrier to fractures and may stratigraphically compartmentalize fractured intervals.

REFERENCES

Al Kharusi, L. M., 2009, Correlation between high resolution sequence stratigraphy and mechanical stratigraphy for enhanced fracture characteristic prediction, unpublished Ph.D. dissertation, University of Miami, Coral Gables, Florida, 152 p.

Bann, K.L., S. C. Tye, J. A. MacEachern, C. R. Fielding, and B. G. Jones, 2008, Ichnological signatures and sedimentology of mixed wave- and storm-dominated deltaic deposits: Examples from the Early Permian, Southern Sydney Basin of southeastern Australia, in Hampson, G., Steel, R., Burgess, P., and Dalrymple, R., eds., Recent advances in models of siliciclastic shallow-marine stratigraphy: SEPM Special Publication 90, p. 293-332.

Blakey, R., 2011, Paleogeography and geologic evolution of North America, http://www2.nau.edu/rcb7/nam.html (accessed September, 2014).

Burkhard, M., 1993, Calcite twins, their geometry, appearance and significance as stress–strain markers and indicators of tectonic regime: a review: Journal of Structural Geology v. 15, no. 3-5, p. 351–368.

Childress, M., 2015, High resolution sequence stratigraphic architecture of a Mid-Continent Mississippian outcrop in southwest Missouri, unpublished M.S. thesis, Oklahoma State University, Stillwater, Oklahoma, 271 p.

Childress, M., and G. M. Grammer, 2015, High resolution sequence stratigraphic architecture of a mid-continent Mississippian outcrop in southwest Missouri, Shale Shaker, July-August, p. 206-234.

Choquette, P. W., and L. C. Pray, 1970, Geologic nomenclature and classification of porosity in sedimentary carbonates: American Association of Petroleum Geologists Bulletin, v. 54, no. 2, p. 207-250.

Cooper, S. and J. Lorenz, 2012, Natural fracture characteristics in core from the Adkisson 1-33 SWD well, Logan County, Oklahoma, Devon Energy proprietary report, 89 p.

Corbett, K., M. Friedman, and J. Spang, 1987, Fracture development and mechanical stratigraphy of Austin Chalk, Texas: American Association of Petroleum Geologists Bulletin, v. 71, p. 17–28.

Di Naccio, D., P. Boncio, S. Cirilli, F. Casaglia, E. Morettini, G. Lavecchia, and F. Bronzzetti, 2005, Role of mechanical stratigraphy on fracture development in carbonate reservoirs: Insights from outcropping shallow water carbonates in the Umbria-Marche Apennines, Italy: Journal of Volcanology and Geothermal Research, v. 148, no. 1–2, p. 98–115.

Dunham, R. J., 1962, Classification of carbonate rocks according to depositional texture, American Association of Petroleum Geologists Special Volumes, Memoir 1: Classification of Carbonate Rocks, v. 1, p. 108-121.

Ferrill, D. A., A. P. Morris, M. A. Evans, M. Burkhard, R. H. Groshong, and C. M. Onasch, 2004, Calcite twin morphology: A low-temperature deformation geothermometer: Journal of Structural Geology 26, p. 1521-1529.

Friedman, M., O. Kwon, and V. L. French, 1994. Containment of natural fractures in brittle beds of the Austin Chalk, in Nelson, P.P., Laubach, S.E., eds., Proceedings of the first North American rock mechanics symposium, Balkema, Rotterdam, p. 833–840.

Frost, E. L., and C. Kerans, 2010, Controls on syndepositional fracture patterns, Devonian reef complexes, Canning Basin, Western Australia: Journal of Structural Geology 32, p. 1231-1249.

Gay, Parker S. Jr., 1999, Strike slip, compressional thrust-fold nature of the Nemaha system in eastern Kansas and Oklahoma, Kansas Geological Society, Transaction 128 of the 1999 American Association of Petroleum Geologists Midcontinent Section Meeting (Geoscience for the 21st Century), p. 39-50.

Gay, Parker S. Jr., 2003, The Nemaha trend – A system of compressional thrust-fold, strike-slip structural features in Kansas and Oklahoma, Part 1, Shale Shaker, July-August, p. 9-49.

Goddard, E. N., P. D. Trask, R. K. De Ford, O. N. Rove, J. T. Singewald, and R. M. Overbeck, 1951, Rock color chart, Geological Society of America, Boulder, Colorado.

Grieser, B., H. Pinkerton, 2013, Horizontal Mississippian fracture completions in Oklahoma and Kansas, Transaction of the 2013 Unconventional Resources Technology Conference, Denver, CO, 11 p.

Gross, M. R., 1995, Fracture partitioning: Failure mode as a function of lithology in the Monterey Formation of coastal California: Geological Society of America Bulletin, v. 107, p. 779–792.

Gross, M. R., M. P. Fischer, T. Engelder, and R. J. Greenfield, 1995, Factors controlling joint spacing in interbedded sedimentary rocks: Integrating numerical models with field observations from the Monterey Formation, U.S.A., in M. S. Ameen, ed., Fractography: Fracture topography as a tool in fracture mechanics stress analysis: Geological Society Special Publication 92, p. 215–233.

Gutschick, R., and C. A. Sandberg, 1983, Mississippian continental margins of the conterminous United States: SEPM Special Publication 33, p. 79-96.

Hanks, C. L., J. C. Lorenz, L. Teufel, and A. P. Krumhardt, 1997, Lithology and structural controls on natural fracture distribution and behavior within the Lisburne Group, northeastern Brooks Range and North Slope subsurface, Alaska: American Association of Petroleum Geologists Bulletin, v. 81, p. 1700–1720.

Harris, S.A., 1975, Hydrocarbon accumulation in “Meramec-Osage” (Mississippian) rocks, Sooner Trend, northwest-central Oklahoma: American Association of Petroleum Geologists Bulletin, v. 59, p. 633-664.

Harstad, H., L. W. Teufel, J. C. Lorenz, and S. R. Brown, 1996, Characterization and fluid-flow simulation of naturally fractured Frontier Sandstone, Green River Basin, Wyoming: Albuquerque, New Mexico, Sandia National Laboratories, v. 96-1955, 70 p.

Kulander, B. R., S. L. Dean, and B. J. Ward, 1990, Fractured core analysis: Interpretation, logging, and use of natural and induced fractures in core: American Association of Petroleum Geologists Methods in Exploration series, No. 8, Tulsa, Oklahoma, 88 p.

Ladeira, F. L., and N. J. Price, 1981, Relationship between fracture spacing and bed thickness: Journal of Structural Geology, v. 3, no. 2, p. 179–183.

Lane, H. R., and T. L. DeKyser, 1980, Paleogeography of the Late Early Mississippian (Tournasian 3) in the central and southwestern United States, Paleozoic paleogeography of west-central United States: Rocky Mountain Paleogeography Symposium 1, p. 149-162.

LeBlanc, S. L., 2014, High resolution sequence stratigraphy and reservoir characterization of the “Mississippian Limestone” in north-central Oklahoma, unpublished M.S. thesis, Oklahoma State University, Stillwater, Oklahoma, 443 p.

Lézin, C., F. Odonne, G. J. Massonnat, and G. Escadeillas, 2009, Dependence of joint spacing on rock properties in carbonate strata: American Association of Petroleum Geologists Bulletin, v. 93, no. 2, p. 271–290.

Lockman, D. F., R. P. George, and M. J. Hayes, 1997, A systematic technique for describing and quantifying fractures in core, American Association of Petroleum Geologists, Pacific Section 2009, Bakersfield, CA, 33 p.

Lorenz, J. C., and S. J. Finley, 1990, Significance of drilling and coring induced fractures in Mesaverde core, northwestern Colorado: American Association for Petroleum Geologists Bulletin, v. 74, no. 7, p. 1017-1029.

Lorenz, J. C., W. D. Rizer, H. E. Farrell, M. D. Sonnenfeld, and C. L. Hanks, 1997, Characteristics of natural fractures in carbonate strata, in Palaz, I., and Marfurt, K. J., eds., Carbonate seismology, Society of Exploration Geophysicists Geophysical Development series, no. 6, p. 179-201.

Lorenz, J. C., J. L. Sterling, D. S. Schechter, C. L. Whigham, and J. J. Jensen, 2002, Natural fractures in the Spraberry Formation, Midland Basin, Texas: the effects of mechanical stratigraphy on fracture variability and reservoir behavior: American Association of Petroleum Geologists Bulletin, v. 86, p. 505-524.

Mohammadi, S., 2016 (in progress), Regional diagenesis of Mississippian strata of the southern Mid-Continent: northeastern Oklahoma, northwestern Arkansas,

southwestern Missouri and southeastern Kansas, Ph.D. dissertation, Oklahoma State University, Stillwater, Oklahoma.

Montgomery, J. C., M. W. Longman, W. M. Colleary, and J. P. Rogers, 1998, Mississippian "chat" reservoirs, South Kansas: Low-resistivity pay in a complex chert reservoir: American Association of Petroleum Geologists Bulletin, v. 82, no. 2, p. 187-205.

Nelson, R. A., and S. Serra, 1993, Vertical and lateral variations in fracture spacing in folded carbonate sections and its relation to locating horizontal wells: Canadian SPE/CIM/CANMET International Conference on Recent Advances in Horizontal Well Applications, Canadian Society of Petroleum Engineers, Paper HWC94-41, 10 p.

Nelson, R. A., 2001. Geological analysis of naturally fractured reservoirs, 2nd edition: Gulf Professional Publishing, 332 p.

Northcutt, R. A., and J. A. Campbell, 1996, Geologic provinces of Oklahoma, Transaction of the 1995 American Association of Petroleum Geologists Mid-Continent Section Meeting, Tulsa, Oklahoma, p. 128-134.

Odling, N., 1997, Scaling and connectivity of joint systems in sandstones from western Norway: Journal of Structural Geology 19, no. 10, p. 1257–1271.

Olson, J. E., 2003, Sublinear scaling of fracture aperture versus length: an exception or the rule?: Journal of Geophysical Research 108, no. B9, p. 2413–2414.

Price, B., 2014, High resolution sequence stratigraphic architecture and reservoir characterization of the Mississippian Burlington-Keokuk Formation, northwestern Arkansas, unpublished M.S. thesis, Oklahoma State University, Stillwater, Oklahoma, 154 p.

Read, J. F., 1995, Overview of carbonate platform sequences, cycle stratigraphy and reservoirs in greenhouse and icehouse worlds, in Read, J. F., Kerans, C., Weber, L. J., Sarg, J. F., and Wright, F. M., eds., Milankovitch sea level changes, cycles, and reservoirs on carbonate platforms in greenhouse and icehouse worlds: SEPM Short Course 35, p. 1-102.

Rijken, P., and M. L. Cooke, 2001, Role of shale thickness on vertical connectivity of fractures in the Austin Chalk, Texas: application of crack-bridging theory: Tectonophysics, v. 337 no. 1-2, p. 117–133.

Schultz, R. A., H. Fossen, 2002. Displacement–length scaling in three dimensions: the importance of aspect ratio and application to deformation bands: Journal of Structural Geology 24, p. 1389–1411.

Stearns, D. W., 1967, Certain aspects of fractures in naturally deformed rocks, in R. E. Riecker, ed., National Science Foundation advanced science seminar in rock mechanics, Bedford, Massachusetts, Air Force Cambridge Research Laboratory Special Report, p. 97-118.

Underwood, C. A., M. L. Cooke, J. A. Simo, and M. A. Muldoon, 2003, Stratigraphic controls on vertical fracture patterns in Silurian dolomite, northeastern Wisconsin: American Association of Petroleum Geologists Bulletin, v. 87, no. 1, p. 121–142.

Vanden Berg, B., 2016 (in progress), Increasing the prediction of permeability in carbonate reservoirs utilizing sonic velocity response coupled with pore system characterization: An example from a Mid-Continent unconventional reservoir (Mississippi Limestone), Ph.D. dissertation, Oklahoma State University, Stillwater, Oklahoma.

Wennberg, O. P., T. Svånå, M. Azizzadeh, A. M. M. Aqrawi, P. Brockbank, K. B. Lyslo, and S. Ogilvie, 2006, Fracture intensity vs. mechanical stratigraphy in platform top carbonates: The Aquitanian of the Asmari Formation, Khaviz anticline, Zagros, southwest Iran: Petroleum Geoscience, v. 12, no. 3, p. 235–246.

Wilhite, Brian W., S. J. Mazzullo, B. T. Morris, and D. R. Boardman, 2011, Syndepositional tectonism and its effects on Mississippian (Kinderhookian to Osagean) lithostratigraphic architecture: Part 1 – Based on exposures in the Mid-Continent USA, American Association of Petroleum Geologists Search and Discovery Article #30207, 43 p.

Witzke, B. J., R. M. McKay, B. J. Bunker, and F. J. Woodson, 1990, Stratigraphy and environments of Mississippian strata in Keokuk and Washington Counties,

southeast Iowa: Iowa Department of Natural Resources, Geological Survey Bureau Guidebook Series No. 10, 105 p.

Zahm, C. K., L. C. Zahm, and J. A. Bellian, 2010, Integrated fracture prediction using sequence stratigraphy within a carbonate fault damage zone, Texas, USA: Journal of Structural Geology 32, p. 1363-1374.

APPENDICES

APPENDIX A

FRACTURE DATA AND CORE DESCRIPTIONS

The tables below display the fracture data summaries for each core. Each illustrative core description follows, which includes a fracture column of each fracture seen in core plotted by depth and color coded by fracture type.

Winney #1-8: Fracture Summary					
	Total Number	Height		Width	
Vertical Extension	59	Sum (ft)	16.12	Sum (mm)	34.25
		Average (mm)	75.58	Average (mm)	0.54
		Minimum (mm)	8.00	Minimum (mm)	0.15
		Maximum (mm)	304.00	Maximum (mm)	2.65
Ptygmatic	145	Sum (ft)	18.47	Sum (mm)	81.50
		Average (mm)	39.92	Average (mm)	0.58
		Minimum (mm)	3.00	Minimum (mm)	0.10
		Maximum (mm)	176.00	Maximum (mm)	2.90
Mixed (Exensional and Ptygmatic)	23	Sum (ft)	7.61	Sum (mm)	13.75
		Average (mm)	116.00	Average (mm)	0.69
		Minimum (mm)	32.00	Minimum (mm)	0.20
		Maximum (mm)	295.00	Maximum (mm)	2.35

Elinore #1-18: Fracture Summary					
	Total Number	Height		Width	
Vertical Extension	64	Sum (ft)	12.79	Sum (mm)	27.95
		Average (mm)	68.40	Average (mm)	0.52
		Minimum (mm)	5.00	Minimum (mm)	0.15
		Maximum (mm)	291.00	Maximum (mm)	2.00
Ptygmatic	141	Sum (ft)	21.13	Sum (mm)	65.15
		Average (mm)	45.35	Average (mm)	0.47
		Minimum (mm)	3.00	Minimum (mm)	0.10
		Maximum (mm)	450.00	Maximum (mm)	1.55
Mixed (Exensional and Ptygmatic)	24	Sum (ft)	6.36	Sum (mm)	13.60
		Average (mm)	92.38	Average (mm)	0.65
		Minimum (mm)	15.00	Minimum (mm)	0.20
		Maximum (mm)	439.00	Maximum (mm)	2.65

Orion Blackbird #3-44: Fracture Summary					
	Total Number	Height		Width	
Vertical Extension	157	Sum (ft)	16.37	Sum (mm)	69.45
		Average (mm)	31.58	Average (mm)	0.45
		Minimum (mm)	0.00	Minimum (mm)	0.10
		Maximum (mm)	350.52	Maximum (mm)	1.55
Ptygmatic	421	Sum (ft)	33.77	Sum (mm)	186.20
		Average (mm)	24.45	Average (mm)	0.44
		Minimum (mm)	0.00	Minimum (mm)	0.10
		Maximum (mm)	307.85	Maximum (mm)	2.65
Mixed (Exensional and Ptygmatic)	24	Sum (ft)	1.24	Sum (mm)	13.90
		Average (mm)	15.70	Average (mm)	0.58
		Minimum (mm)	0.00	Minimum (mm)	0.20
		Maximum (mm)	107.00	Maximum (mm)	1.50

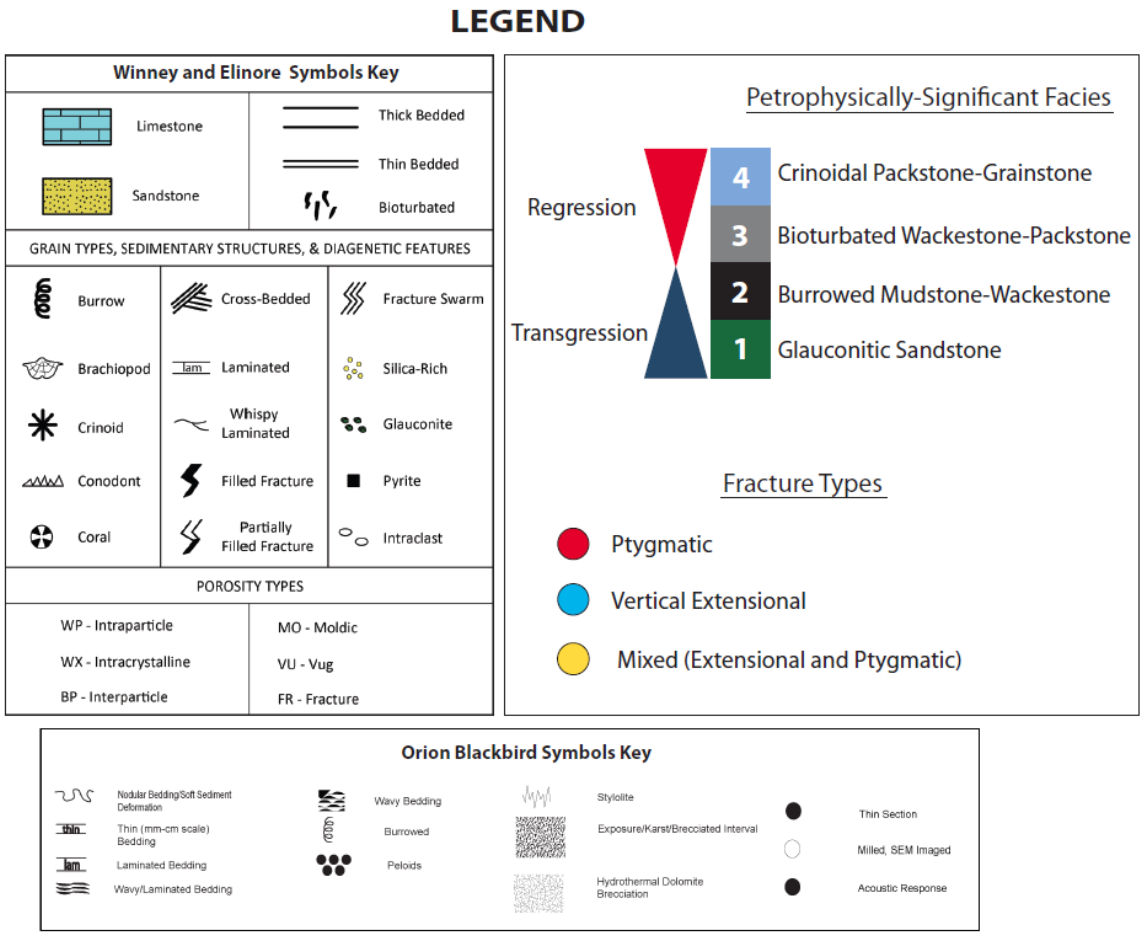

Modified from Leblanc, 2014 and Vanden Berg, 2016.

Winney #1-8, Payne County, Oklahoma

Formation: Mississippian Limestone Depth Interval: 5123'-5313'

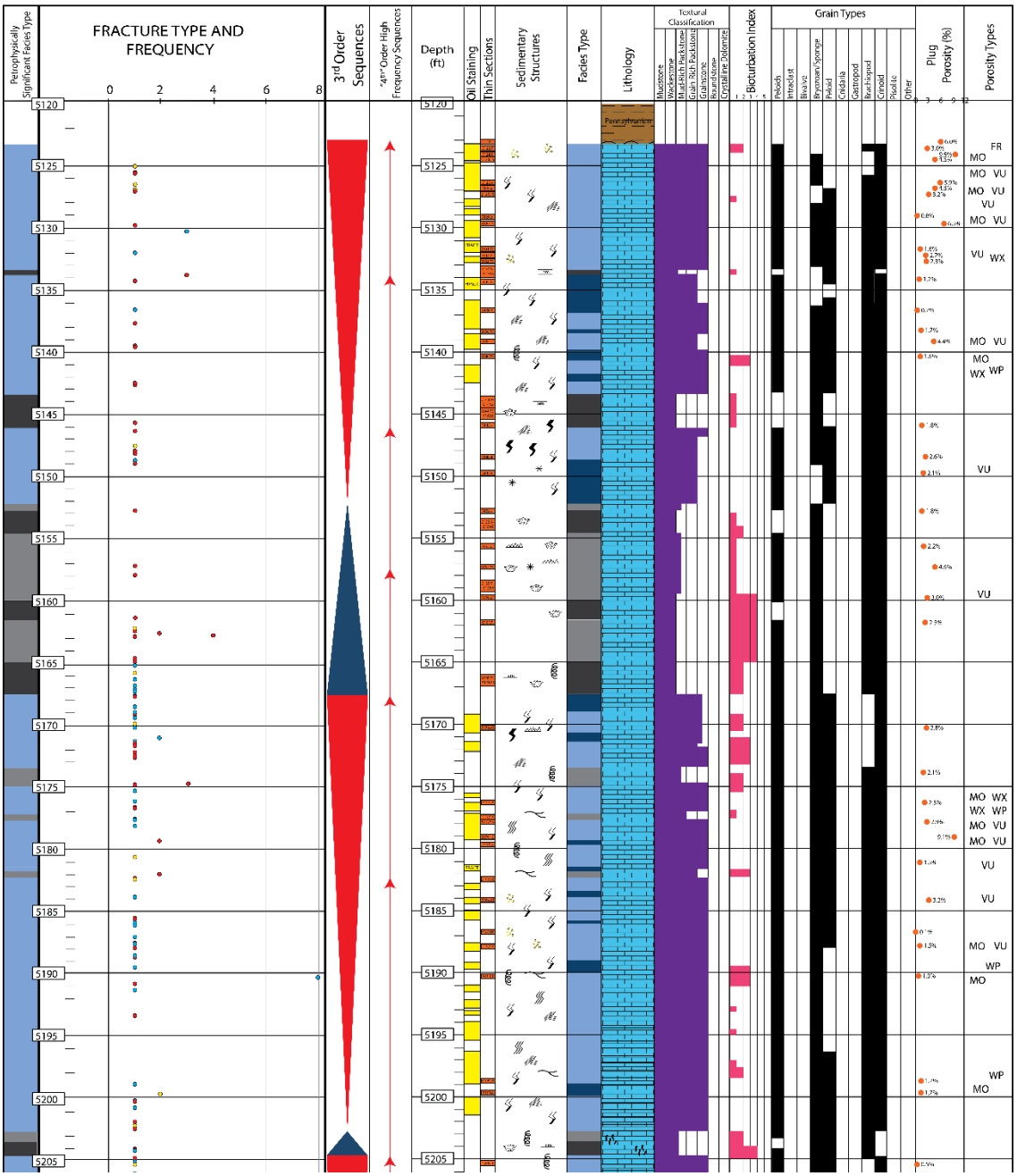

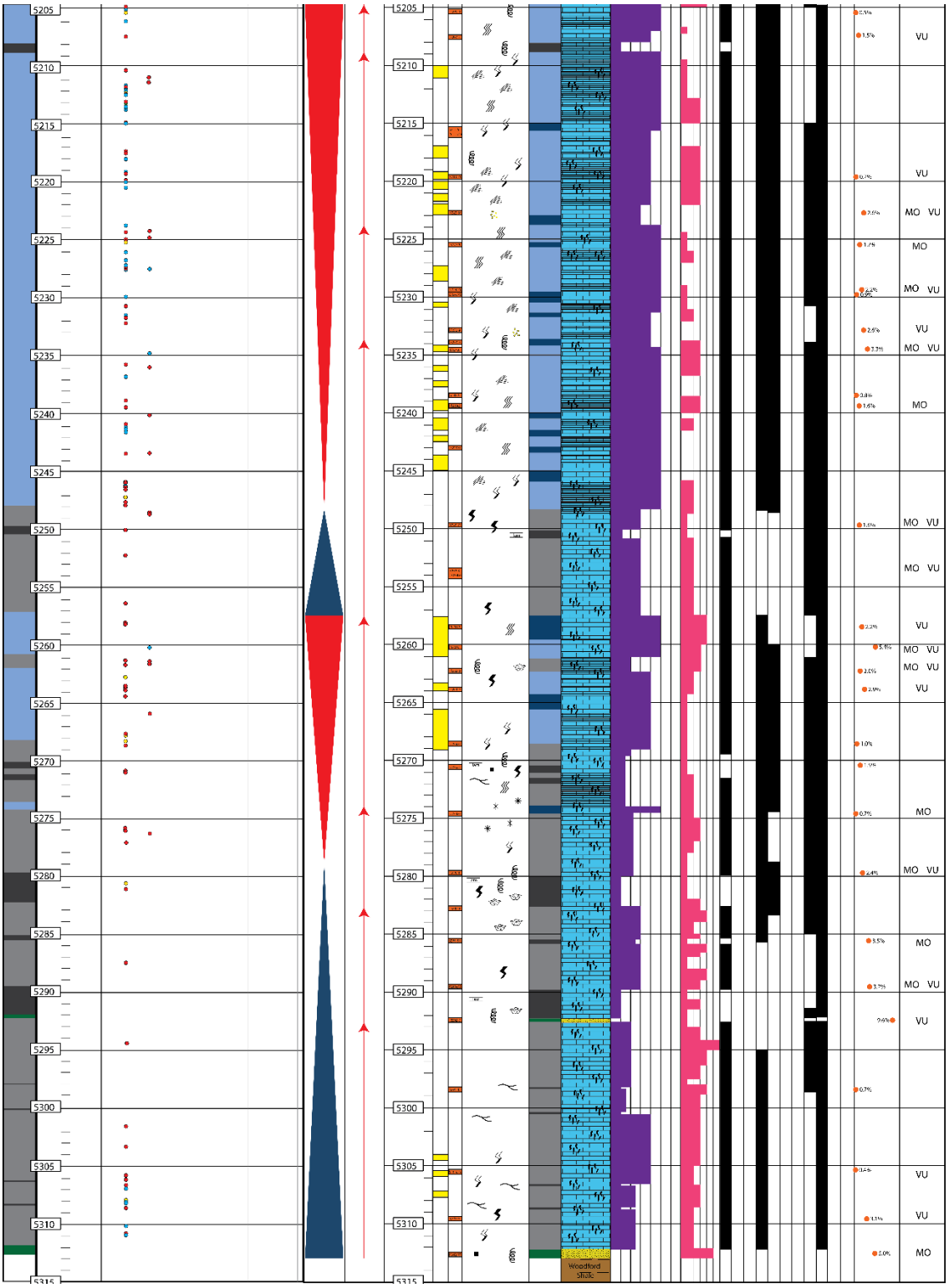

Modified from Leblanc, 2014.

Elinore #1-18, Payne County, Oklahoma

Formation: Mississippian Limestone **Depth Interval: 4335'-4485'**

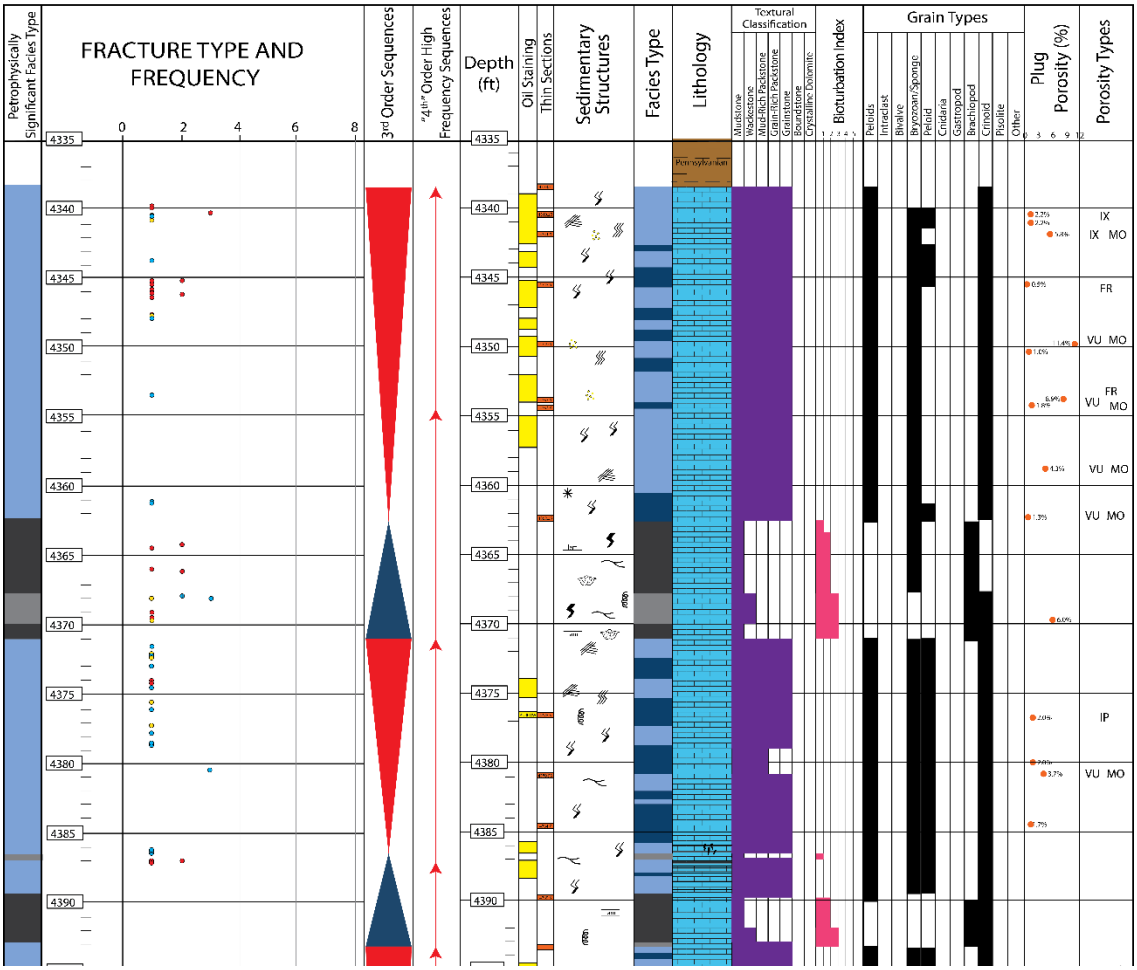

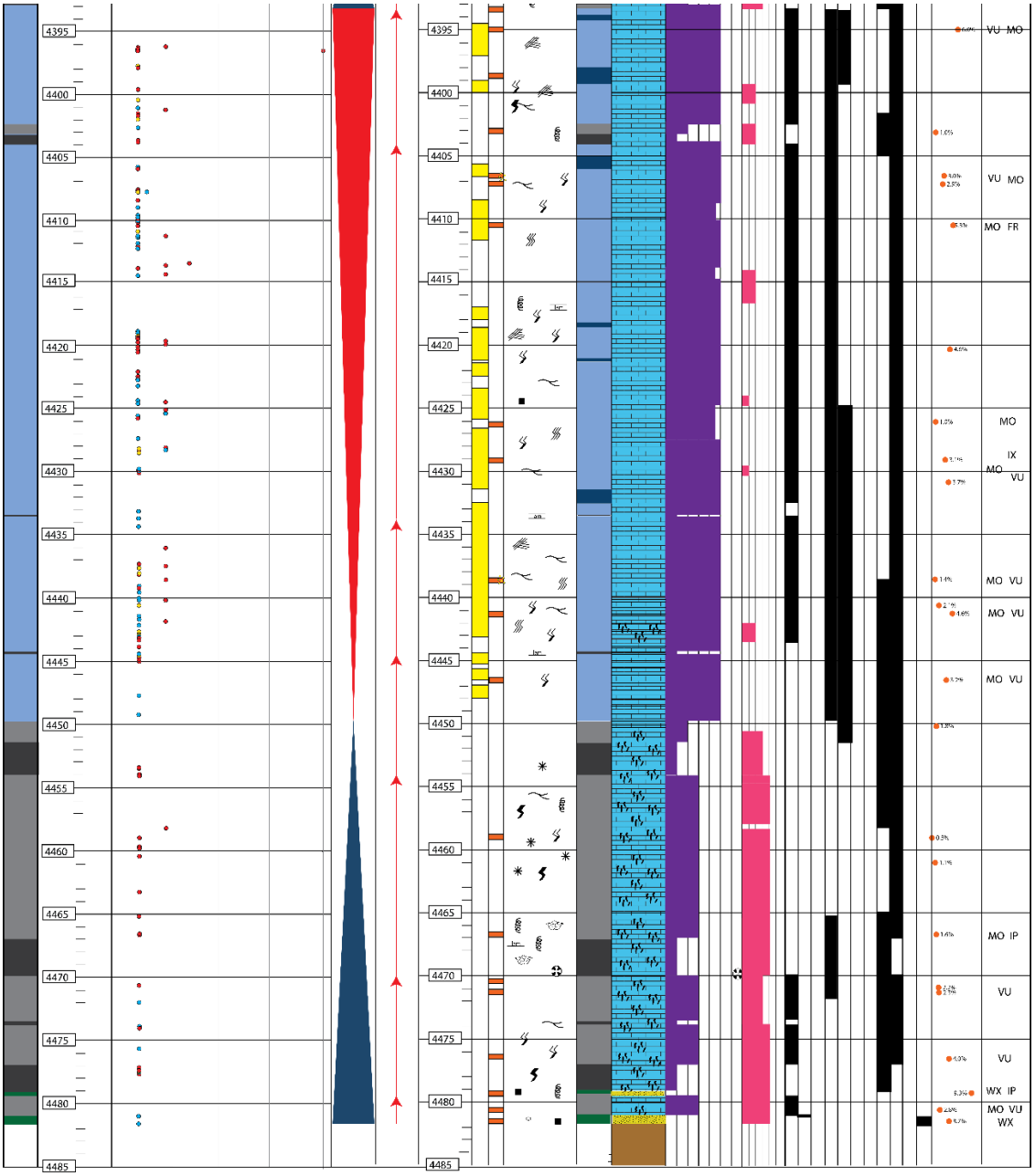

Modified from Leblanc, 2014.

Orion Blackbird #3-44, Osage County, Oklahoma

Formation: Mississippian Limestone **Depth Interval: 3147'-3425'**

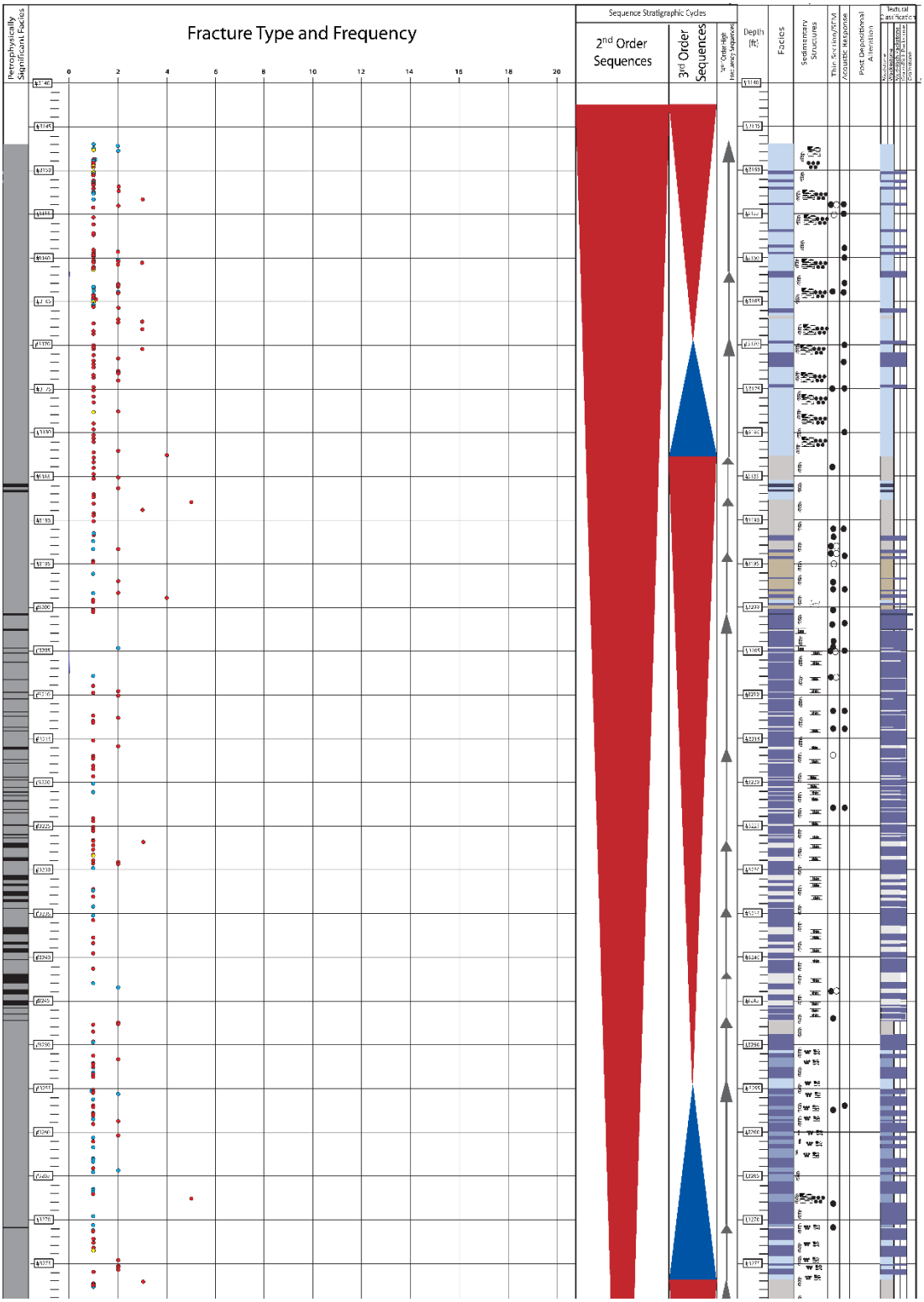

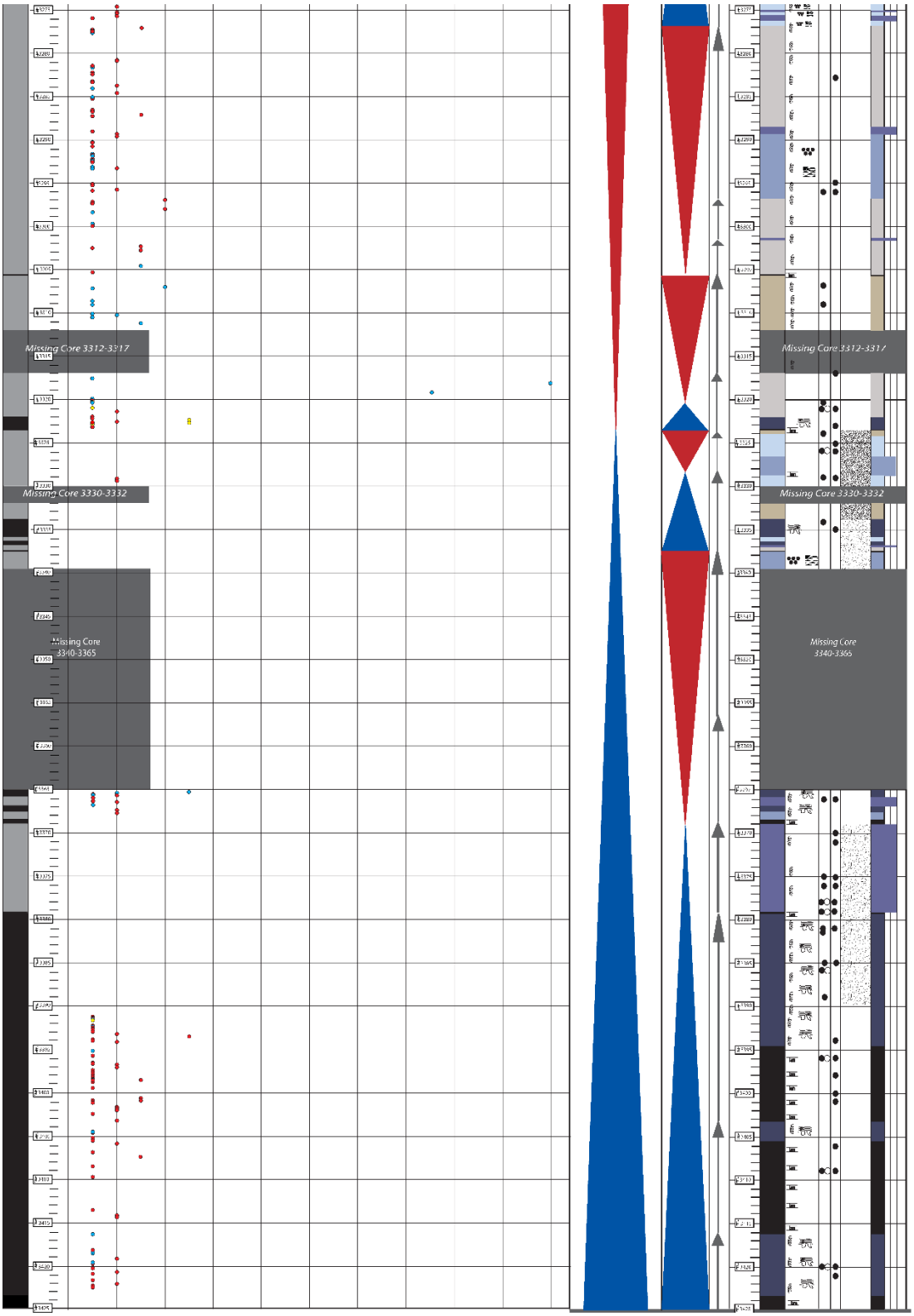

Modified from Vanden Berg, 2016.

APPENDIX B

FRACTURE DATA AND X-RAY DIFFRACTION DATA

The following graphs include fracture density and XRD data comparisons that did not result in any trends.

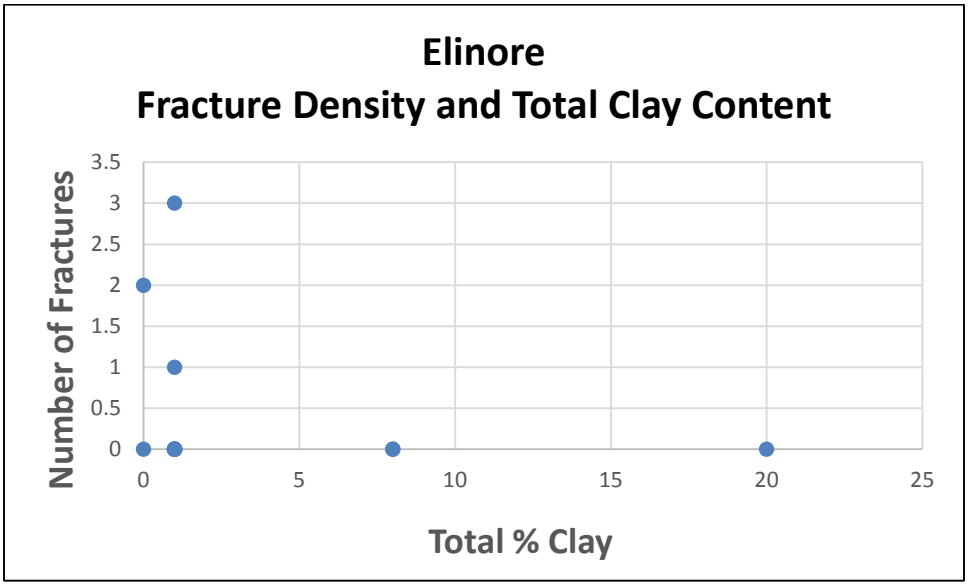

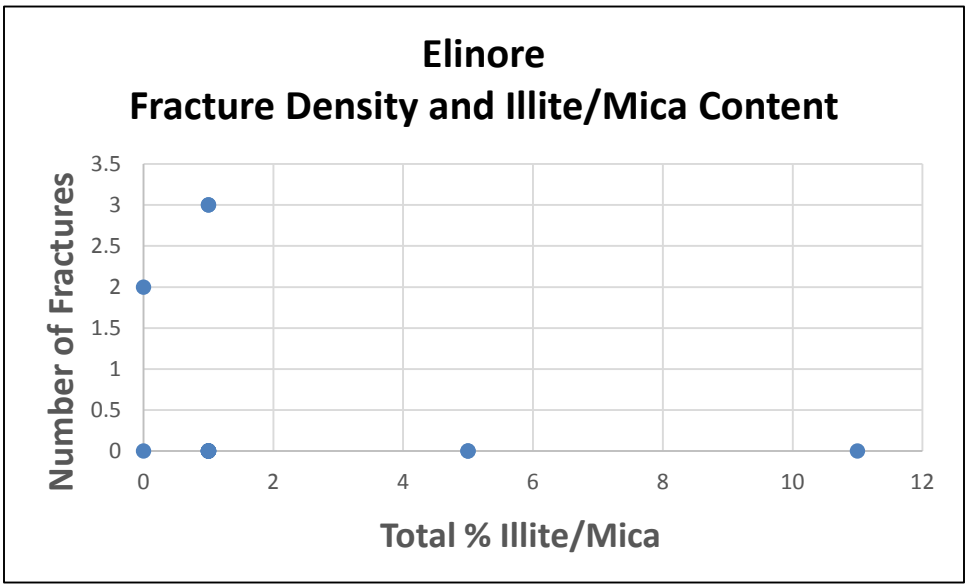

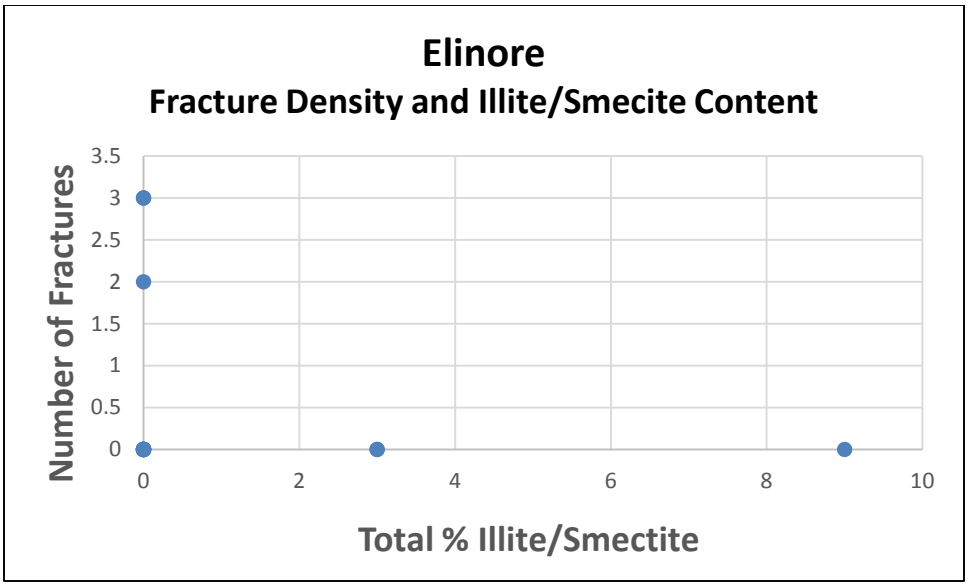
Elinore
Fracture Density and Illite/Smecite Content
Number of Fractures
3.5
3
2.5
2
1.5
1
0.5
0
0
2
4
6
8
10
Total % Illite/Smectite

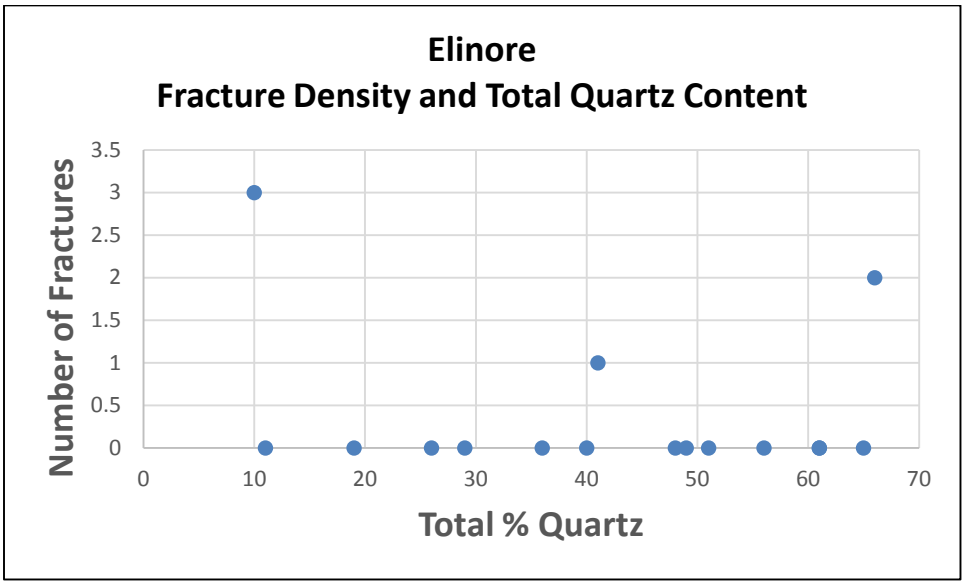
Elinore
Fracture Density and Total Quartz Content
Number of Fractures
3.5
3
2.5
2
1.5
1
0.5
0
0
10
20
30
40
50
60
70
Total % Quartz

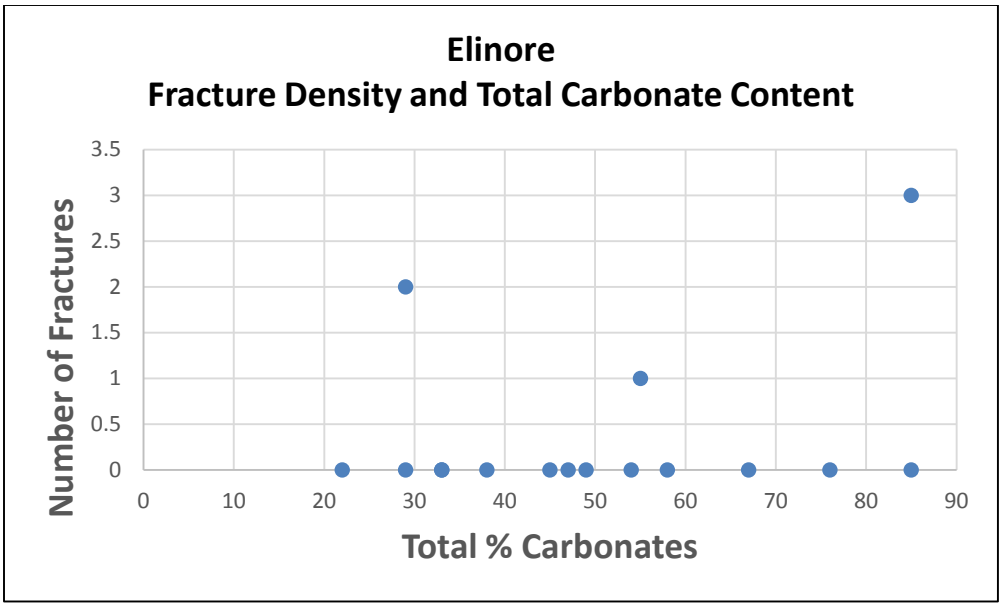
Elinore
Fracture Density and Total Carbonate Content
Number of Fractures
3.5
3
2.5
2
1.5
1
0.5
0
0
10
20
30
40
50
60
70
80
90
Total % Carbonates

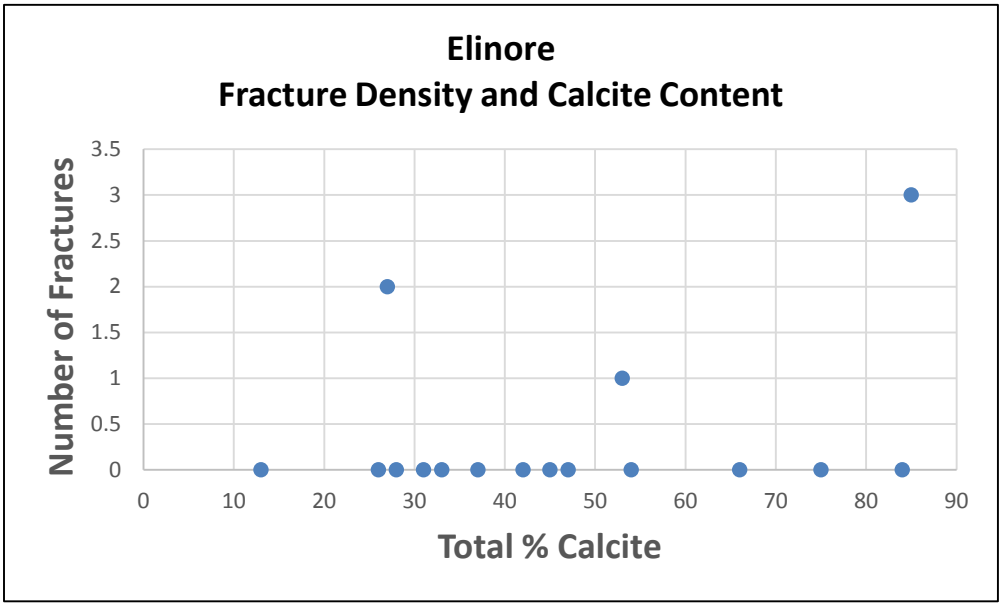
Elinore
Fracture Density and Calcite Content
Number of Fractures
3.5
3
2.5
2
1.5
1
0.5
0
0
10
20
30
40
50
60
70
80
90
Total % Calcite

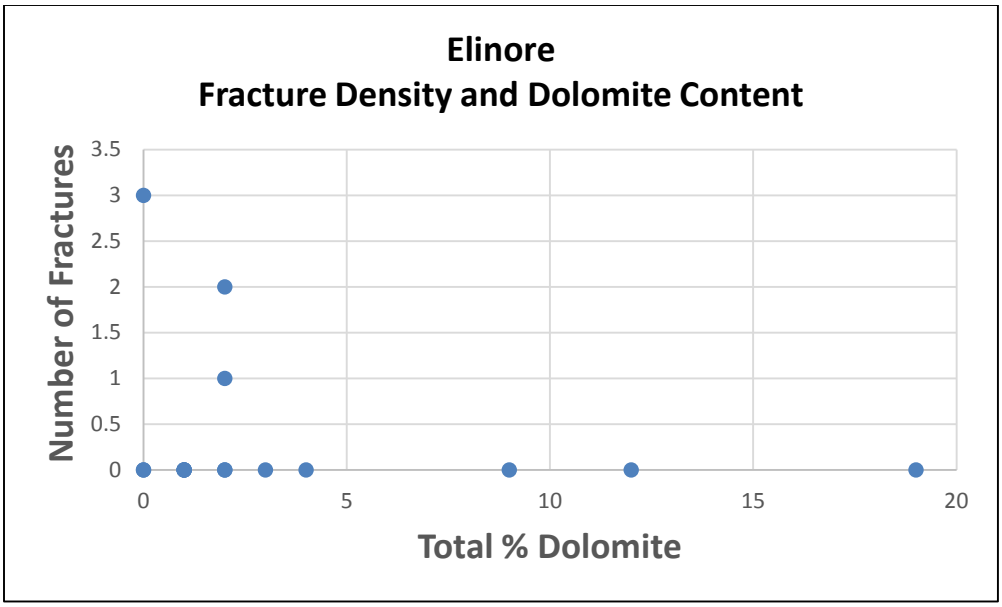
Elinore
Fracture Density and Dolomite Content
Number of Fractures
3.5
3
2.5
2
1.5
1
0.5
0
0
5
10
15
20
Total % Dolomite

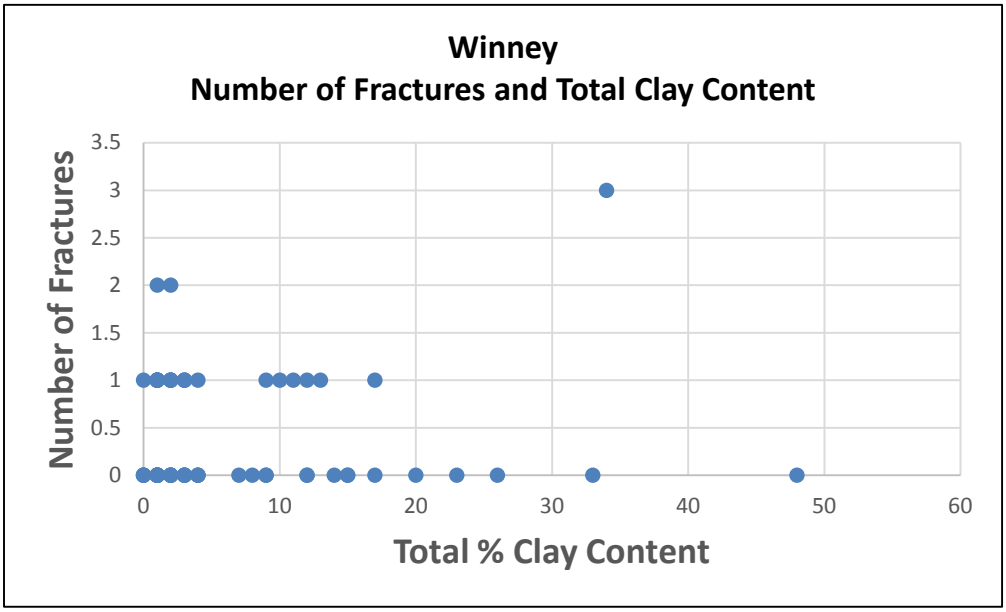
Winney
Number of Fractures and Total Clay Content
Number of Fractures
3.5
3
2.5
2
1.5
1
0.5
0
0
10
20
30
40
50
60
Total % Clay Content

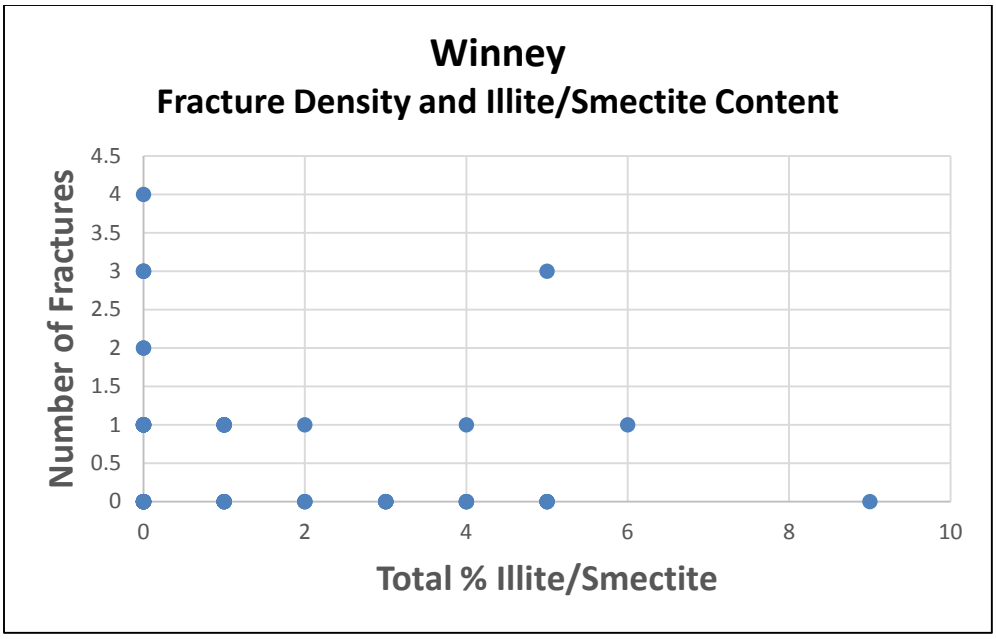
Winney
Fracture Density and Illite/Smectite Content
Number of Fractures
4.5
4
3.5
3
2.5
2
1.5
1
0.5
0
0
2
4
6
8
10
Total % Illite/Smectite

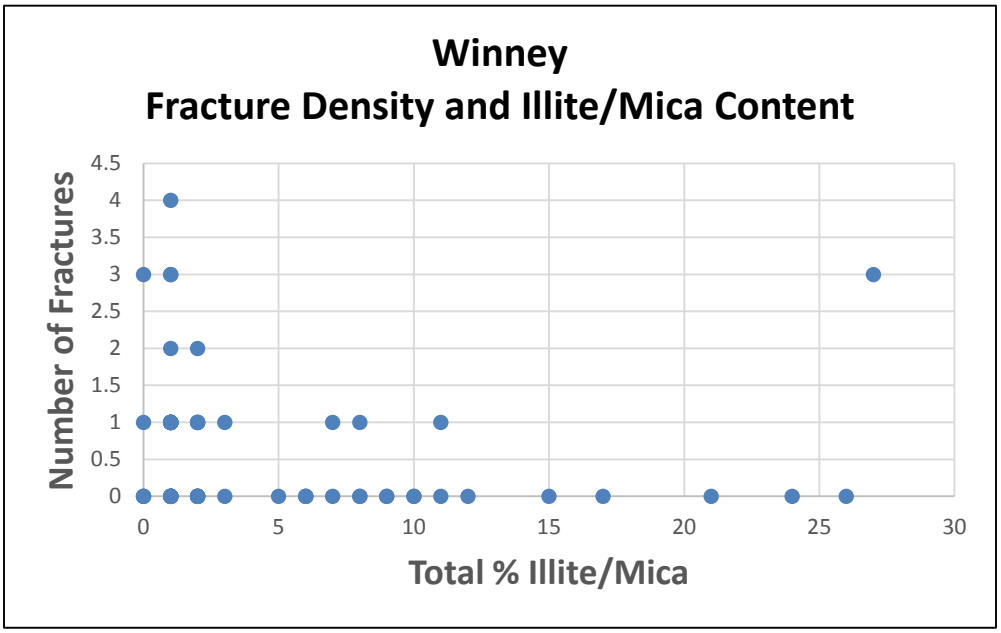
Winney
Fracture Density and Illite/Mica Content
Number of Fractures
4.5
4
3.5
3
2.5
2
1.5
1
0.5
0
0
5
10
15
20
25
30
Total % Illite/Mica

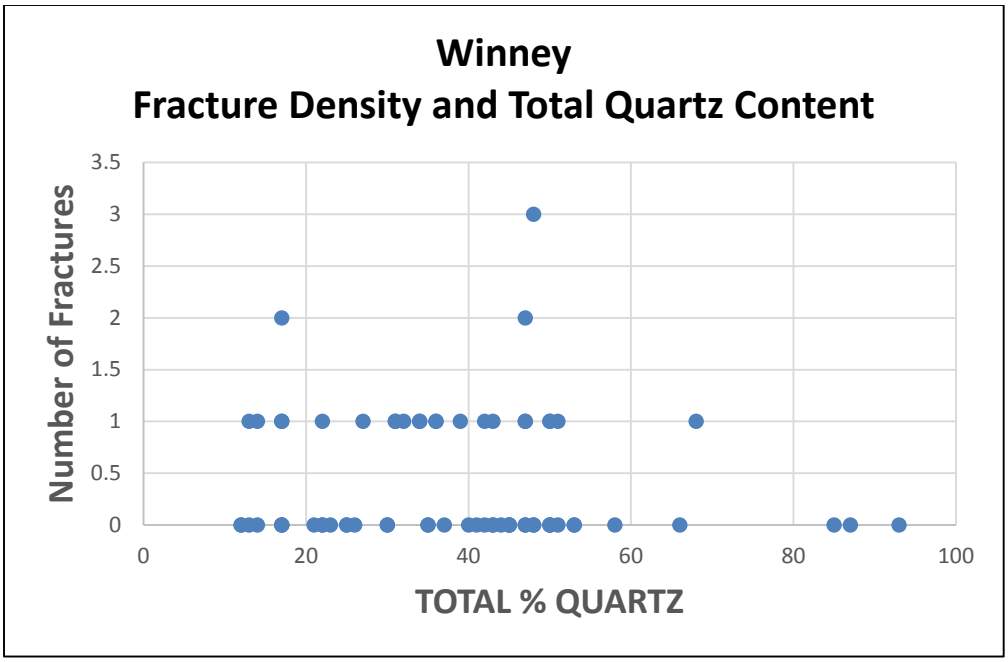
Winney
Fracture Density and Total Quartz Content
Number of Fractures
3.5
3
2.5
2
1.5
1
0.5
0
0
20
40
60
80
100
TOTAL % QUARTZ

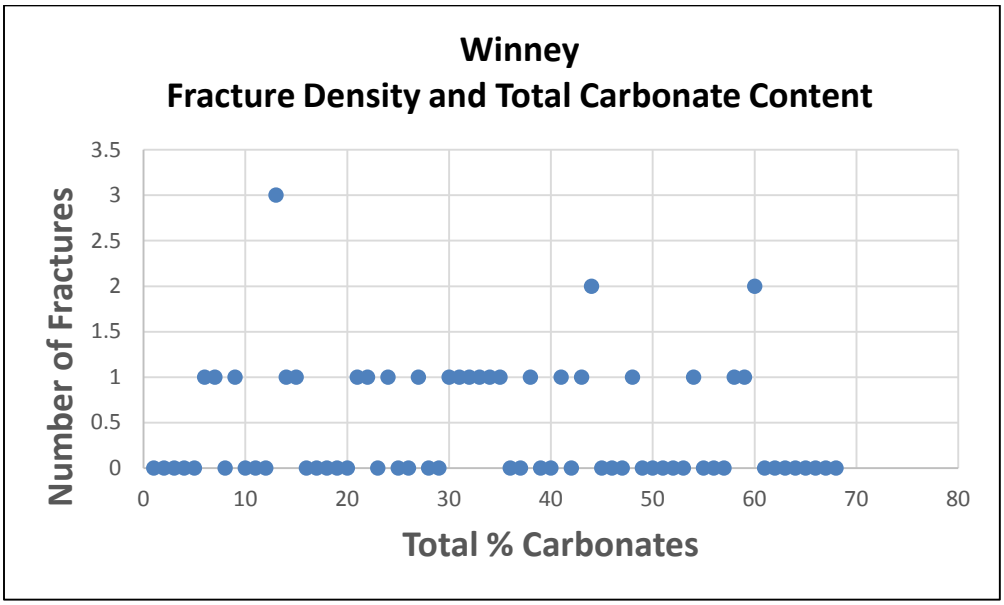
Winney
Fracture Density and Total Carbonate Content
Number of Fractures
3.5
3
2.5
2
1.5
1
0.5
0
0
10
20
30
40
50
60
70
80
Total % Carbonates

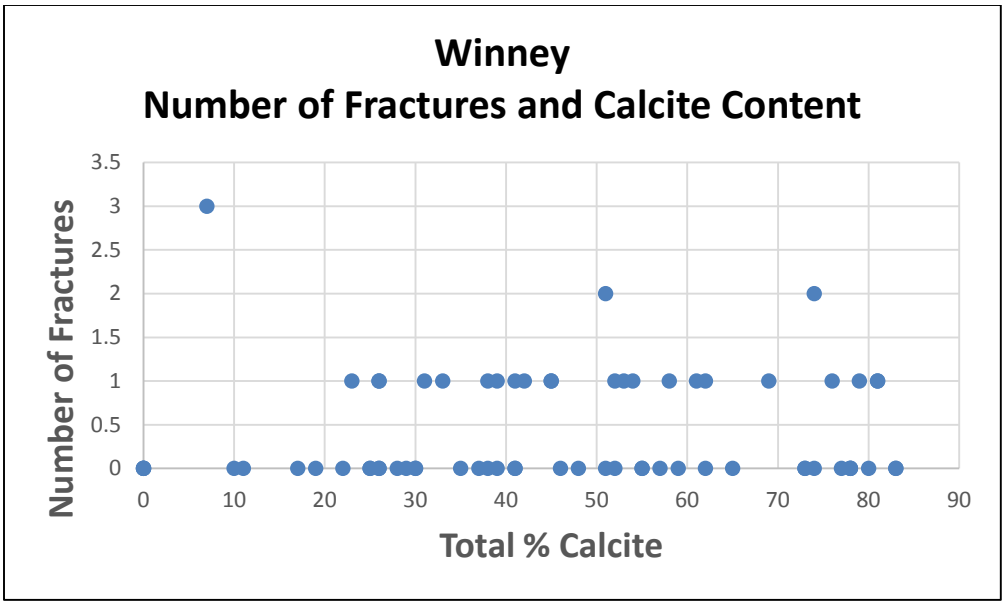
Winney
Number of Fractures and Calcite Content
Number of Fractures
3.5
3
2.5
2
1.5
1
0.5
0
0
10
20
30
40
50
60
70
80
90
Total % Calcite

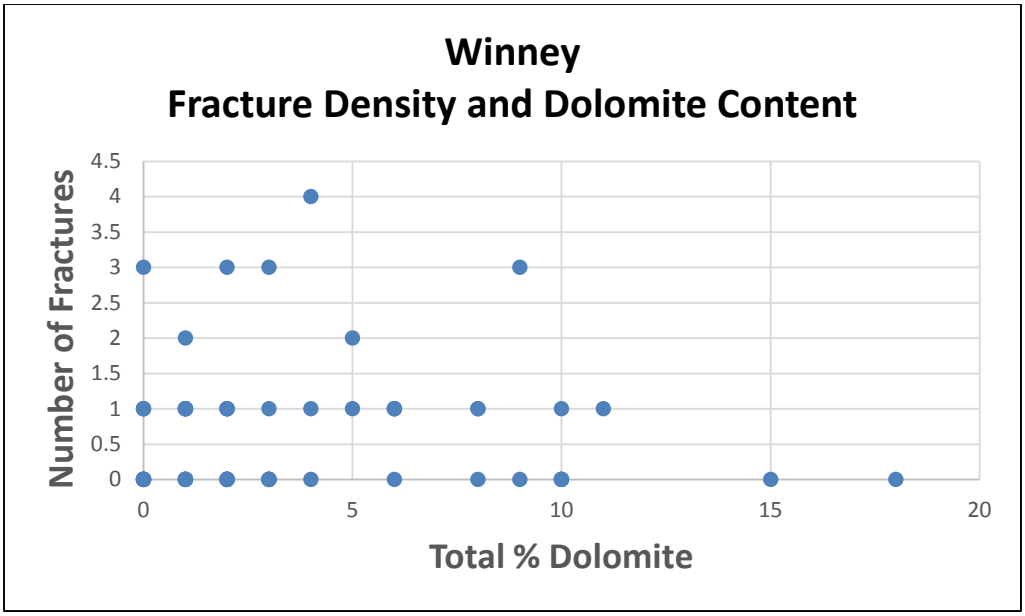
Winney
Fracture Density and Dolomite Content
Number of Fractures
4.5
4
3.5
3
2.5
2
1.5
1
0.5
0
0
5
10
15
20
Total % Dolomite

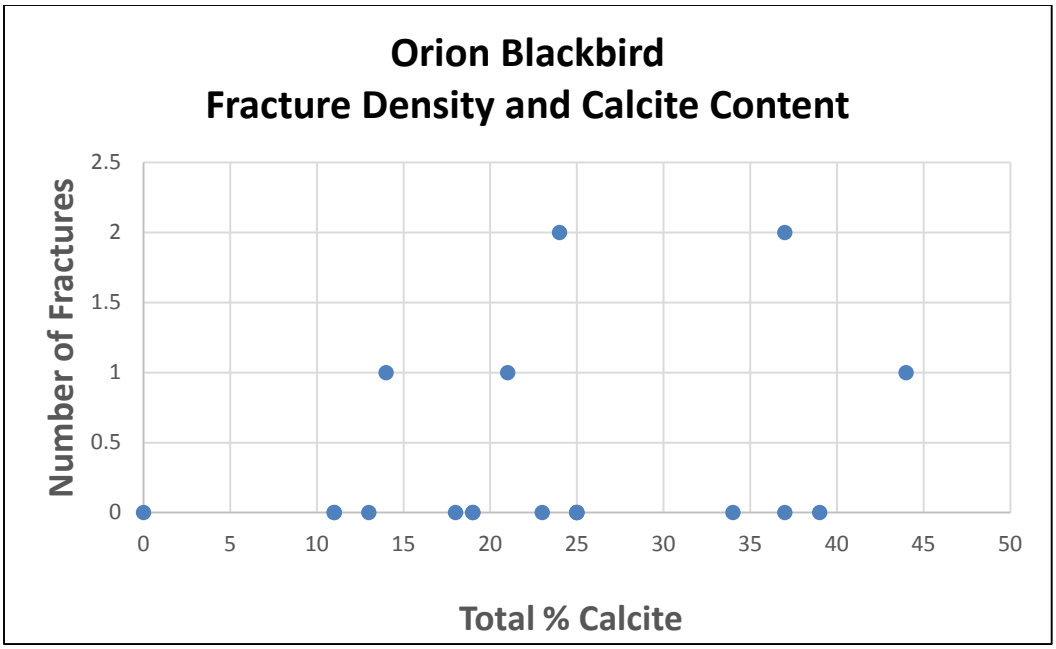
Orion Blackbird
Fracture Density and Calcite Content
Number of Fractures
2.5
2
1.5
1
0.5
0
0
5
10
15
20
25
30
35
40
45
50
Total % Calcite

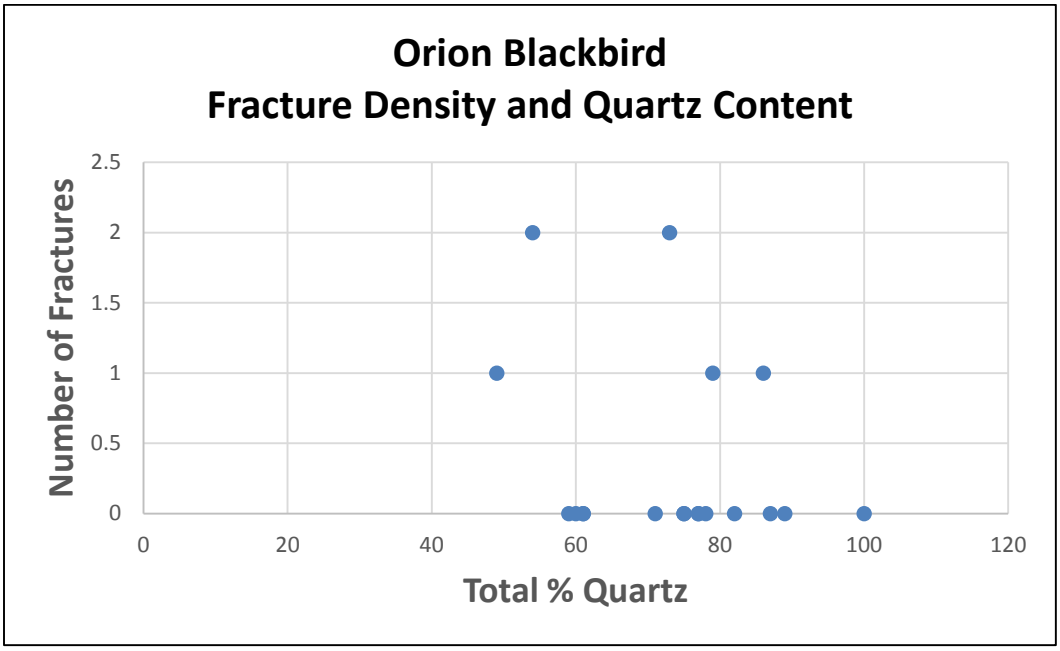
Orion Blackbird
Fracture Density and Quartz Content
Number of Fractures
2.5
2
1.5
1
0.5
0
0
20
40
60
80
100
120
Total % Quartz

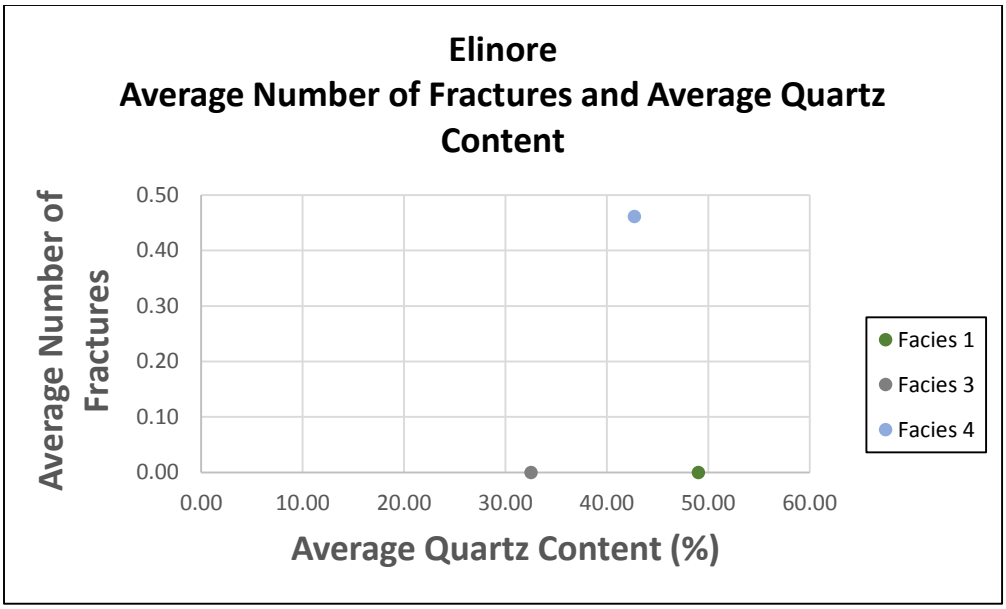
Elinore
Average Number of Fractures and Average Quartz Content
Average Number of Fractures
0.50
0.40
0.30
0.20
0.10
0.00
0.00
10.00
20.00
30.00
40.00
50.00
60.00
Average Quartz Content (%)
Facies 1
Facies 3
Facies 4

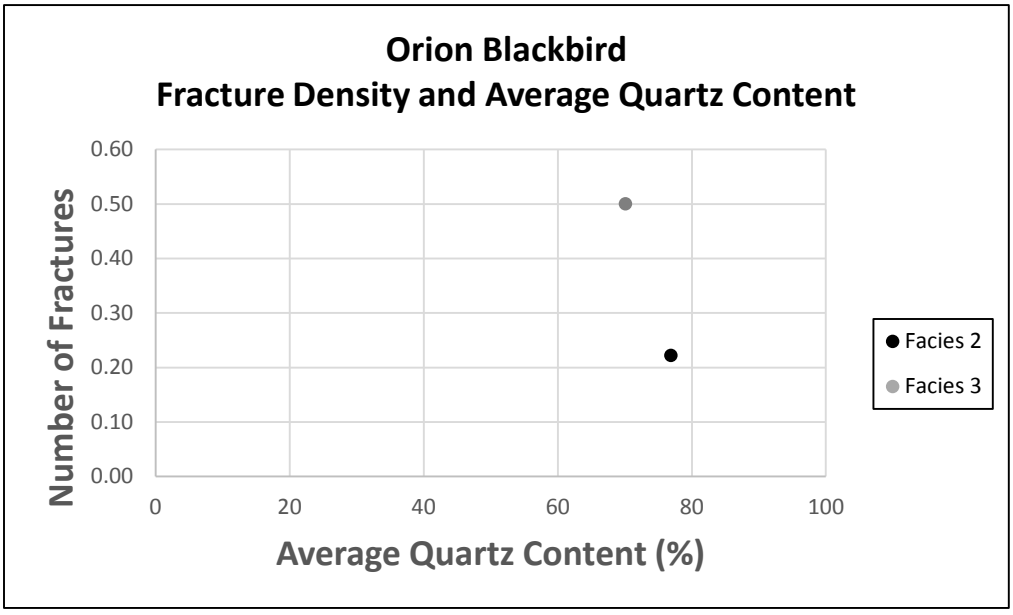
Orion Blackbird
Fracture Density and Average Quartz Content
Number of Fractures
0.60
0.50
0.40
0.30
0.20
0.10
0.00
0
20
40
60
80
100
Average Quartz Content (%)
Facies 2
Facies 3

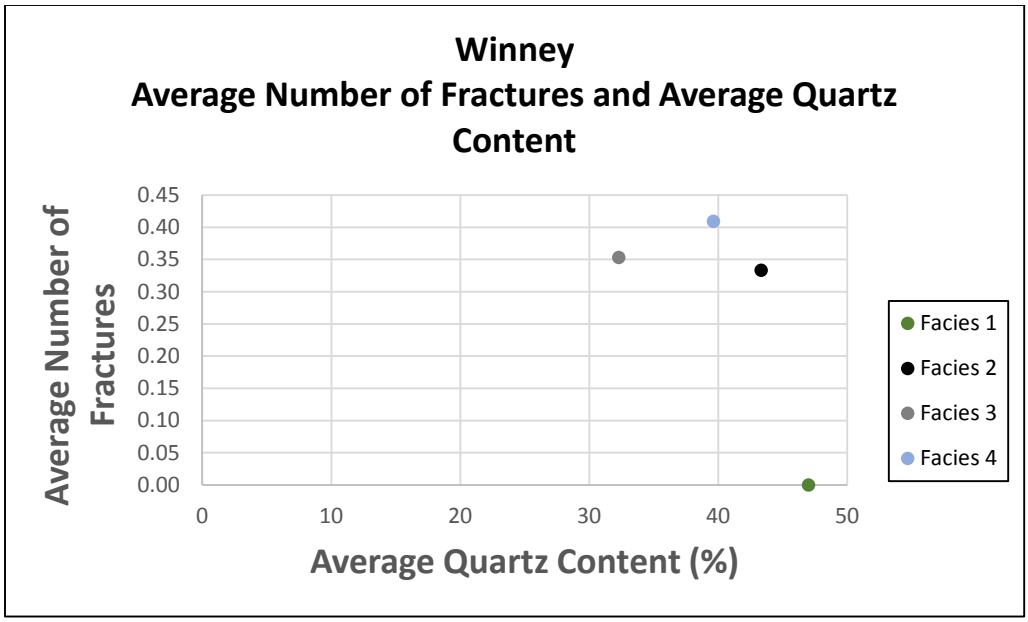

The following graphs depict correlation between the averaged fracture density and averaged XRD data from the Elinore and Orion Blackbird cores.

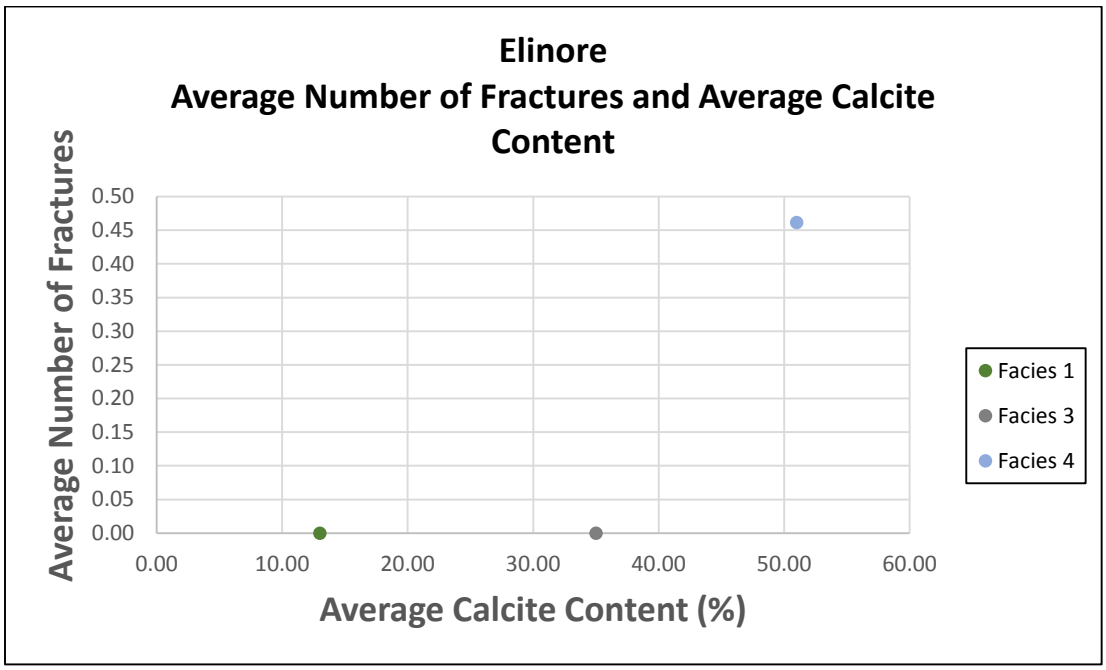

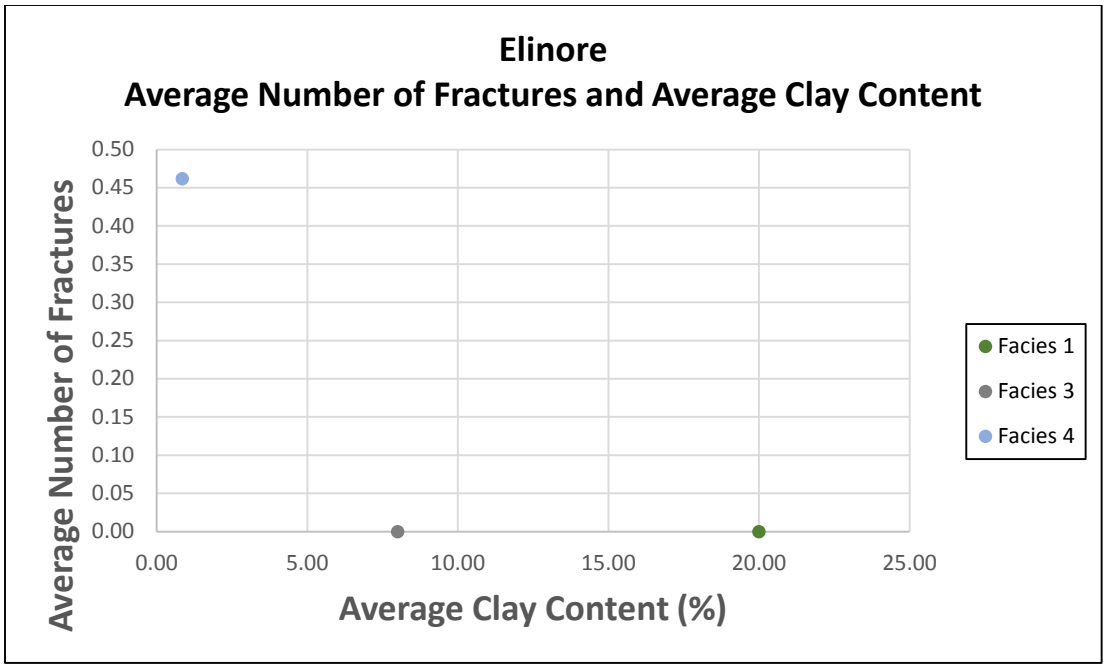
Elinore
Average Number of Fractures and Average Clay Content
Average Number of Fractures
0.50
0.45
0.40
0.35
0.30
0.25
0.20
0.15
0.10
0.05
0.00
0.00
5.00
10.00
15.00
20.00
25.00
Average Clay Content (%)
Facies 1
Facies 3
Facies 4

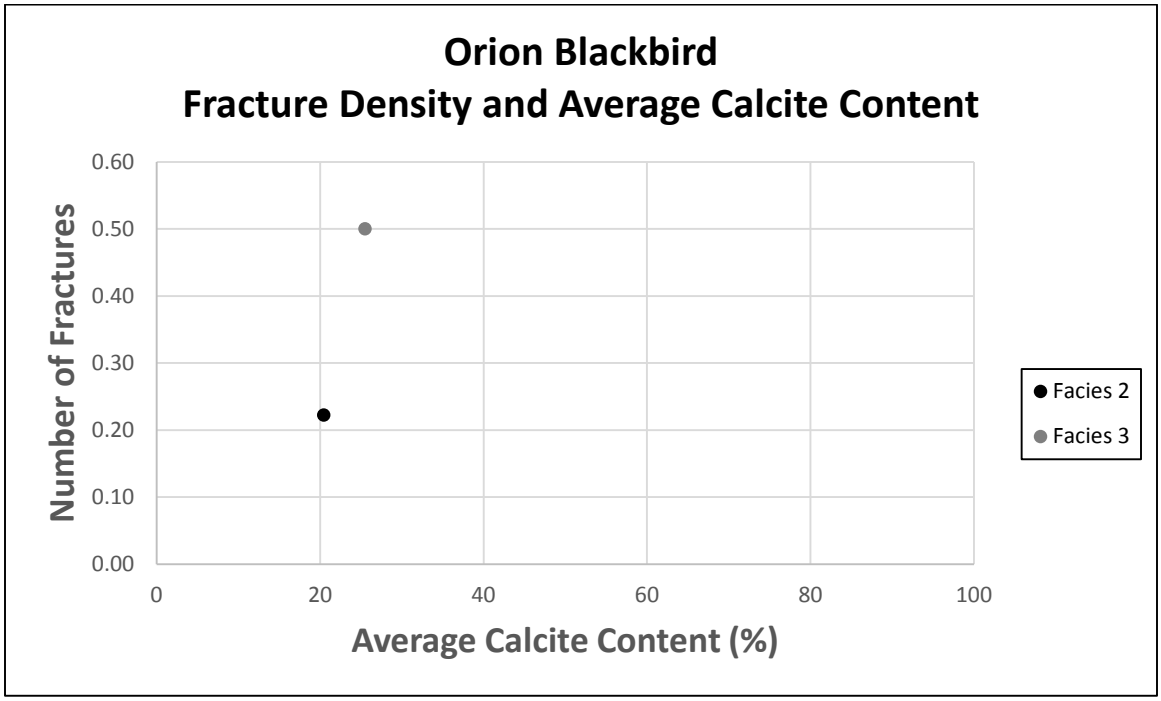
Orion Blackbird
Fracture Density and Average Calcite Content
Number of Fractures
0.60
0.50
0.40
0.30
0.20
0.10
0.00
0
20
40
60
80
100
Average Calcite Content (%)
Facies 2
Facies 3

APPENDIX C

CORE PHOTOGRAPHS OF FRACTURES

The following photographs represent examples of vertical extensional fracturing.

Core photo of vertical extensional fracturing (arrows) in the Elinore core in Facies 3 (bioturbated wackestone-packstone) at a depth of 4459.0'. The fracture height is approximately 335 millimeters and the aperture was not measured due to the fracture

being completely broken apart. The fracture is partially mineralized with calcite that is seen on the fracture walls at the arrow locations.

Core photo of vertical extensional fracturing (arrows) in the Elinore core in Facies 4 (crinoidal packstone-grainstone) at a depth of 4411.5'. The fracture height is approximately 291 millimeters and the aperture was not measured due to the fracture

being completely broken apart. The fracture walls are partially mineralized with calcite (not shown in photo).

Core photo of vertical extensional fracturing in the Winney core in Facies 4 (crinoidal packstone-grainstone) at a depth of 5228.0'. The extensional fracture is indicated by the white arrows. The fracture height is approximately 105 millimeters and the aperture was not measured due to the fracture being completely broken apart. The fracture is partially mineralized with calcite (seen on the fracture walls at the arrow locations).

The following photographs represent examples of ptygmatic fracturing.

Core photo of ptygmatic fracturing (arrows) in the Elinore core in Facies 3 (bioturbated wackestone-packstone) at a depth of 4458.4'. The fracture height is approximately 450 millimeters and the aperture ranges from 0.1-2 millimeters. The fracture is mineralized

with calcite and heavier distortion (folding) is present in the darker material towards the top of the photo.

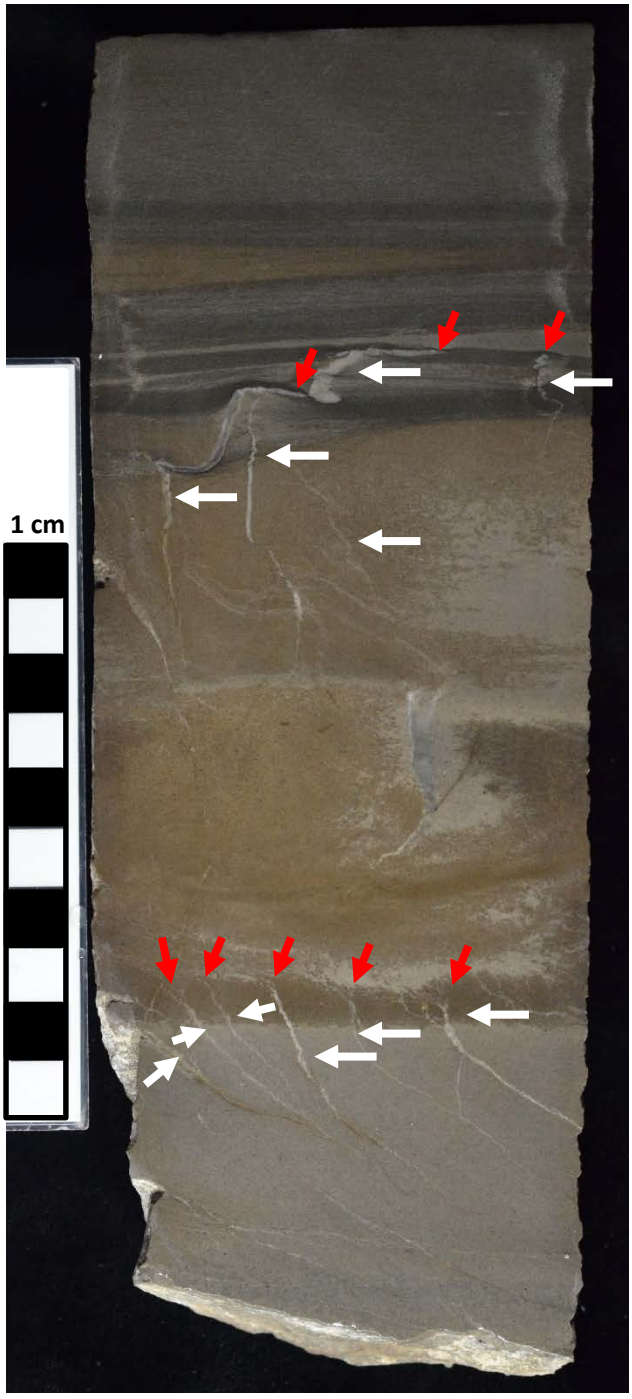

Core photo of ptygmatic fracturing in the Elinore core in Facies 4 (crinoidal packstone-grainstone) at a depth of 4395.3'. The ptygmatic fractures are indicated by the white arrows. The fracture heights range from 20-35 millimeters and the apertures range from 0.1-1.5 millimeters. The fractures are mineralized with calcite and the red arrows

indicate fracture terminations at specific layers. Heavier folding in these fractures is present in the dark gray material near the top of the photo.

Core photo of ptygmatic fracturing in the Winney core in Facies 3 (bioturbated wackestone-packstone) at a depth of 5261.5'. The ptygmatic fractures are indicated by the white arrows. The fracture heights range from 10-42 millimeters and the apertures range from 0.1-1 millimeters. The fractures are mineralized with calcite and are bounded by darker layers at both ends (indicated by red arrows).

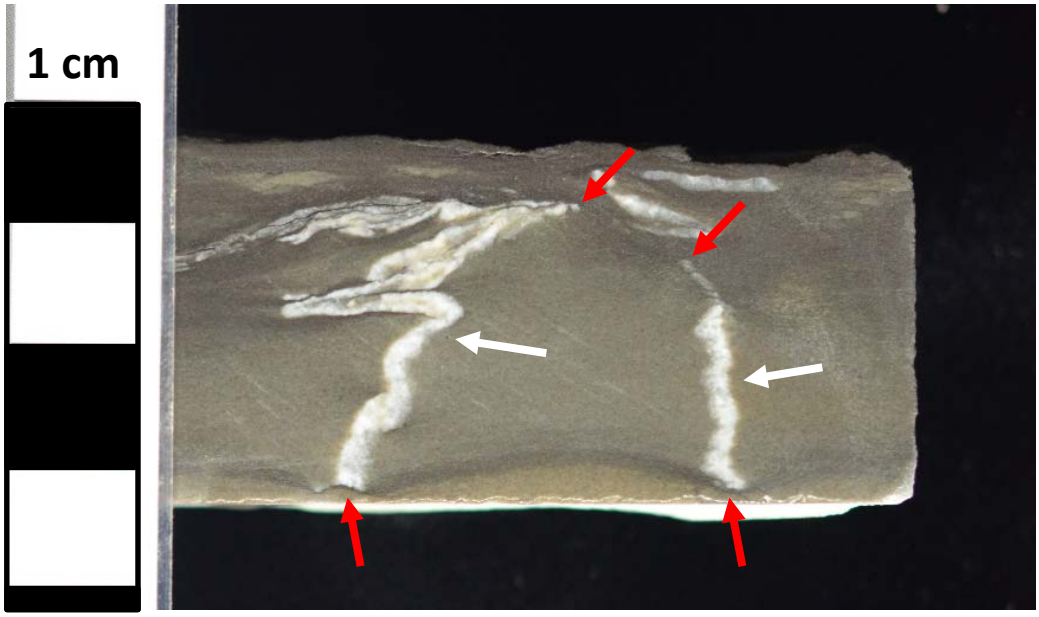

Core photo of ptygmatic fracturing (white arrows) in the Winney core in Facies 4 (crinoidal packstone-grainstone) at a depth of 5236.9'. The average fracture height is 24.5 millimeters and the apertures range from 0.5-2 millimeters. The fractures are mineralized with calcite and terminate at both ends (indicated by red arrows).

Core photo of ptygmatic fracturing (arrows) in the Orion Blackbird core in Facies 2 (burrowed mudstone-wackestone) at a depth of 3406.2'. The fracture height is approximately 189 millimeters and the aperture ranges from 0.5-4 millimeters. The fracture is mineralized with calcite and heavier folding occurs near the bottom of the photo.

The following photographs represent examples of mixed fracturing.

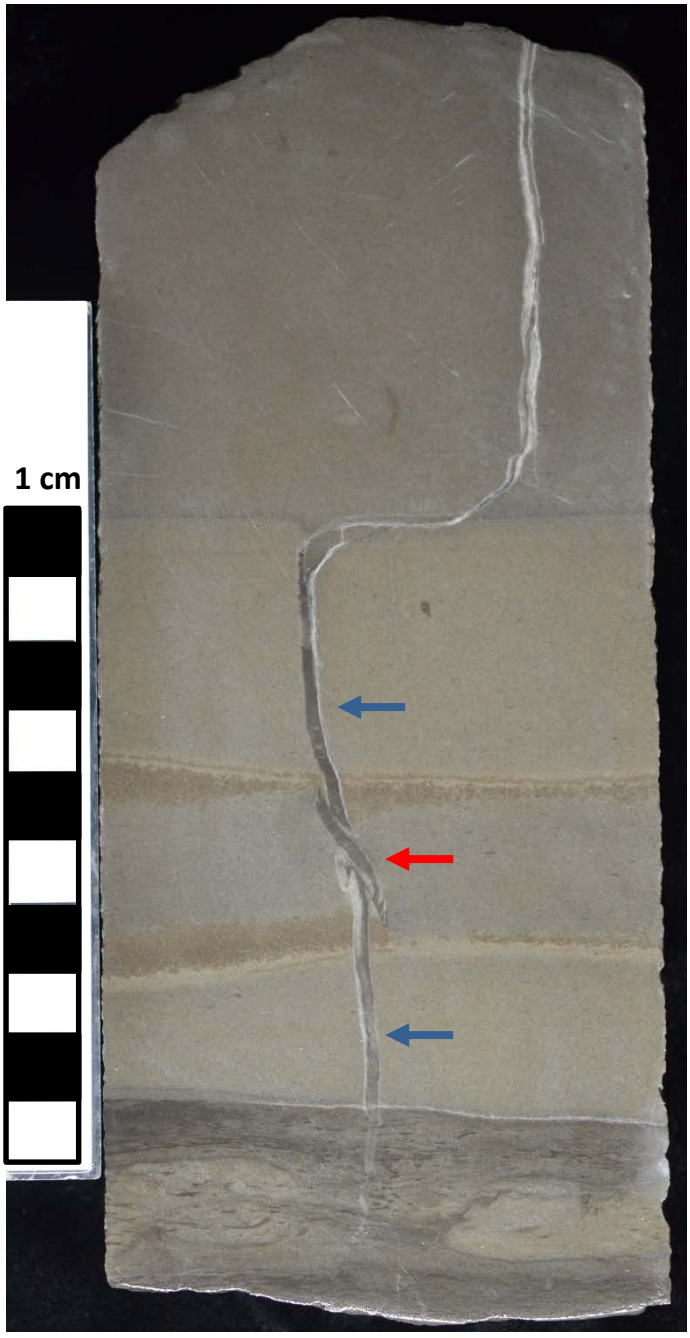

Core photo of a mixed fracture in the Elinore core in Facies 4 (crinoidal packstone-grainstone) at a depth of 4402.0'. The extensional portions of the fracture are indicated by the blue arrows and the ptygmatic portion is indicated by the red arrow. The fracture height is approximately 207 millimeters and the aperture ranges from 0.3-2.5

millimeters. The fracture may contain multiple zones of calcite cement (indicated by differing cement colors).

VITA

Taylor Thompson

Candidate for the Degree of

Master of Science

Thesis: FRACTURE CHARACTERIZATION AND PREDICTION IN THE "MISSISSIPPIAN LIMESTONE" IN NORTH-CENTRAL OKLAHOMA

Major Field: Geology

Biographical:

Education:

Completed the requirements for the Master of Science in Geology at Oklahoma State University, Stillwater, Oklahoma in May, 2016.

Completed the requirements for the Bachelor of Arts in Geology at University of Colorado, Boulder, CO/USA in 2013.

Experience:

Interned at Linn Energy in Oklahoma City, OK in 2014.

Professional Memberships:

American Association of Petroleum Geologists